Extending the Performance and Bandwidth of Electromechanical Devices

Adrian R. D. Stamp

Department of Mechanical Engineering

University College London

A thesis submitted in partial fulfilment of the requirements for the Degree of

DOCTOR OF PHILOSOPHY

I, Adrian Stamp confirm that the work presented in this thesis is my own. Where information has been derived from other sources, I confirm that this has been indicated in the thesis.

Abstract

Electromechanical devices are used in a wide range of dynamic applications, from hard disk drives to levitating trains; therefore any improvements in the dynamic performance of such devices would be of significant academic and commercial benefit.

This thesis presents theoretical and experimental analyses of shorted turns (conductive loops inductively coupled to a coil). The effect of shorted turn design parameters was investigated using electromagnetic actuator models, measuring force and electrical impedance, with the aims of increasing dynamic range and stability.

It was found that a shorted turn reduces the motor constant at high frequencies; it does however significantly improve the transient response of the total coil current. This would suggest that although a shorted turn is likely to reduce the peak force, with the correct shorted turn configuration an increase in acceleration may be apparent; this would be particularly beneficial for positioning actuators with fast response time, such as those found within hard disk drives. A shorted turn was also found to provide damping, attributed to eddy-currents, which reduced resonance in tests.

Utilising an inductively-coupled secondary coil it was possible to control the shorted turn effect, switching it on and off as desired. This could be applied in practice: the shorted turn could be passive in the acceleration phase and active in the deceleration phase, potentially leading to improvements in the dynamic performance.

Table of Contents

Nomenclature

μ_0	Permeability of free space ($4\pi\times10^{-7}$ NA^{-2})
$\ddot{\theta}$	Angular acceleration (rad s^{-2})
σ_F	Stress on flexures (Pa)
Ω	Cut-Off frequency (rad/s)
A_{AG}	Cross-sectional area of air gap (m^2)
$A_{COATING}$	Exposed area of coating (m^2)
A_S	Cross-sectional area of stator (m^2)
A_{WIRE}	Cross-sectional area of coil wire (m^2)
$B_{AC(MAX)}$	Maximum AC flux density (T)
$B_{DC(MAX)}$	Maximum DC flux density (T)
B_{MAX}	Total maximum flux density (T)
B_P	Peak magnetic flux density (T)
c_{EDDY}	Eddy current damping constant
δ_{MAX}	Maximum deflection (m)
ε_f	Strain on flexures
E_F	Young's Modulus of flexures (GPa)
ε_i	Induced EMF (V)
E_{SHAFT}	Young's modulus of shaft (220GPa)
F_{COG}	Cogging force (N)
F_F	Full scale load cell force (100N)
F_M	Measured force (N)
F_{MAG}	Magnetic force (N)
F_N	Normal force (N)
F_{PM}	Force from permanent magnet (N)
F_{TANA}	Tangential force configuration A (N)
F_{TOTAL}	Total force (N)
f_{p1}	Frequency of pole 1 (Hz)
f_{p2}	Frequency of pole 2 (Hz)
fz	Frequency of zero (Hz)
g	Gravitational field strength - 9.81ms^{-2}

G	Load cell sensitivity
H	Strain gauge amplifier gain
$ɦ$	Heat transfer coefficient (W/m^2)
h_S	Height of stator (m)
I_A	Second moment of area (m^4)
I_{ST}	Shorted turn current (A)
I_M	Magnetising current (A)
I_T	Total current (A)
J	Moment of inertia
κ	Thermal conductivity (W/m)
K_{EDDY}	Constant relating eddy current damping and conductor geometry
K_{EVAL}	Constant relating eddy current damping constant and thickness
k_{FXLC}	Stiffness of flexures in the horizontal direction and load cell (N/m)
k_{FY}	Stiffness of flexures in the vertical direction (N/m)
k_G	Stiffness of flexures due to gravitational restoring force (N/m)
K_M	Motor constant between the total current and force (N/A)
K_{MM}	Motor constant between the magnetising current and force (N/A)
L_1	Coil inductance (mH)
L_{12}	Mutual inductance (mH)
L_2	Shorted turn leakage inductance as viewed from the coil (mH)
l_{COILA}	Length of coil in configuration A (m)
l_F	Length of flexures (m)
l_{MF}	Distance between mover and flexure (m)
l_S	Distance between flexures (m)
L_{ST}	Shorted turn leakage inductance (mH)
MMF	Magnetiomotive force (N·A·turns)
M_{MS}	Mass of mover and shaft (kg)
N_1	Number of turns in primary coil (turns)
N_{ST}	Number of turns in shorted turn (turns)
P	Power (W)
ρ	Resistivity
R_1	Coil resistance (Ω)

R_2	Shorted turn resistance as viewed from the coil (Ω)
$R_{COATING}$	Thermal resistance of wire coating (ºC/W)
$R_{CONVECTION}$	Resistance of air through convection (ºC/W)
R_{SENSE}	Current Sensing Resistor (Ω)
R_{ST}	Shorted turn resistance (Ω)
R_{TOTAL}	Total resistance (Ω)
T_1	Coil temperature (ºC)
T_2	Temperature at wire coating (ºC)
t_F	Thickness of flexures (m)
T_{ROOM}	Room temperature - 21^{o}C
V_1	Voltage across coil (V)
V_2	Voltage across coil and current sensing resistor (V)
V_E	Excitation voltage (V)
V_F	Force voltage reading (V)
V_{in}	Input voltage (V)
V_M	Measured voltage (V)
V_{out}	Output voltage (V)
W	Stored energy (J)
W'	Stored energy in the volume of air gap (J/M^3)
w_F	Width of flexures (m)
ω_n	Natural frequency (Hz)
x	Horizontal displacement (m)
$\dot{x}$	Velocity (m/s)
Y_M	Magnetising current admittance (Ω^{-1})
Y_{COIL}	Primary coil admittance (Ω^{-1})
y	Air gap height (m)
Z_1	Coil impedance (Ω)
Z_2	Shorted turn impedance as viewed from the coil (Ω)
Z_{COIL}	Coil impedance (Ω)

List of Figures

List of Tables

1. Introduction

Electromechanical devices are extensively used from small scale systems such as hard disk drives and loudspeakers to much larger applications such as transportation (hybrid cars and high speed levitating trains) (Slemon, Turton, & Burke, 1974). Therefore due to the wide ranging usage, any improvements in electromechanical performance would be of significant academic and commercial benefit. The major parameters of interest when using electromechanical devices are the factors affecting the dynamic performance and dynamic range (bandwidth), e.g. positioning accuracy, force, controller responsiveness and system stability. Research has shown (Hirano, Naruse, & Tsuchiyama, 1989) that a possible aid in improving the overall performance of electromechanical devices is a shorted turn.

A "shorted turn" may be any complete electrical circuit in a coil's magnetic field. When a sinusoidal current is passed through the coil of an electromechanical device a magnetic field of changing flux is produced; which in-turn induces a current into the shorted turn producing its own magnetic field. According to Lenz's law, the direction of this magnetic field will be such that, any current induced back into the coil would serve to increase the coil current or reduce the impedance. The interactions between a shorted turn and a coil are analogous to the secondary and primary coils of a transformer, for this reason a transformer based model was the basis of the analysis throughout this thesis.

Analysing equation 1.1 it is apparent that the most significant reductions in coil impedance would be at high frequencies, this is as at high frequencies the rate of change of flux $\left(\frac{d\phi}{dt}\right)$ would be high and therefore the emf induced in the shorted turn (ε_i) would be large. However at higher frequencies, above the coil's breakpoint frequency, the primary coil current (I) will drop due to an increased coil impedance, also reducing the emf induced into the shorted turn (ε_i).

$$\varepsilon_i = I\frac{d\phi}{dt} \tag{1.1}$$

Figure 1-1a shows a coil without a shorted turn while Figure 1-1b shows the same coil with an aluminium cylinder around it. In this scenario, the coil produces the magnetic field while the aluminium cylinder is the electrical circuit within this field (shorted turn). Since the shorted turn may come in the form of any conductive material in a complete circuit; it is typical for shorted turn effects to be present in many devices by accident of design (aluminium cases, bobbins).

a) **b)**

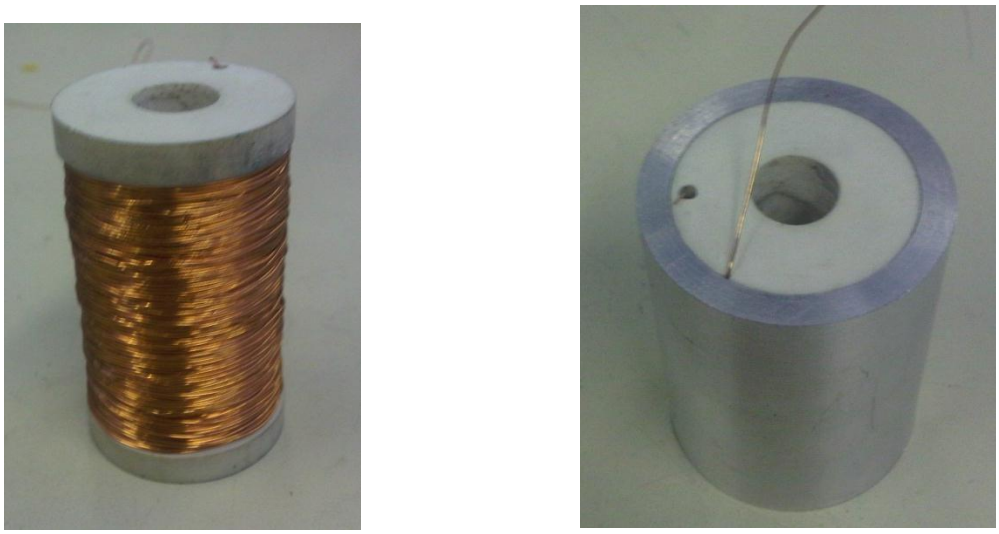

Figure 1-1. a) A coil without a shorted turn. b) A coil with a shorted turn.

Although shorted turns are commonly employed to exploit the reduction of apparent inductance within hard disk drives, a comprehensive study of the shorted turn is yet to be published. This thesis aims to provide a framework for the design of shorted-turns within electromechanical systems to optimise the electrical and dynamic characteristics of such devices.

Although there is a large amount of diversity within electromechanical devices, a system model containing the elements of a typical electromechanical system with a controller (figure 1-2) was the basis of improving the dynamic performance and range throughout the thesis. ADC represents the analogue to digital conversion, μ_CP

represents the processing of the controller and DAC represents the digital to analogue conversion which all together represents the controller; AMP denotes the amplifier, with $\mu_A P$ denoting the amplifier processing. Z is the coil impedance, K_M is the motor constant and 'Dynamics' is the system dynamics.

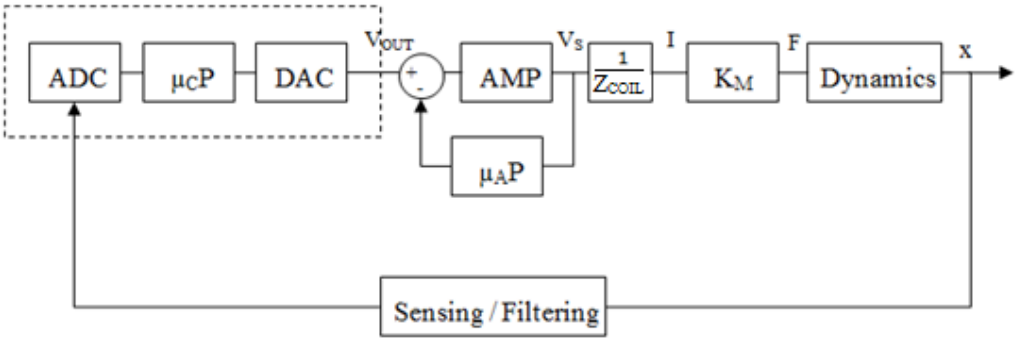

Figure 1-1. A system model of a typical electromechanical device.

The processing required by the controller and amplifier, the ADC and DAC will all cause a time delay affecting system stability. All the other components will cause system lags often affecting both the system stability and dynamic range within a closed loop system. The effect of lags and delays within the components of the system model (described in figure 1-2) may be described in the frequency domain using stability margins (gain and phase margins). Any additional gain at the frequency where the phase is -180 degrees or additional phase lag where the gain is at 0dB will push the system away from positive gain and phase margins (fig. 1-3a) and closer to negative phase and/or gain margins; instability (fig. 1-3b). Larger stability margins allows larger controller gains to be applied to the system before it becomes unstable, producing a more responsive system - an improved dynamic performance (Collinson, 2011).

a)

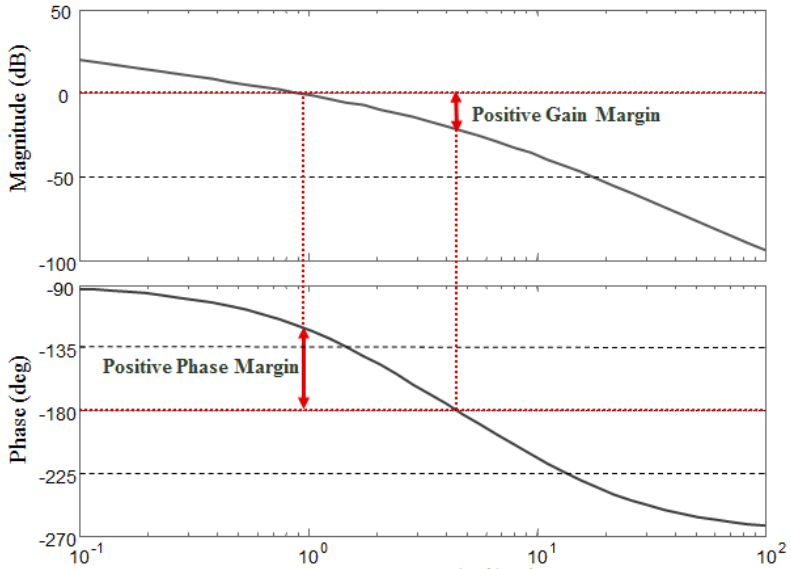

b)

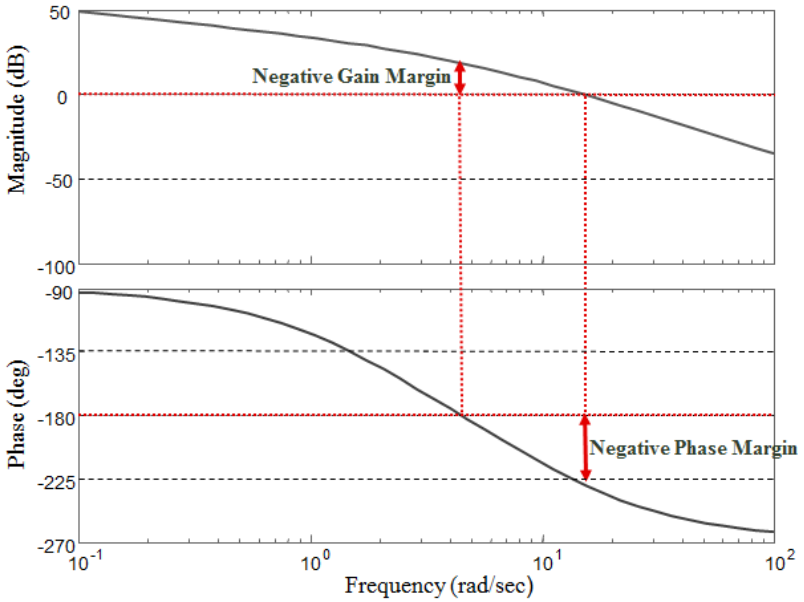

Figure 1-2. Stability margins of a) a stable system and b) and unstable system.

The primary coil impedance 'Z_{COIL}' within the system model is inherently frequency-dependent; above the coil's breakpoint frequency this impedance increases in proportion to frequency. This effect often limits the high-frequency performance of devices; producing a greater phase lag between the voltage input and produced current (Miller & Miller, 2007), reducing stability margins and the system bandwidth (throughout this thesis 'bandwidth' is defined as the range of frequencies that is within 3dB of the closed loop gain value). The high frequency increase in coil impedance will also cause a reduction in primary coil current, slowing the current transient response and reducing the force production. A shorted turn may produce useful performance improvements for many electromechanical devices by reducing the apparent primary coil inductance and in turn reducing the coil impedance.

$$Z_{COIL} = R_1 + j\omega L_1 \tag{1.2}$$

This has the effect of reducing the primary coil phase lag and producing a faster current response which may translate to increased force and therefore faster device acceleration, dependent on the method of coil excitation.

The main parameters of a shorted turn are resistance and inductance; however these properties are dependent on the shorted turn's geometric properties, for example with the shorted turn shown in figure 1-1b reducing the wall thickness of the aluminium cylinder would increase the shorted turn resistance and therefore impedance. To ascertain the significance of these main parameters (resistance and inductance) a range of experiments were designed to by varying the shorted turn's geometrical properties; which although would not give complete isolation of the shorted turn resistance and inductance would show how the shorted turn could be used in real-world situations..

Chapter 2 of this thesis evaluates related work in the form of a literature review, this identified methods that had been previously employed to improve the dynamic performance and range of electromechanical devices, and particularly research relating to the feasibility of utilising shorted turns in devices for the purposes of improving the dynamic range and performance. This review of related work was used to identify gaps in the research and a set of experiments based upon these gaps were designed in chapter 3, the results of these experiments were analysed in chapter 4 with the conclusions given in the fifth chapter and recommendations for future work given in the sixth chapter.

This thesis provides a detailed analysis of the effect of shorted turns on electromechanical devices and the feasibility of using them to improve the dynamic range (device bandwidth) and performance. This thesis also builds on previously published work (Stamp & Hanson, 2011) on the influence of the shorted turn parameters (resistance and inductance) on the dynamic range and performance and whether or not these parameters may be used to control and negate any negative effects that a shorted turn may produce; as research by Hirano suggests that a shorted turn may reduce the device motor constant (Hirano, Naruse, & Tsuchiyama, 1989).

2. Literature Review

The implementation of electromechanical devices has become more widespread in recent years due to the lower cost and increased strength of permanent magnets and improvements in power electronics and microprocessors; this has made the use of such systems over alternatives such as hydraulic, pneumatic and even internal combustion systems more economically viable (Thornton, 2005). Electromechanical systems have a range of advantages over the described alternative systems such as being more versatile and requiring less maintenance than hydraulic systems (Majumdar, 2000); therefore studies to improve the dynamic range and performance may further increase the scope and diversity of application for electromechanical devices.

Numerous studies have been conducted with an aim of increasing the bandwidth and force production of electromechanical devices with novel designs and techniques (Fujimoto, Kominami, & Hamada, 2009), (Zhu & Cho, 2010) & (Clower, 1994); one such example of this is Hajan et al.'s work on increasing the bandwidth of specific tasks by analysing how humans complete high bandwidth tasks (Hajian, Sanchez, & Howe, 1997). Humans have a relatively slow responding neuromuscular system with reaction times to tactile or visual cues well over 100ms; however humans can perform tasks well in excess of human motor control bandwidths such as a skilled drummer performing a drum roll at over 30Hz. The drummer achieves this by modifying the effective stiffness of the drumstick to allow the drumstick to bounce and play a beat two or more times per stroke. The research showed that the same principle may be applied to automated high bandwidth tasks by making a "drumming machine" with artificial muscles capable of impedance modulation to achieve performance comparable to a skilled human. This research produces a viable method for extending the bandwidth of a system beyond its traditional control limits, the work however is not a generically applicable method of extending the dynamic range of electromechanical devices as it is very application specific and requires novel methods to be designed for every application.

For the purposes of this literature review, research relating to the enhancement of electromechanical devices has been split into two categories,

i) Works where the significant benefit is the improvement of the dynamic performance such as targeting improvements in the current response of the coil windings;

ii) Research where the significant benefit is an increase in the dynamic range by methods such as reducing lags, delays and disturbances.

It should be noted that many solutions have benefits to both the dynamic range and performance.

2.1. IMPROVING DYNAMIC PERFORMANCE

Improving "dynamic performance" as referred to throughout this thesis means improving the performance of any of the aspects that cause motion in an electromechanical device; for the purpose of this thesis this encapsulates only the production of larger forces for faster acceleration and improved responsiveness e.g. a faster current response. In order to increase the force produced by an electromechanical device, an increase in the magnetic flux density and/or a larger current is required. An increase in coil current is often achieved by simply applying larger voltages to the system, although this does not improve the current response, only the maximum current. The issue with applying larger voltages to the system is that this is often impractical, for example speaker coils are often very lightweight and therefore cannot handle large coil currents for a sustained period; also a for stators with a core there is the additional problem of saturation whereby no increase in flux density is produced for the additional current.

Several studies have investigated small electromagnetic coils for the specific application of hard disk drives, within these devices, the read/write head is moved across the platter (the circular disk where the actual disk data is stored (Ec-Council, 2009)) by a voice coil motor; the dynamic performance of such actuators has a

significant impact on hard disk drive performance, as the faster the read/write head acceleration and deceleration, the faster the seek times. Voice coil motors are employed within hard disk drives as they offer fast acceleration and positioning accuracy of inertial loads, in this situation bang-bang control, whereby the maximum voltage is applied to the voice coil motor in order to accelerate the read/write head to its desired position and then the maximum voltage is applied in an opposing manner to decelerate it again (Jagacinski & Flach, 2003). This is often the preferable control method as it allows for rapid acceleration and deceleration (Ananthanarayanan, 1982). Figure 2-1, an idealised illustration of the effect of bang-bang control on actuator displacement, shows how linear acceleration may be achieved by using this method of control. In reality the current does not reach its maximum at the same point as the voltage, therefore the shorted turn may improve system response by reducing this discrepancy.

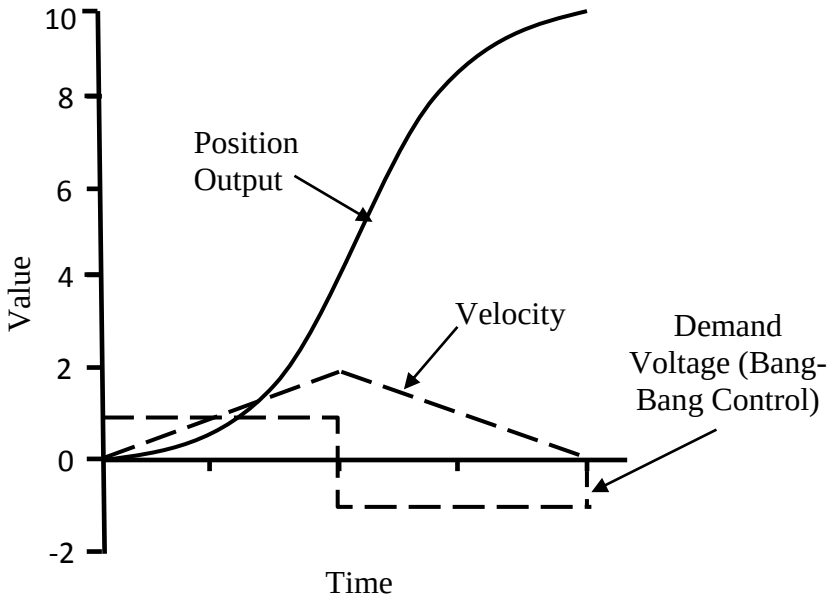

Figure 2-1. The kinematic response of a second order system to Bang-Bang control (the scaling is arbitrary) *(Reproduction from R. J. Jagacinski, J. Flach, 2003 – Psychology Press).*

2.1.1. SHORTED TURN

To aid the coil current in changing state rapidly, shorted turns are often implemented within hard disk drives; a shorted turn is a secondary conductive loop that is inductively coupled with the primary coil. The effect of this inductive couple is an apparent modification of the high frequency impedance of the primary coil. Shorted turn effects are present in many devices by accident of design (aluminium cases, bobbins) (Moser, 1996).

J. A. Wagner's paper 'The Shorted Turn in the Linear Actuator of a High Performance Disk Drive' was amongst the earliest published work to analyse a shorted turn within disk drives. The basis of the analysis was a transformer circuit model (fig. 2-2) in which Wagner derived relationships between the current response and the actuator electrical and geometrical parameters (Wagner, 1982). Although the model correlates well with the results of experimental testing over the initial and latter stages of the current response, the research gives a very limited indication of how this current response actually affects the actuator performance; the research within this thesis aims to build on Wagner's work, using the transformer model to investigate how a shorted turn may impact the dynamic performance of an electromechanical device.

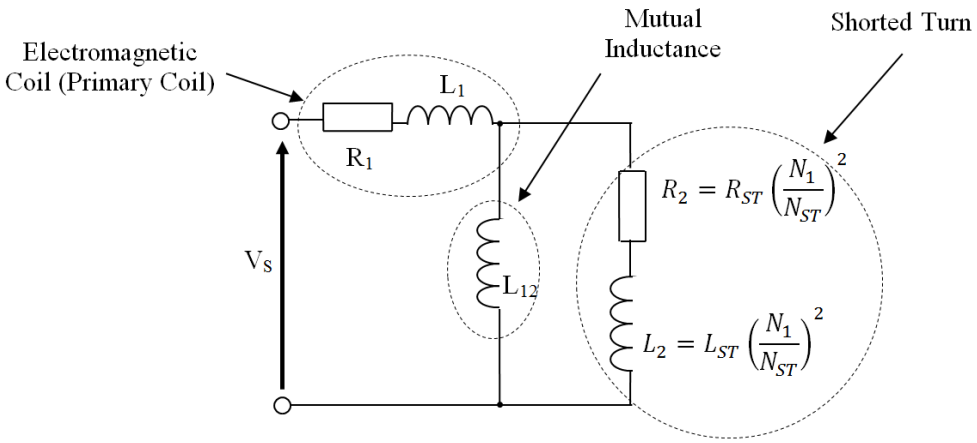

Figure 2-2. Circuit diagram of J.A Wagner's transformer circuit model.

Hirano et al. (Hirano, Naruse, & Tsuchiyama, 1989) modelled the dynamic characteristics of a voice coil motor with a shorted turn within a disk drive using finite element analysis. Modelling a voice coil motor requires the modelling of

parameters that may not be represented by simple analysis. This paper aimed to produce a design tool that was capable of simulating the motion of an actuator carriage for the optimisation of voice coil motor and shorted turn dimensions for minimal seek time. Although the design tool was not intended solely for shorted turn optimisation, within the paper the authors used the tool to optimise the shorted turn thickness (e.g. the wall thickness for a single turn shorted turn) for maximal dynamic performance. It was found that the maximum current (I_{MAX}) increased with the shorted thickness whilst the time and motor constants (τ and K respectively) of the system were both reduced (Hirano, Naruse, & Tsuchiyama, 1989). Figure 2-3 shows that the velocity reached by the carriage after 2ms of acceleration (U_{2ms}) was initially increased with shorted turn thickness, as the improved current response produces a greater force in a shorter time. With larger thicknesses of shorted turn the motor constant was so significantly degraded that the overall force produced from a coil with thicker shorted turns was lower than that of the thinner shorted turns, which have a slower rise time and lower maximum current; this produces a lower carriage velocity after 2ms of acceleration.

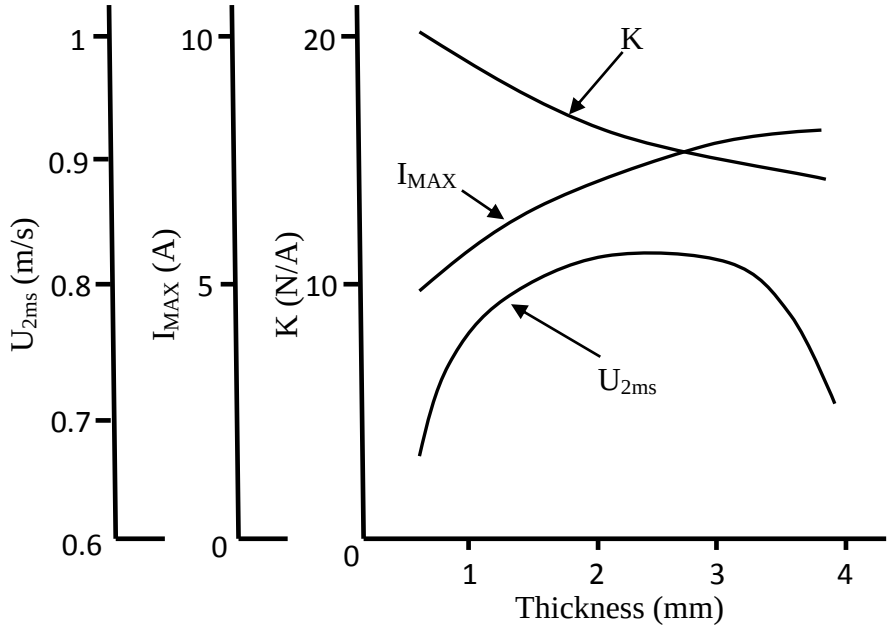

Figure 2-3. Simulation results summarising the effects of shorted turn thickness on the carriage speed after 2ms (U_{2ms}), maximum current (I_{MAX}) and the motor constant (K) *(Reproduction from Hirano et al., 1989 – IEEE).*

This paper established a link between the resistance of a shorted turn and the dynamic performance of a voice coil motor, with very detailed analysis on the effects of shorted turns of various thicknesses on actuator performance; however although experimental methods were utilised throughout the paper, none of these methods were implemented for shorted turn analysis. The work produced within this thesis aims to provide experimental validation of this reduction in motor constant with shorted turn thickness. The only shorted turn parameter investigated by Hirano et al. was the thickness, effectively investigating a change in shorted turn resistance, neglecting parameters such as shorted turn inductance and mutual inductance (closeness of coupling). This thesis aims to provide a more comprehensive study on the effects of varying shorted turn parameters on coil behaviour. This work includes analysis of the shorted turn thickness for verification purposes; however, it also investigates other methods of varying the shorted turn resistance and inductance. Inductive methods are also investigated with a "shorted coil" being utilised to investigate the effect of a change in shorted turn inductance by varying the number of turns in the coil; and methods of varying the mutual inductance by varying the flux leakage through methods such as such as varying the air gap size and the proportion of the coil covered by the shorted turn. The previously described experiments will not only highlight potential pitfalls that should be avoided whilst designing shorted turns but also illustrate other methods of regulating the shorted turn effect for greater design flexibility.

M. A. Moser investigated the response of moving shorted turns within rotary voice coils in order to improve the actuator move time and power consumption (Moser, 1996); this was an extension of Chai and Lisser's work (Chai & Lissner, 1988) that showed that the shorted turn increased the coil current rise time, however within rotary systems the coil rise time is often short in relation to the seek time therefore stationary shorted turns only offer a minor improvement on seek times; it was however found that, within the type of rotary voice coil motor investigated, the shorted turn acts as a "brake" providing deceleration to both the acceleration and deceleration phases of its movement (fig. 2-5) (Moser, 1996). The majority of analysis was conducted via simulation using models of a voice coil motor with both

a moving shorted turn and a moving shorted turn with a slit through it; the latter increased the shorted turn resistance and prevented current from circulating, this was referred to as an open shorted turn. These systems were then modelled and validated with measurements of impedance plotted on frequency response diagrams. Figure 2-4 shows coil impedance of the voice coil, at frequencies below 100Hz there is a rise in coil impedance which is not typically evident in static coil analysis; Moser suggests that this was due to the back EMF, due to the movement of the actuator, reducing the net voltage apparent to the coil, thus causing an apparent impedance rise. There was a marked difference between the frequency response of the closed and open shorted turn with the open shorted turn consistently producing larger impedances at both high and low frequencies, however within the mid-range frequencies of around 100Hz to 1000Hz the open shorted turn was comparable to that of a closed shorted turn (fig. 2-4).

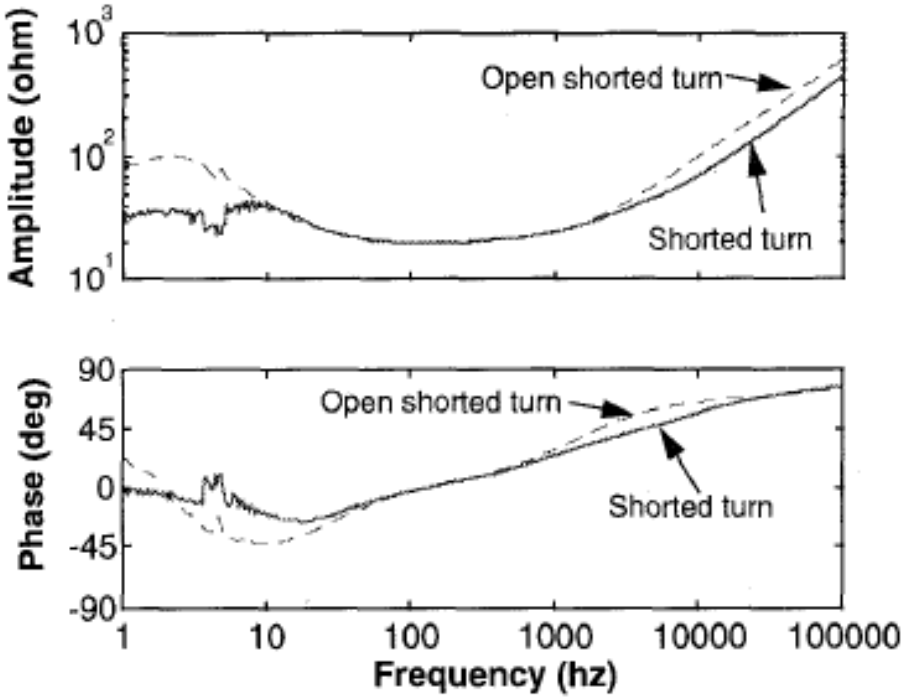

Figure 2-4. A simulated Bode plot of impedance, comparing an open and regular shorted turn *(Moser, 1996) – IEEE.*

Moser's work showed that a shorted turn reduces the high frequency coil impedance in relation to the open shorted turn; however the research also demonstrates that a

shorted turn may degrade the performance of an electromechanical device with a lower actuator velocity (fig. 2-5).

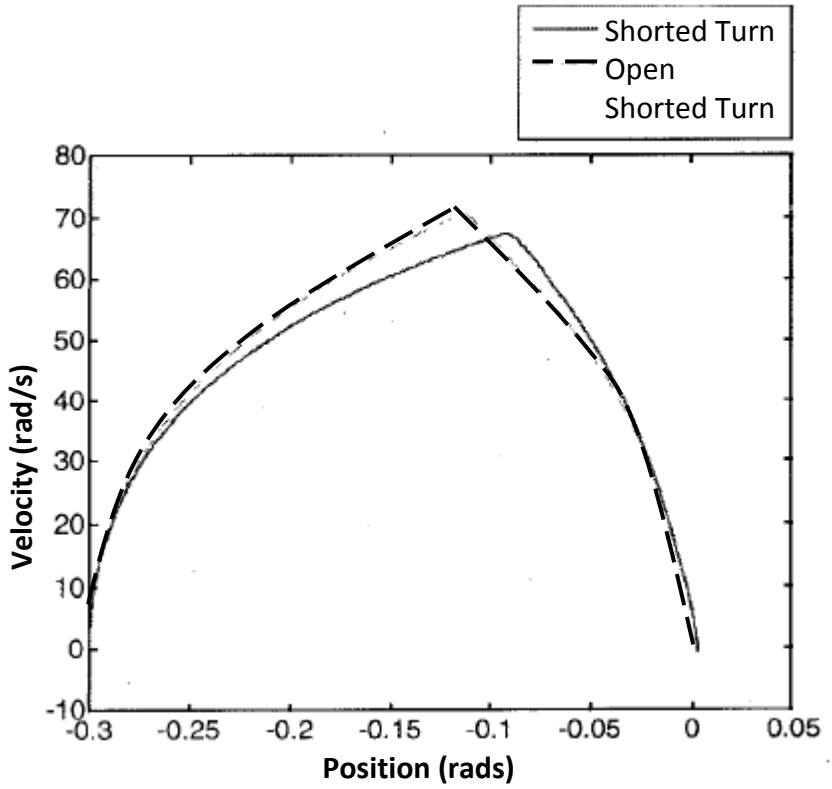

Figure 2-5. Simulated trajectories of a rotary voice coil motor with a shorted turn (solid) and an open shorted turn (dashed) *(Reproduction from Moser, 1996 – IEEE).*

Since the open shorted turn modifies the shorted turn behaviour by significantly increasing its resistive properties, this suggests that by varying the resistance of a shorted turn it may be possible to dynamically control or switch on or off the shorted turn effect; dependent on the application this may allow systems to maximise the benefits of a shorted turn whilst limiting the negative impacts. For example in figure 2-5 this would relate to using a "switched off" shorted turn to maximise acceleration but a "switched on" shorted turn for the deceleration phase for a reduced seek time; the feasibility of controlling a shorted turn will be analysed within this thesis.

Previous papers have demonstrated the effect of a shorted turn on the transient current response; however Hanson et al. demonstrated that a shorted turn may produce a reduction in coil impedance and phase lag specifically in the higher

frequency range (Hanson, Brown, & Fisher, 2001). Within this research an actuator's shorted turn produced a relationship between the actuator coil current and voltage that was not a typical LR first-order system (fig. 2-6). A third order Laplace transfer function was fitted to this the data and optimised in MATLAB (MathWorks, USA) although this may have been described by Wagner's transformer model (fig. 2-2 (Wagner, 1982)). It may be seen that the shorted turn reduces the phase lag of the coil admittance around the coil's breakpoint frequency, demonstrating that a shorted turn may also increase the dynamic range of an electromechanical device. As the shorted turn was present within the structure of the actuator, the effect of the shorted turn on the magnitude and phase of admittance was not investigated; therefore the effect of a shorted turn on the frequency response of a coil was investigated in much greater detail with analysis of the current response performed in the frequency domain to ascertain whether the shorted turn may produce the additional benefit of increasing stability margins.

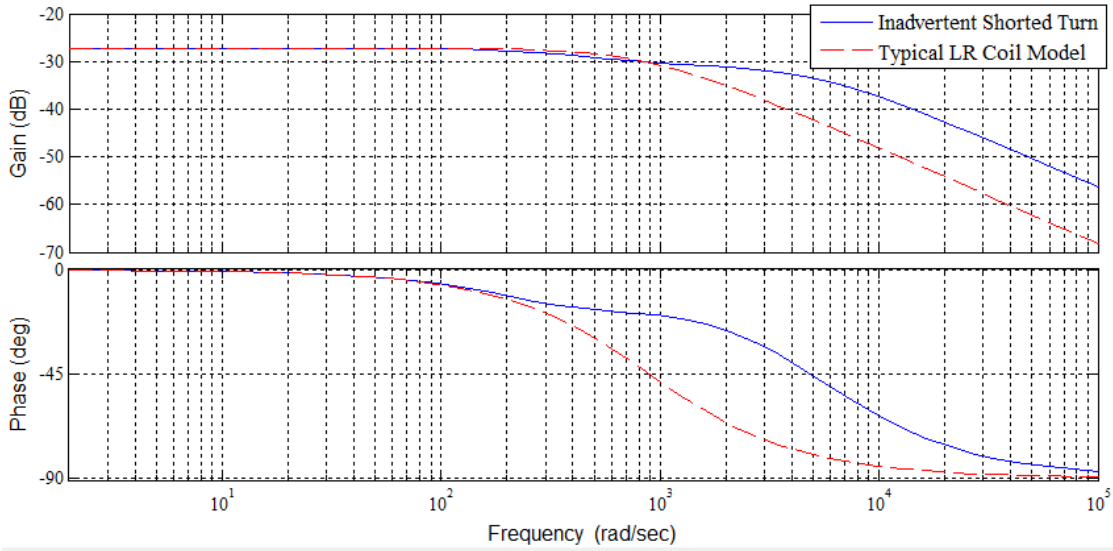

Figure 2-6. A frequency response of coil admittance of an inadvertent shorted turn, reproduced with permission from (Hanson et al., 2001)

2.2. IMPROVING DYNAMIC RANGE

As implied by Hanson et al.'s work, the shorted turn may also improve the dynamic range by increasing phase margins and producing an increased primary coil current to meet the a device's performance specification for a larger range of frequencies.

2.2.1. SYSTEM DAMPING

As described by figure 1-2 the system dynamics influence the total lag within an electromechanical device and thus the stability margins. Resonant effects will produce displacements of greater magnitudes and increase phase lags; reducing both gain and phase margins. Damping will reduce the amplitude of these larger displacements and although the transient response of the mover/rotor will be slowed, it would allow for greater gains to be applied, compensating for the slower rise time (Jaensch & Lampérth, 2007).

Damping involves dissipating energy from a system, in terms of vibration this means reducing the amplitude of each vibration. Systems are often unintentionally damped by elements such as friction and wind resistance. There are two types of dampers, active dampers which apply an external force such as a controlled actuator that actively applies a damping force to control vibrations; and passive dampers which dissipate energy from within the structure, such as within joints or with the use of an add-on damping device such as an isolator (which is a method of segregating an object from vibration) (Beards, 1996).

Yamada et al. produced an active vibration control system for a hard disk drive micro-actuator using a self-sensing actuator (Yamada, Sasaki, & Nam, 2004). The structural resonance mode of the read/write head and suspension is one of the major limiting factors in achieving even faster hard disk drive read/write head positioning times, Yamada's solution to this issue was an additional high bandwidth micro-actuator placed at the end of the read/write head assembly. A piezoelectric material was used to detect vibrations which were used by the controller to produce a self-

sensing damping system. This system produced good damping of the detected vibratory modes; however, the system did not detect all modes.

There is a wide range of mechanical damper types, such as dashpots; however, within an electromechanical system a convenient form of damping would be a non-contact technique such as eddy current damping, which may utilise the system's own magnetic fields to produce passive damping without mechanical wear. An eddy current, also known as a Foucault current after its discoverer León Foucault, is generated when an electrical conductor moves within a magnetic field. This movement induces a current which, due to Lorentz force, has a circular motion within the conductor. Lorentz force may be defined as the force acting on a charge in a magnetic field:

$$\mathbf{F_M} = q(\mathbf{v} \times \mathbf{B}) \tag{1.3}$$

Where $\mathbf{F_M}$ is the magnetic force, q is the charge of the particle, $\times$ is the vector cross product and **B** is the flux density (Benenson, Harris, Stöcker, & Lutz, 2002), (Lerner, 1997). Eddy currents are often inadvertent creations and often undesirable (dissipating energy through a process called ohmic heating).

Sodano and Inman performed research into eddy current damping by modelling a non-contact active eddy current damping system and gathering experimental data to gauge the accuracy of the model (Sodano & Inman, 2007). The system design utilised a conductive sheet attached to the end of a cantilever beam with an electromagnet directly under it; this allowed eddy currents to be generated by varying the current in the coil in relation to the vibration of the beam, with the damping force actively controlled based on the results of a positive feedback control system. This controller utilised second order digital filters that were based on three parameters: the damping ratio, filter frequency and controller gain that were required to be determined in advance to apply maximum damping to the structure. However, the use of filters with such a complex algorithm was a major disadvantage of the design as in practical terms this severely limited the flexibility of the system. Sodano and Inman's paper showed that it was possible to generate controlled damping forces by sensing the velocity of the vibrating structure and using that to control the coil current for eddy current generation; demonstrating the potential of eddy current

damping to reduce resonant peaks (see fig. 2-7) and increasing stability margins. However as many electromechanical devices are already driven by control systems, the extravagant setup offered no apparent benefits over the simpler negative velocity feedback.

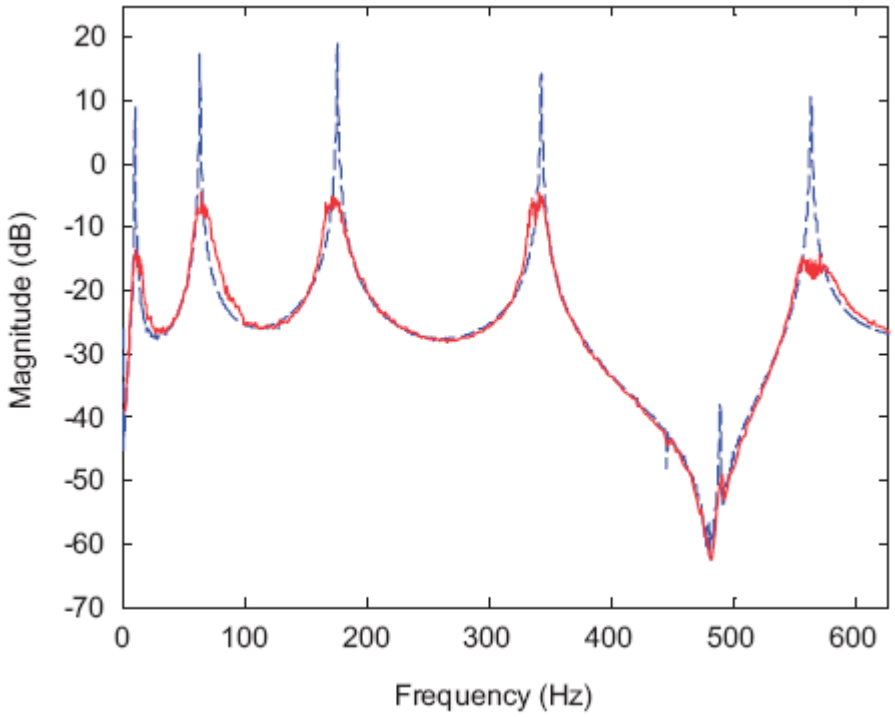

Figure 2-7. Experimental control of a cantilever beam's first five modes: --, uncontrolled and -, controlled *(Sodano & Inman, 2007) – Elsevier.*

A passive method of eddy current damping was presented by Bae, Kwak and Inman (Bae, Kwak, & Inman, 2005). This passive method of eddy current damping built on the experimental work of Kwak et al. (Kwak, Lee, & Heo, 2003) by producing an eddy current damping system with the use of a copper plate fixed to a cantilever beam and situated between two permanent magnets. The movement of the cantilever and in turn permanent magnets cause eddy currents to be developed within the copper plate. This was shown to be a very effective method of damping vibrations as may be seen from figure 2-8 where the resonant vibrations of the cantilever beam were suppressed (Bae, Kwak, & Inman, 2005).

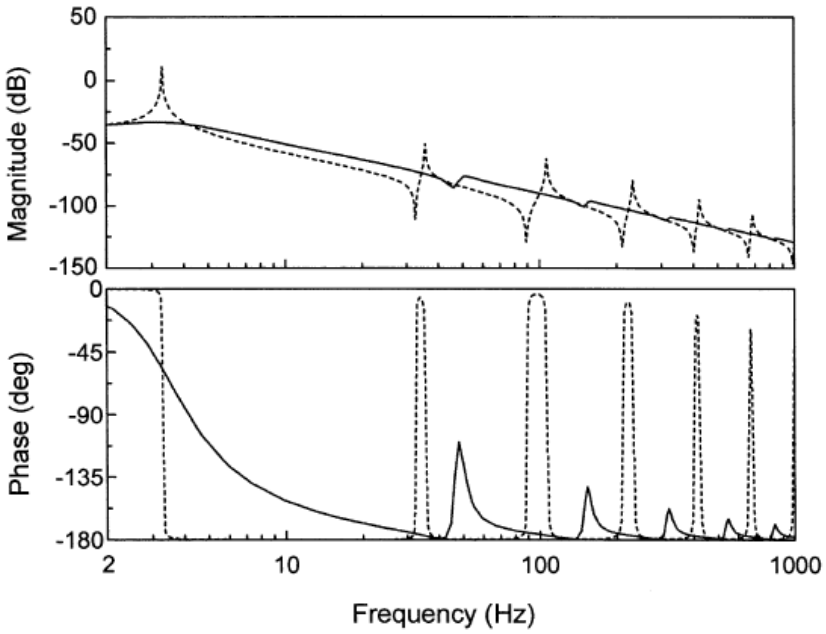

Figure 2-8. Frequency response plots: ——— Eddy current damping on; ------- Eddy current damping off *(Bae, Kwak & Inman, 2005) – Elsevier.*

The main limitation of Bae, Kwak & Inman's system was that the level of damping was not controllable as the damping forces are intrinsically linked to the cantilever displacement. Nonetheless this form of passive eddy current damping may be applicable to many electromechanical devices with careful design to control the magnitude of damping, as eddy currents are often generated within the device casing (Kirtley, 2010).

Due to the commercial appeal of eddy current damping, numerous patents have been filed on the subject with a range of novel designs and applications (Hofmann, Howe, Iorillo, Reiter, & Rubin, 1974), (Thompson, 2003) & (Bandera, 1998). Bandera patented some of the most relevant work on eddy current damping; this involved using eddy currents to produce damping forces within a motor (Bandera, 1998). A cylindrical current conducting member, attached to the motor armature, was arranged in such a way that it moved perpendicularly to the magnetic flux within the air gap to induce eddy currents and damp the velocity of the armature. Theoretically, dependent on the type of electromechanical device, the application of a shorted turn could also produce damping effects as this is also a cylindrical conductive member.

Therefore, within this thesis there will be an investigation into the feasibility of using a shorted turn as a damper.

2.2.2. OTHER METHODS OF IMPROVING ELECTROMECHANICAL PERFORMANCE

Electromechanical systems use the energy density of electrical and magnetic fields to generate a force on a rotor or a mover (in linear systems) and produce movement. More complex devices, such as those that require the force production over a longer stroke, often utilise 3 phase systems. These require complex control systems to allow smooth commutation from phase to phase producing a smooth movement of the rotor or mover. More complex control systems will, assuming the controller microprocessor speed remains constant, increase the time delay of $\mu_C P$ in figure 1-2 (the controller processing) reducing stability margins. Failure to correctly commutate phase to phase also will cause an increase in torque ripple reducing the dynamic range of positioning type electromechanical devices (Mir, Elbuluk, & Husain, 1997). Due to the controller processing ($\mu_C P$), control and positioning at higher frequencies becomes much more challenging due to the shorter period between changes in current demand.

Delays and lags may particularly limit the controller bandwidth where the controller is being utilised in a negative velocity feedback setup. Negative velocity feedback may be described as a controller actively damping a system by measuring the velocity of the mover/rotor and then applying a proportional force in the opposite direction, damping the motion. As the frequency of operation increases, any time delay between measuring the velocity of the mover and applying a proportional force will become more significant until the direction of the velocity will not be the same as that of the force application; this would transform negative velocity feedback into positive velocity feedback, accelerating the mover instead of damping the motion and possibly causing overshoot and instability (Walsh, 1992).

Filters may be used to reduce the burden on the controller by blocking disturbances, the however filters introduce lags to a system negatively effecting stability margins. There are however certain situations in which stability margins may also be

improved by good filtering, for example where well designed analogue filters are used instead of disturbance compensation, the additional latency within the controller caused by the processing of the disturbance compensation would be removed, potentially increasing the phase margin (Gonzalez & Woods, 2007).

Numerous patents have been filed on filtering within electromechanical devices, with many utilising adaptive filter designs (Semba, Kagami, & Tokizono, 2001), (Duttweiler, 1999) & (Skidmore & Proulder, 2004). Filter use typically requires knowledge of the range of frequencies to be attenuated; however, adaptive filters overcome this limitation. Jia et al.'s patent (Qingwei, Mingzhong, Kiankeong, & Jianyi, 2008), a "Random vibration and shock compensator using a disturbance observer" was a data storage device capable of compensating for physical disturbances, such as the disturbance caused by jogging with a mp3 player encasing a hard disk drive; this used a disturbance observer to "monitor" and adjust the filter to attenuate such disturbances. This patent highlighted the potential benefits of filtering within electromechanical devices.

The studies described to date have worked in a similar way, using an algorithm to predict control loop conditions and modifying the filter accordingly; and although usage within the research tended to focus on only one type of electromechanical device, hard disk drives, it did show that filters could be used to produce attenuation of resonant conditions within electromechanical devices. Adaptive filters for the purpose of improving stability margins will not be covered throughout this thesis as they require complex control systems bringing them outside the scope of this research which is more about passive approaches.

Reviewing prior work has helped to identify a range of methods that may be useful in improving the dynamic range and performance of electromechanical devices: improvements such as enhanced control system performance, the application of damping and reduction of high frequency coil impedance. However, from all the methods reviewed, a shorted turn may potentially encompass all of these factors, reducing lags for improved stability margins and larger controller gains, producing a faster transient response and potentially offering non-contact eddy current damping. There have been many studies on shorted turns; however, there has yet to be a study

on the effects of a shorted turn encompassing all of these aspects. Therefore, the focus of this thesis is to produce a more comprehensive study of shorted turns in comparison to other research, highlighting design considerations for the use of shorted turns.

3. Experimental Design

This chapter introduces the key principles behind the experimental design, the development of a test rig and analytical methodologies followed to investigate the effect of shorted turns on the performance of electromechanical devices. A transfer function is derived to describe the shorted turn, which will be used throughout the whole investigation. Its influence on the primary coil will be given along with details of any analytical techniques that may assist shorted turn design.

3.1. TEST RIG SETUP

A flexible, modular test rig was designed to simulate the behaviour of a range of generic electromagnetic devices with the aim of ascertaining how modifications to the coil's frequency response (as characterised by the low-power current response experimentation) would be expressed in terms of dynamic performance.

The basis of the test rig design was a series of permanent magnet devices in a linear configuration, as it was considered that this type of device was the most generic. Many electromechanical devices such as voice coil motors (VCM's) and rotary motors, which may be described as rolled up linear motors (fig. 3-1) (Boldea & Nasar, Linear Motion Electromagnetic Devices, 2001), work on the same principles of interactions between permanent magnetic fields and electromagnetic coils (equation 3.1). This is a contrast to induction motors (Jacek, 1994) however the effects of a shorted turn on coil impedance will also apply in the case of induction motors.

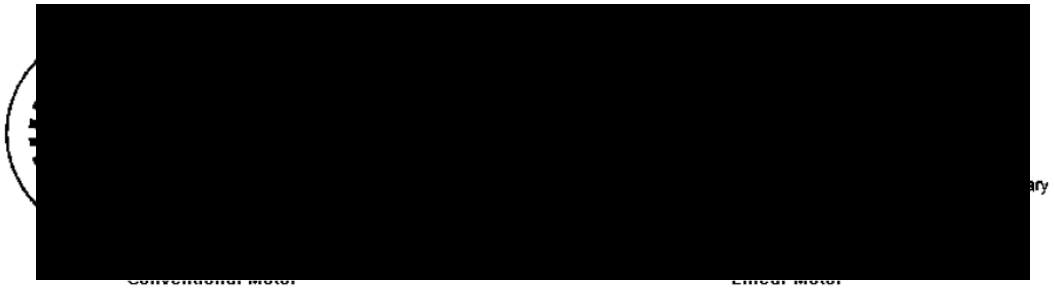

Figure 3-1. Design of a single sided linear induction motor – *(Viet Nam Hoang, 2003) Pemisiion pending.*

Boleda and Nasar showed that, for practical use, permanent magnet devices may be separated into two categories (configurations A and B) (Boldea & Nasar, Linear Electric Actuators and Generators, 1999). Configuration A which is based on the principle of flux alignment; whereby the poles of a magnet will attempt to align themselves such as a brushless DC motor (fig. 3-2) (Hughes, 2006). And Configuration B is based on the Lorentz force principle:

$$F = BIL \tag{3.1}$$

Where the force on the wire (F) of length (L) is directly proportional to the current within it (I) assuming a constant magnetic flux density (B) and that the direction of current within the wire remains the same relative to that of the magnetic flux density around the wire. Configuration B may either be configured so that the coils are fixed and the permanent magnet producing the magnetic field moves, as within the test rig (fig. 3-3), or in such a way that the magnets are fixed and the wire moves, as in a moving coil loudspeaker (Brice, 2001).

The setup used in the test rig was a simple single phase, single stator permanent magnet and coil arrangement. This was selected for simplicity and due to the fact that it was a more generic arrangement than multi-pole, multi-phase systems; as many devices such as voice coil motors use a similar permanent magnet and coil setup. Even though the arrangement was not designed to replicate the behaviour of induction motors (as there was no squirrel cage or reaction plate) the effects of a

shorted turn may also be analysed as the current and force responses will give a good idea of how the magnetic field is reacting to the shorted turn and whether or not more current would be induced into the conductor causing more force to be generated and improved performance.

Configuration A was produced within the testing rig by winding a coil around a core of high permeability relative to air to significantly increase the flux density. When this configuration was energised the stator became an electromagnet whose poles (based upon the direction of coil current) attracted or repelled a permanent magnet. This is detailed in figure 3-2. More in depth analysis of the interaction between magnetic fields and the force on the mover is described in section 3.2.4.

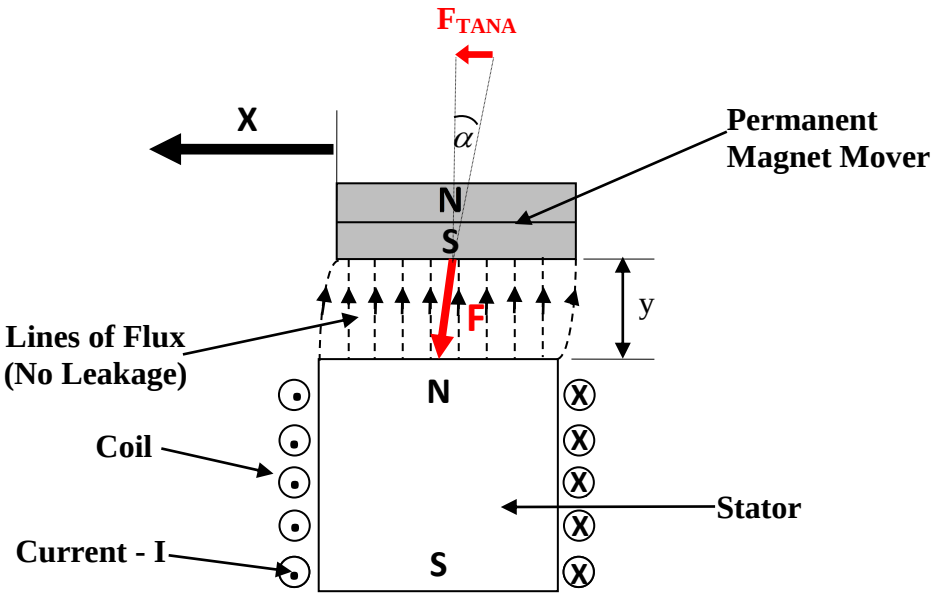

Figure 3-2. A diagram of Configuration A, a flux alignment design.

Configuration B was produced within the testing rig by placing a square coil underneath a permanent magnet mover. This mover had both a north and south pole facing a square coil that was arranged so that the direction of coil current, relative to that of the magnetic flux would produce a force on one side of the coil that would not oppose the other (fig. 3-5). A material with a high permeability relative to air (termed a coil cover) was placed beneath the coil to keep the flux as perpendicular to that of the coil current as possible with an aim of minimising flux leakage; the design of this coil cover is detailed in section 3.3.3.

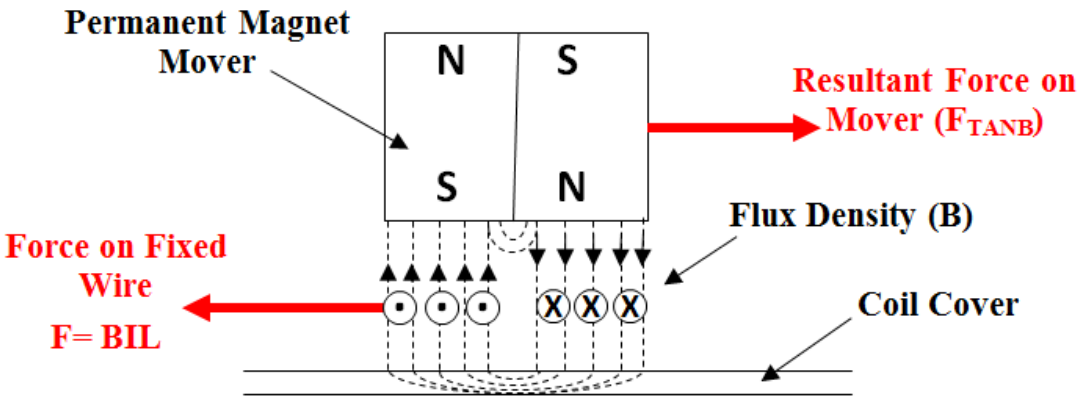

Figure 3-3. Diagram of Configuration B, a lorentz force design.

Configurations A and B were produced in experimentation using a testing rig. To simulate the mover of a linear electromechanical device a permanent magnet was suspended over a stator using flexures and a shaft. Flexures were selected to use rather than bearings as they offer very little resistance to motion and are extremely durable.

Producing a force on the mover as described by figures 3-2 and 3-3, shorted turn effects are achieved by placing aluminium cylinders over the coil. The effect of the shorted turn on force may then be measured by applying a force to the shaft such that it would push against the load cell; displacement measurements were achieved by removing the load cell and allowing the flexures to swing freely.

Detailed below is the test rig in configurations A and B and the parts used (figures 3-4, 3-5 and 3-6):

Configuration A

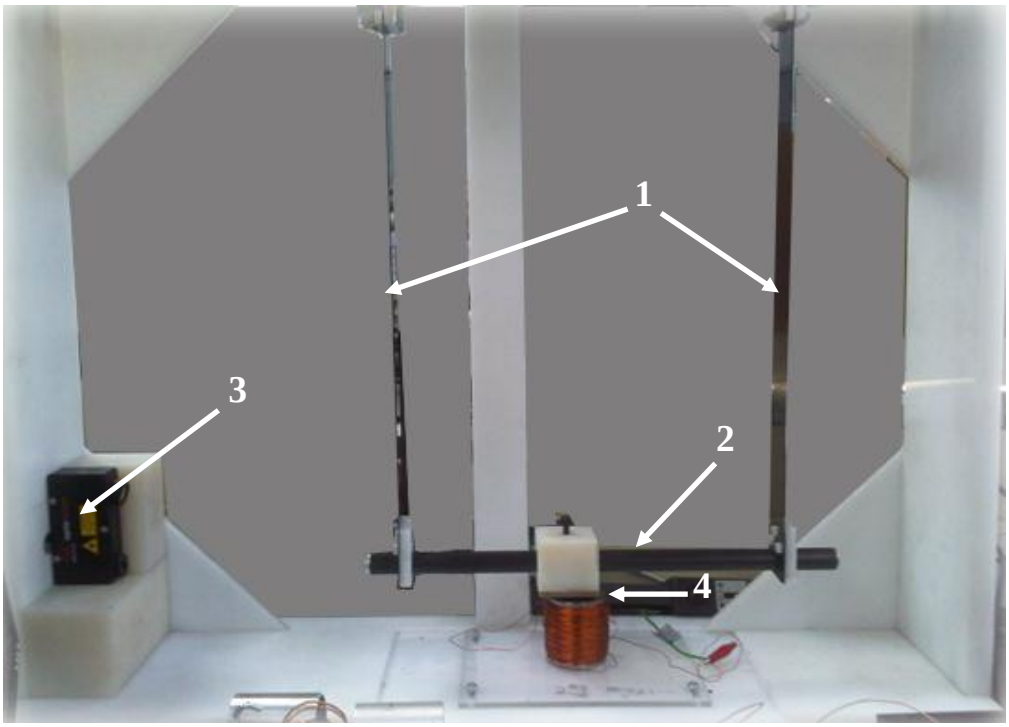

Figure 3-4. The test rig in configuration A set up for displacement experimentation.

Part No.	Description	Material	Notes
1	Flexures	50% Polyethylene Terephthalate (PET) and 50% Glass Reinforced Fibre	Flexures were used to ensure that the shaft moved with as little resistance to motion as possible, however a major disadvantage of flexures is that for any horizontal deflection there is a vertical deflection, therefore the flexures were long (500mm) relative to its maximum horizontal deflection (10mm each way) to minimise any variation in the air gap
2	Shaft	Carbon Fibre	The shaft was a hollow tube 20mm diameter and 400mm long. The length was selected as it allowed the flexures to be placed in such a way to minimise the shaft rotation around the Z-Axis whilst changing direction in dynamic tests.
3	Laser Sensor	N/A	A laser position sensor was selected for use within the test rig as it was able to measure the displacement of the shaft in a non-contact manner without disturbance to the magnetic field.
4	Air Gap	N/A	An air gap of 5mm between the permanent magnet face and the coil was chosen for the testing rig.

Table 3-1. Description of parts shown in figure 3.4

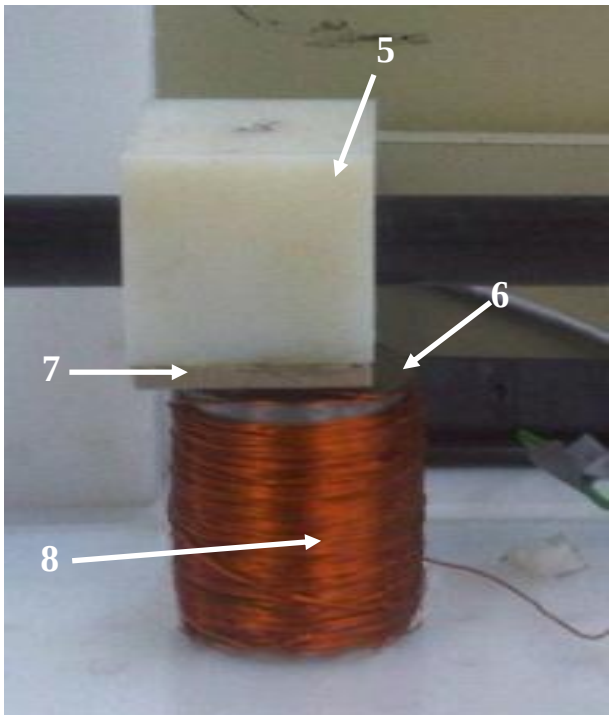

Figure 3-5. The mover and stator in configuration A

Part No.	Description	Material	Notes
5	Mover	Acrylonitrile Butadiene Styrene (ABS)	The width and depth were selected to be of the same dimensions as the permanent magnet and the height was selected to be large enough for the shaft to be placed through.
6	Stator	Iron	The stator core had a diameter of 50mm and height of 60mm; a high permeability core, with a relative permeability of 125 (μ/μ0) was used as it increased the flux density produced by the coil.
7	Permanent Magnet A	Neodymium N42	5mm thick and 50mm square producing a magnetic flux density of 0.11 Tesla. The permanent magnets had a maximum operating temperature of 80℃; therefore thermal analysis was conducted to ensure that the coil temperature would not exceed this value (section 3.2.1).
8	Coil A	Magnet Wire	Made from 22 AWG (American wire gauge) wire, 200 turns were selected as it would produce a magnetomotive force large enough to generate a significant force whilst not extending the flexures or bending the shaft

Table 3-2. Description of parts shown in figure 3.5

Configuration B

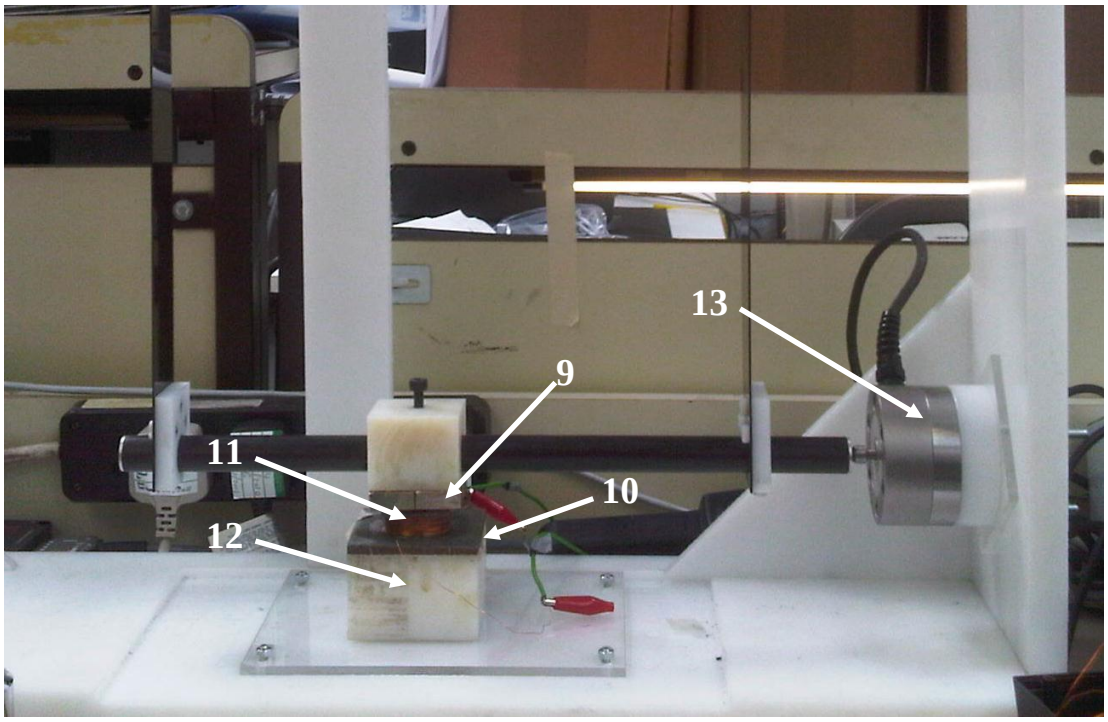

Figure 3-6. The test rig in configuration B set up for force experimentation

Part No.	Description	Material	Notes
9	Permanent Magnet B	Neodymium N42	Two 10mm thick, 50mm long and 25mm wide Neodymium N42 magnets, which producing a magnetic flux density of 0.22 Tesla each, were selected for configuration B. Arranged as shown in figure 3-3.
10	Coil Cover	Iron	The coil cover was a 100mm x 100mm piece of iron placed directly underneath the permanent magnet to create a path of low reluctance for a more uniform flux distribution
11	Square Coil	Magnet Wire	Made from 22 AWG (American wire gauge) wire and 10m of wire, The coil was oriented to be perpendicular to the lines of flux (fig. 3-3).
12	Coil Holder	ABS	The cover holder was 100mm x 100mm (to match that of the coil cover) ensured that the coil and coil cover stayed fixed firmly in position whilst a tangential force was applied to it.
13	Load Cell	N/A	The load cell was selected to match the test rig's ability to generate force (based on the calculations of section 3.2.4).

Table 3-3. Description of parts shown in figure 3.6

A high power setup was used to deliver large currents to the coil windings of the test rig and therefore maximise force production. The electrical setup used to achieve this is detailed in figure 3-7; this shows the test rig set up for force measurement whereby a digital acquisition device (DAQ) sends a demand signal to the amplifier (powered by a high voltage power supply) which outputs a large current to the coil. The input signal from the load cell/strain gauge amplifier is then obtained and processed to give a meaningful output.

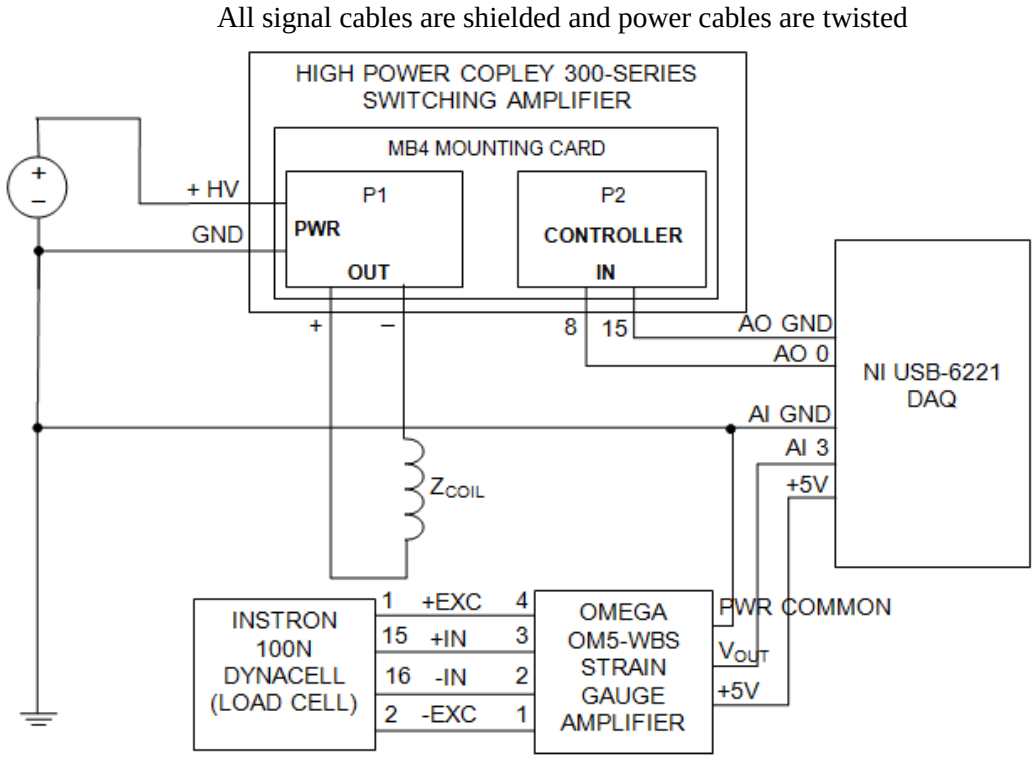

Figure 3-7. Wiring diagram of the high power experimental set up.

A low power set up was also used independently of the test rig to measure the current response without the possibility of back emf effects or significant coil heating. The electrical setup used to achieve this is detailed in figure 3-8; whereby an instrumentation amplifier is connected to a 5V power supply to produce voltages large enough for the DAQ to accurately measure up to 1000Hz

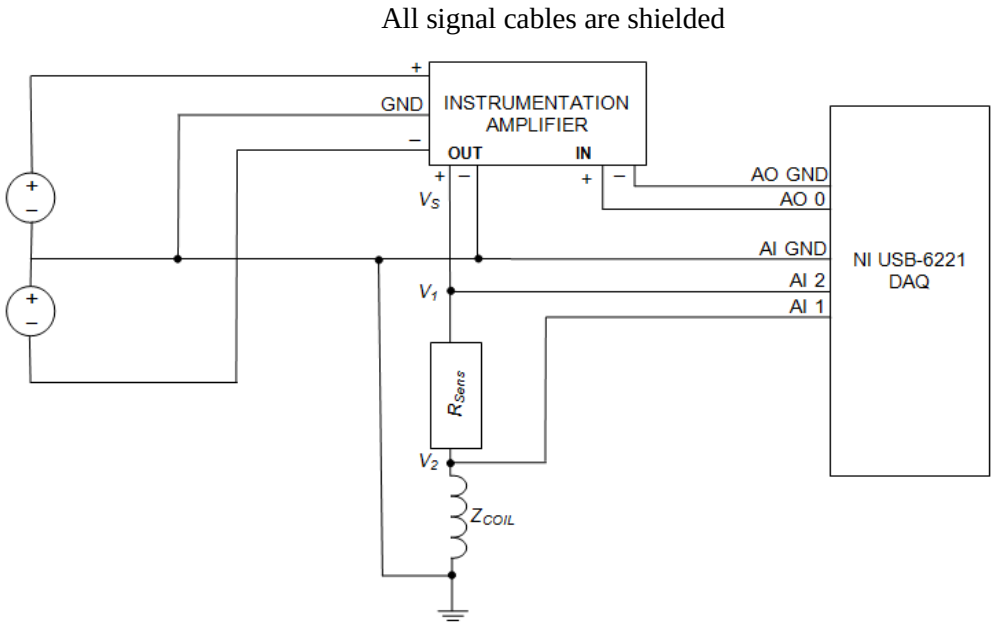

Figure 3-8. Wiring diagram of the low power experimental set up.

Figure 3-8 is a connection diagram detailing the experimental setup for investigation into the current response. The aim of the experimentation was to produce a Bode plot of primary coil admittance (Y_{COIL}), where coil admittance may be defined as:

$$Y_{COIL} = \frac{1}{Z_{COIL}} = \frac{I}{V} \tag{3.2}$$

Voltages were measured using a Digital Acquisition device (DAQ) and current obtained by measuring voltages across a 15.2Ω current sensing resistor (R_{SENS}) and across a coil with respect to ground; the coil current was then calculated using Ohm's Law:

$$I = \frac{V_2 - V_1}{R_{SENS}} \tag{3.3}$$

Where V_2 is the voltage between AI 1 and ground and V_1 is the voltage between AI 2 and ground. The value of the current sensing resistor (R_{SENS}) was chosen to approximate the DC resistance of the coil and minimise the magnitude of coil current to not (under 300mA) to prevent damage to the DAQ.

To investigate the effect of a shorted turn on the frequency response of admittance, a high Q (low energy dissipation) instrumentation amplifier was required. This effect was measured separately from and force/displacement effects, which were measured on a higher power test rig providing relative motion.

The Bode plot was produced using a custom computer program created in SignalExpress (National Instruments, USA) calculated the amplitudes and relative phases of the coil voltage and current, using a Fast Fourier Transform (FFT), through a frequency sweep of 3 to 1000Hz by applying a FFT to the acquired voltage and current waveforms. This program then automatically calculated complex coil admittance (defined by equation 3.2) at each frequency and produced a Bode plot of the frequency response. The program was also used to acquire the response of the coil to a step input of applied voltage.

3.1.1. OTHER EQUIPMENT

The next section details the main equipment used throughout the experimentation and the reasons for its selection.

Equipment	Use
A computer	Use to automate data acquisition; the only requirement of this computer was that it was capable of running MATLAB (MathWorks, USA) and SignalExpress (National Instruments, USA) and had a free USB port to connect the DAQ.
A NI USB-6221 Digital Acquisition Device (DAQ)	Used to generate and acquire analogue voltage signals; a minimum of 5 analogue inputs (one for each signal – Demand (V_D), Voltage (V_{COIL}), Current (I), Force (F)) and Displacement (x), 1 analogue output and a 5V DC power supply (to power the strain gauge amplifier) were required. The USB 6221 had a sampling rate of 250kHz meaning that each of the 5 signals, if processed simultaneously, would have a sampling rate of 50k Samples/Sec; therefore at 1000Hz (the maximum experimental frequency) each sine wave would have 50 samples, this would obey the Nyquist-Shannon criterion (Winder, 2002) however as the signal is not band limited (a signal which only has spectral density power within a giver range of frequencies (Allen & Mills, 2004)), therefore a filter may be required to prevent sampling effects such as aliasing.

A Tektronix TDS1000 series oscilloscope	Used to verify the DAQ's accuracy, as the oscilloscope had a significantly higher sampling rate of 100MHz compared to the DAQ's 250kHz; this would allow analysis of high frequency noise.
An Omega OM5-WBS strain gauge amplifier	Used to amplify the load cell output.
A Micro-Epsilon laser sensor	Used for non-contact displacement measurement; this was selected as its resolution of 0.02mm was sensitive enough to be able to produce a good measurement resolution in the 5mm – 0.5mm range that will be used for damping experimentation, whilst the range of 100mm was large enough to measure the mover and shaft moving over their full range. The measuring rate of 37kHz was also sufficiently in excess of the maximum test frequency of 1000Hz to ensure a minimal loss of accuracy.
A HIRST Magnetic Instruments GM08 gaussmeter (probe size: 1mm x 4mm)	Was also used to obtain readings for the magnetic flux density at specific parts of the system; this was useful for verifying calculations.

Table 3-4. Description of other parts of the test rig setup.

3.2. COMPONENT DESIGN

The following section details the design calculations used to select and design the test rig components.

3.2.1. COIL

The coils were designed to ensure that whilst operating at maximum power the system would not be damaged due to overheating and that whilst operating at maximum power the force produced would be sufficient based upon the criteria specified in the load cell design section (section 3.2.4).

Thermal Design

Under load conditions the coil current will cause the 22 AWG wire to heat, raising the coil resistance and increasing the possibility that the Neodymium magnet's maximum operating temperature of 80℃ would be reached. For this reason the coil heating was analysed by calculating the power generated by the coil and the heat transferred through the wire coating and convected into the permanent magnets. This was achieved through a using a thermal network model (fig. 3-9), (this model ignores any heat conducted through the iron core of the stator, which would only serve to increase the heat loss and lower the maximum temperature).

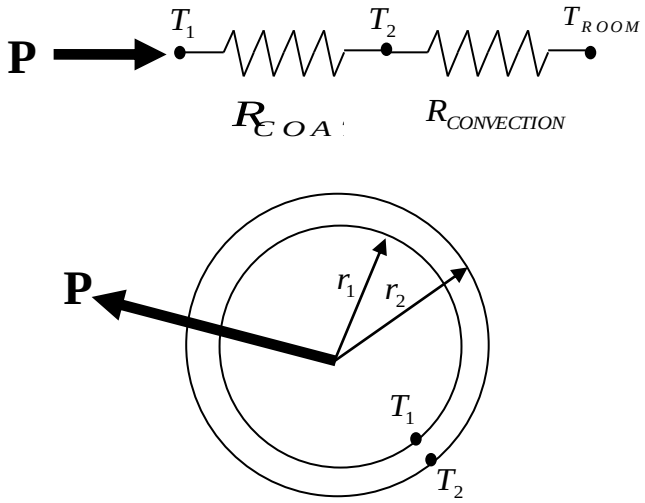

Figure 3-9. Model of coil heating with a single coated wire.

To calculate the maximum steady state temperature of the coil under continuous max current conditions, the power generated by the coil was given by:

$$P = I^2R \tag{3.4}$$

$$P = 7^2 \times 0.33 = 16.17W \tag{3.5}$$

Where R is the coil resistance and I is the maximum operating temperature of the coil.

The thermal resistance in the copper wire was then calculated using:

$$R = \frac{\rho L_{COILA}}{A_{WIRE}} \tag{3.6}$$

Where R is the resistance in Ohm's and ρ is the resistivity of copper (1.72 x 10^{-8}Ωm), L is the length of the coil in configuration A (31.41m) and A_{WIRE} is the area of the wire without the coating. Substituting values into equation 3.4 gave a resistance of 0.33Ω.

The thermal resistance due to conduction through the coating of the wire was given by (Incropera, 2007):

$$R_{COATING} = \frac{\ln(r_2/r_1)}{2\pi\kappa L_{COILA}} \tag{3.7}$$

Where κ is the thermal conductivity of the wire coating (0.15W/m), r_2 is the radius of coating and r_1 is the radius of the 22AWG wire. When values are substituted into this formula this gives a value of 3.38 x 10^{-3}°C/W.

To calculate the thermal resistance due to convection the following formula was used (Incropera, 2007):

$$R_{CONVECTION} = \frac{1}{hA_{COATING}} \tag{3.8}$$

Where h is the overall heat transfer coefficient of air (12W/m^2) and $A_{COATING}$ is the exposed area of the coating ($2\pi r_2 L_{COILA}$). Therefore by substituting values into equation 3.8 the resistance due to convection is 1.90°C/W.

The total thermal resistance is the sum of thermal resistance due to the convection and due to the wire coating:

$$R_{TOTAL} = R_{CONVECTION} + R_{COATING} \tag{3.9}$$

$$R_{TOTAL} = 1.9 + (3.38 \times 10^{-3}) = 1.90℃/W \tag{3.10}$$

The maximum temperature coil temperature was calculated by:

$$P = \frac{\Delta T}{R_{TOTAL}} \tag{3.11}$$

Assuming an average room temperature of 21°C:

$$T_1 = (16.17 \times 1.90) + 21 = 51.72℃ \tag{3.12}$$

Therefore with the system operating under continual maximum current conditions of 7A the system will only reach 51.7°C, significantly below the 80°C maximum operating temperature. At this operating temperature the coil resistance will also increase leading to greater I^2R power dissipation; the increased resistance is calculated by (Incropera, 2007):

$$R(T) = R_0(1 + \alpha\Delta T) \tag{3.13}$$

Where α is the temperature coefficient of copper ($0.0039K^{-1}$), R_0 is the initial coil resistance (0.33Ω) and ΔT is the change in temperature that caused the resistance change. This gives a new coil resistance at max power of 0.370Ω increasing the power dissipation to 18.1W and the maximum operating temperature to 55.4°C. As this is still significantly below the maximum operating temperature of 80°C, this suggests that even considering resistance changes due to coil heating the system will still not overheat under maximum current conditions.

Analysis was only conducted on configuration A as both configurations had the same maximum operating temperature but configuration B had a lower resistance (due to the shorter wire length) and therefore a smaller I^2R power dissipation, meaning that the maximum temperature reached by the system in configuration B will be lower than that of configuration A.

3.2.2. STATOR

The electromagnetic force, in configuration A, was generated by a stator consisting of an iron core and a coil. Low reluctance materials are generally selected for stator cores as they produce a greater magnetic flux density, they are however prone to

saturation. Saturation is where an increase in current will no longer cause an increase in the flux density; iron is normally designed to a maximum of 1.5T. This maximum flux density is given by summing the maximum AC and DC magnetic flux densities (3.14):

$$B_{MAX} = B_{AC(MAX)} + B_{DC(MAX)} \tag{3.14}$$

Within the test rig, the DC magnetic flux density ($B_{DC(MAX)}$) is equal to the permanent magnet flux density of configuration A (B_A) 0.15T (defined in section 3.3.4); therefore, the total flux density may be given by the following equation (Kothari & Nagrath, 2006) & (Kazimierczuk, 2009), where V_{RMS} is the root mean squared voltage, N is the number of coil turns, f_{MIN} is the minimum frequency that the system would be operated at and 4.44 is a constant derived from converting rad/s to Hz and voltage to root mean squared voltage:

$$B_{MAX} = \frac{V_{RMS}}{4.44 A_s N f_{MIN}} + B_A \tag{3.15}$$

Calculating V_{RMS} for the system operating under maximum current conditions (at 51.7^{o}C):

$$V_{RMS} = \frac{IR_{51.7℃}}{\sqrt{2}} = \frac{7 \times 0.37}{\sqrt{2}} = 1.83\text{V} \tag{3.16}$$

Therefore the minimum stator diameter required for configuration A to avoid saturation is given by:

$$A_s = \frac{V_{RMS}}{4.44(B_{MAX} - B_A) N f_{MIN}} \tag{3.17}$$

$$\emptyset_{SAT} = 2\sqrt{\frac{V_{RMS}}{4.44\pi(B_{MAX} - B_A) N f_{MIN}}} \tag{3.18}$$

$$\emptyset_{SAT} = 2\sqrt{\frac{1.83}{4.44\pi \times (1.5 - 0.15) \times 200 \times 1}} = 44.1mm \tag{3.19}$$

As a minimum stator diameter of 44.1mm was required to prevent saturation, when the system is operated at maximum current and at a frequency of 1Hz, a stator diameter of 50mm was chosen.

3.2.3. COIL COVER

The coil cover produces a path of least reluctance between the permanent magnets and the stator to keep the lines of flux perpendicular to the coil. This was made of iron, a high permeability material, which is also subject to saturation; therefore, modelling the coil cover as square in dimensions, equation 3.18 becomes:

$$w_{SAT} = \sqrt{\frac{V_{RMS}}{4.44(B_{MAX} - B_B)Nf_{MIN}}} \tag{3.20}$$

Designing the coil cover to saturation at 1.5T and using a permanent magnet flux density (B_B) as defined in section 3.3.4 of 0.28T, the minimum width is given by:

$$w_{SAT} = \sqrt{\frac{1.83}{4.44 \times (1.5 - 0.28) \times 50 \times 1}} = 82.2mm \tag{3.21}$$

As a minimum coil cover width, in a square design, of 82.2mm was required to prevent saturation, when the system is operated at maximum current and at a frequency of 1Hz, dimensions of 100mm x 100mm were chosen.

The aim of the coil cover was to guide the flux to as close to perpendicular to the square coil as possible, in order to minimise the normal and maximise the tangential component of force; to evaluate this a finite element model was created in COMSOL Multiphysics (fig. 3-10).

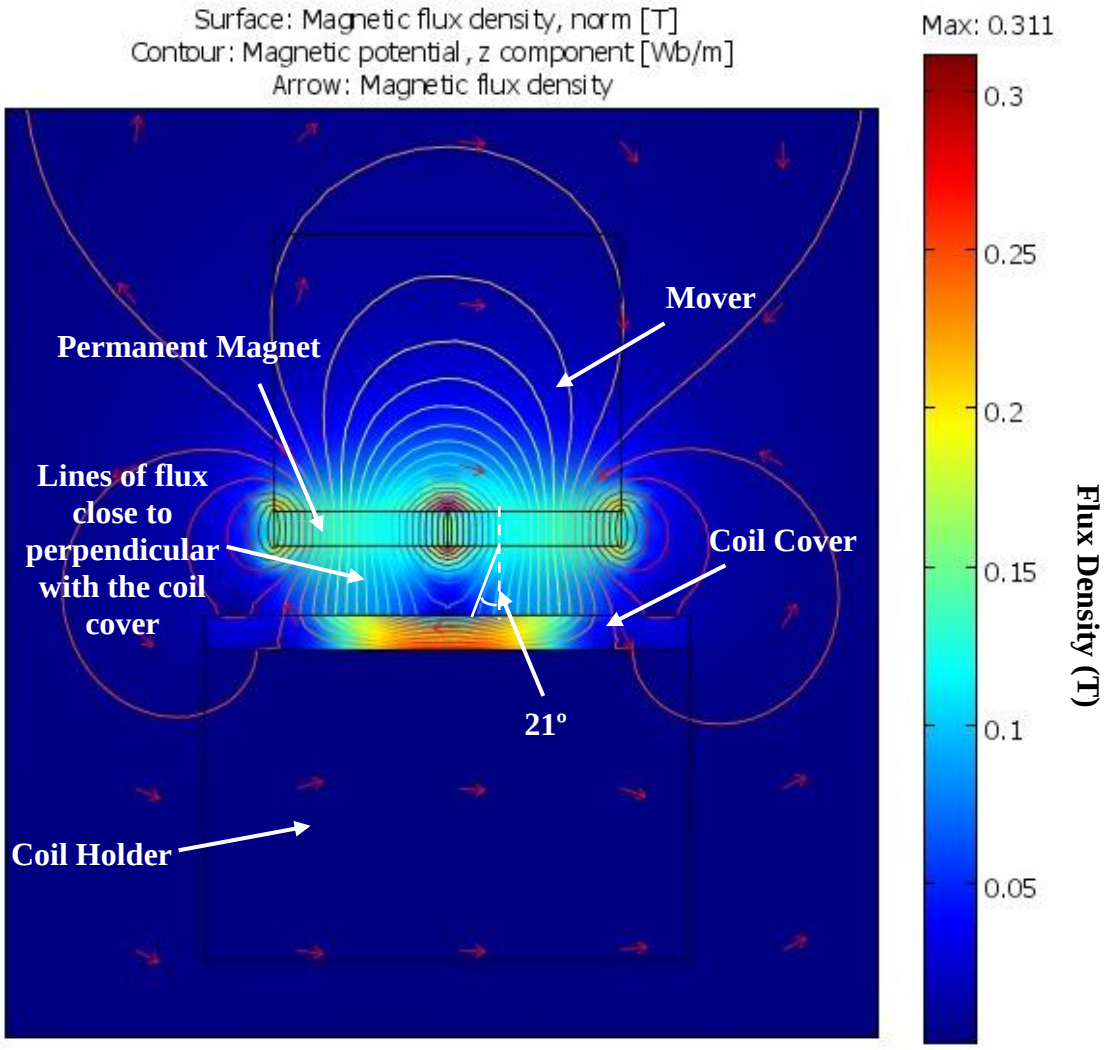

Figure 3-10. Finite element model of the coil cover, mover and permanent magnetic in configuration B.

Figure 3-10 shows that the lines of flux may be assumed to be perpendicular to the coil at the midpoint of the pole, however, according to the model, the lines of flux entering the coil cover from the permanent magnet will be up to 21 degrees off perpendicular, highlighting the necessity of correctly aligning the permanent magnet poles over the coil.

3.2.4. LOAD CELL

To calculate the range of load cell required for force experimentation, the total force acting tangentially was required. In configuration A this required summing the permanent magnetic and electromagnetic forces.

Normal Permanent Magnetic Force

To calculate the permanent magnetic force acting horizontally upon the load cell, first the normal force must be calculated (fig. 3-11); this may be calculated by first evaluating the stored energy in the magnetic field. Assuming that the magnetic field is uniform and that there is no flux leakage, the stored energy in the air gap may be calculated by multiplying the stored energy in the magnetic field by the volume of air in the gap (Hammond, 1997), (Sibley, 1996) & (Christopoulos, 1990).

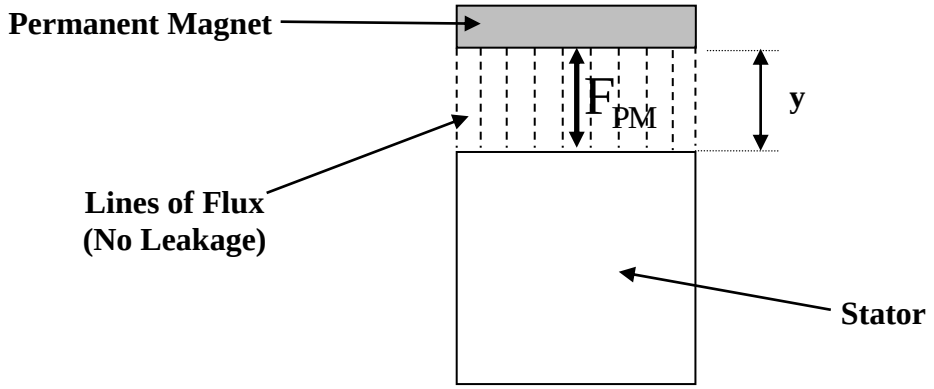

Figure 3-11. Model of the normal force created by the permanent magnet and stator.

The stored energy of the magnetic field in the volume of the air gap is given by:

$$W' = WV_{AG} = \left(\frac{B^2}{2\mu_0}\right)(yA_{AG}) \tag{3.22}$$

Where W' is the stored energy in the volume of the air gap, W is the stored energy of the magnetic field, V_{AG} is the volume of the air gap, B is the magnetic flux density, μ_0 is the permeability of free space, y is the height of the air gap and A_{AG} is the cross sectional area of the air gap.

Force is then equal to the change in stored energy in the volume of air gap per change in air gap height.

$$F_{PM} = \frac{dW'}{dy} \tag{3.23}$$

$$F_{PM} = \frac{B^2 A_{AG}}{2\mu_0} \tag{3.24}$$

Equation 3.24 is known as the Maxwell force equation.

The flux density in practice is dependent upon the reluctance of its magnetic circuit. For this reason the flux density was obtained experimentally using a gaussmeter, however experimentation with the gaussmeter revealed that the magnetisation of the permanent magnets were not constant across the length of the magnet. To investigate this further measurements taken with a gaussmeter at 5mm deviations along the face of the magnet to be used in configuration A.

Figure 3-12 shows the results of the permanent magnet flux density investigation plotted as a surface map; this showed that the corners of the magnet have the largest flux density whilst the centre point has the lowest flux density, suggesting that variations in the mover position throughout static experimentation may vary force output.

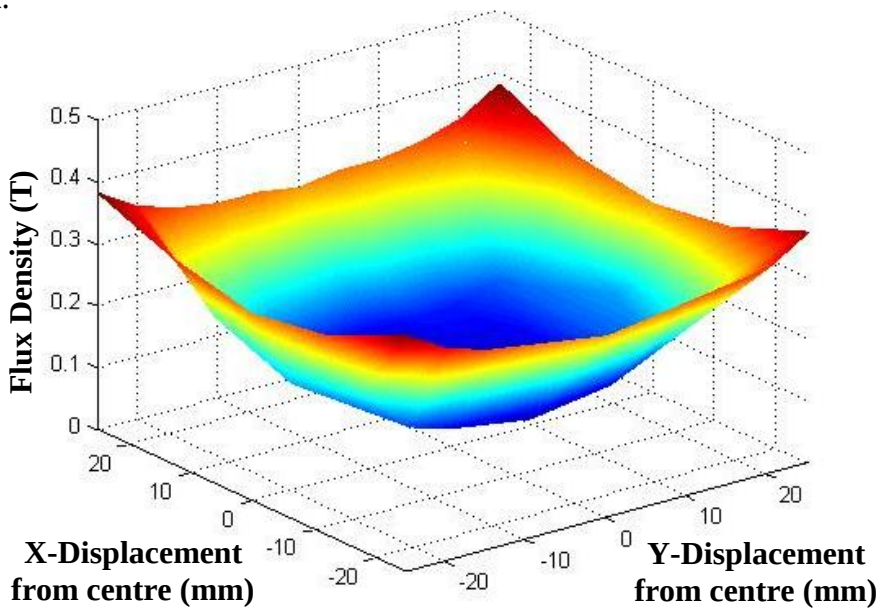

Figure 3-12. Surface map of the magnetic flux density over a Neodymium N42 magnet's surface (as used in configuration A)

As the flux density along the magnet's surface varies so significantly it was decided that the mean flux density of 0.15T was the best approximation to use for the proceeding calculations. Analysis was conducted with configuration B to obtain a mean magnetic flux density of 0.28T.

Substituting values into the Maxwell force equation (3.23) gives a value of 22.4N for the force created between the permanent magnet and stator in configuration A (F_{PM}).

Normal Electromagnetic Force

Since Ampere's Law relates magnetic fields to the electrical currents that create them, it may be used to derive a relationship for the normal electromagnetic force (Ida, 2004):

$$B_{EM} = \frac{MMF\mu_0}{y} \tag{3.25}$$

And combining with the Maxwell force equation (3.24); the normal force generated by the coil current in configuration A may be calculated by:

$$F_{EM} = \frac{MMF^2\mu_0 A_S}{2y^2} \tag{3.26}$$

Therefore the maximum normal force produced by the stator in configuration A (F_{EM}) will be 96.7N and the total force will be the sum of the normal force from the stator and the permanent magnet (F_{TOTAL}), 119.12N.

Tangential Permanent Magnetic Force

The tangential force was calculated by modelling the test rig with the permanent magnet and mover displaced a small distance from the stator (fig. 3-13). For small displacements the model was assumed to have a linear magnetic field and that there is no flux leakage and hence would be less valid as displacement increases.

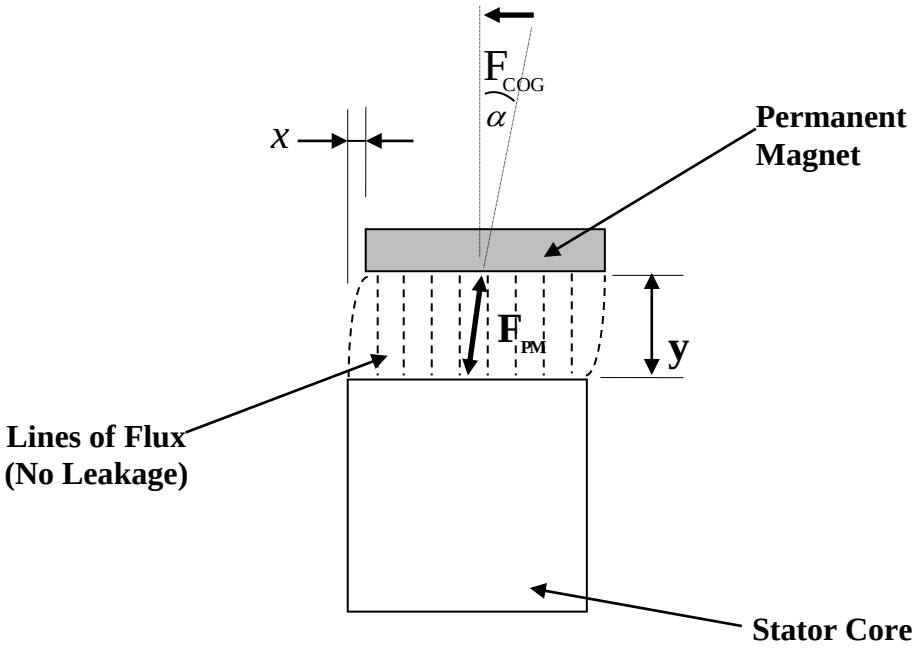

Figure 3-13. A model of cogging within the electromagnet test rig.

Finite element analysis was employed in order to investigate whether the assumption of no flux leakage was a fair approximation, by analysing the flux contours over a range of displacements. Figure 3-14 shows an example with a maximum displacement of 10mm from its central point, as shown by the contours there is some flux leakage (uncoupled flux) on the side displaced from the stator; however according to the contours the majority of the flux is coupled to the stator, therefore the assumption that there is no flux leakage is considered to be fair.

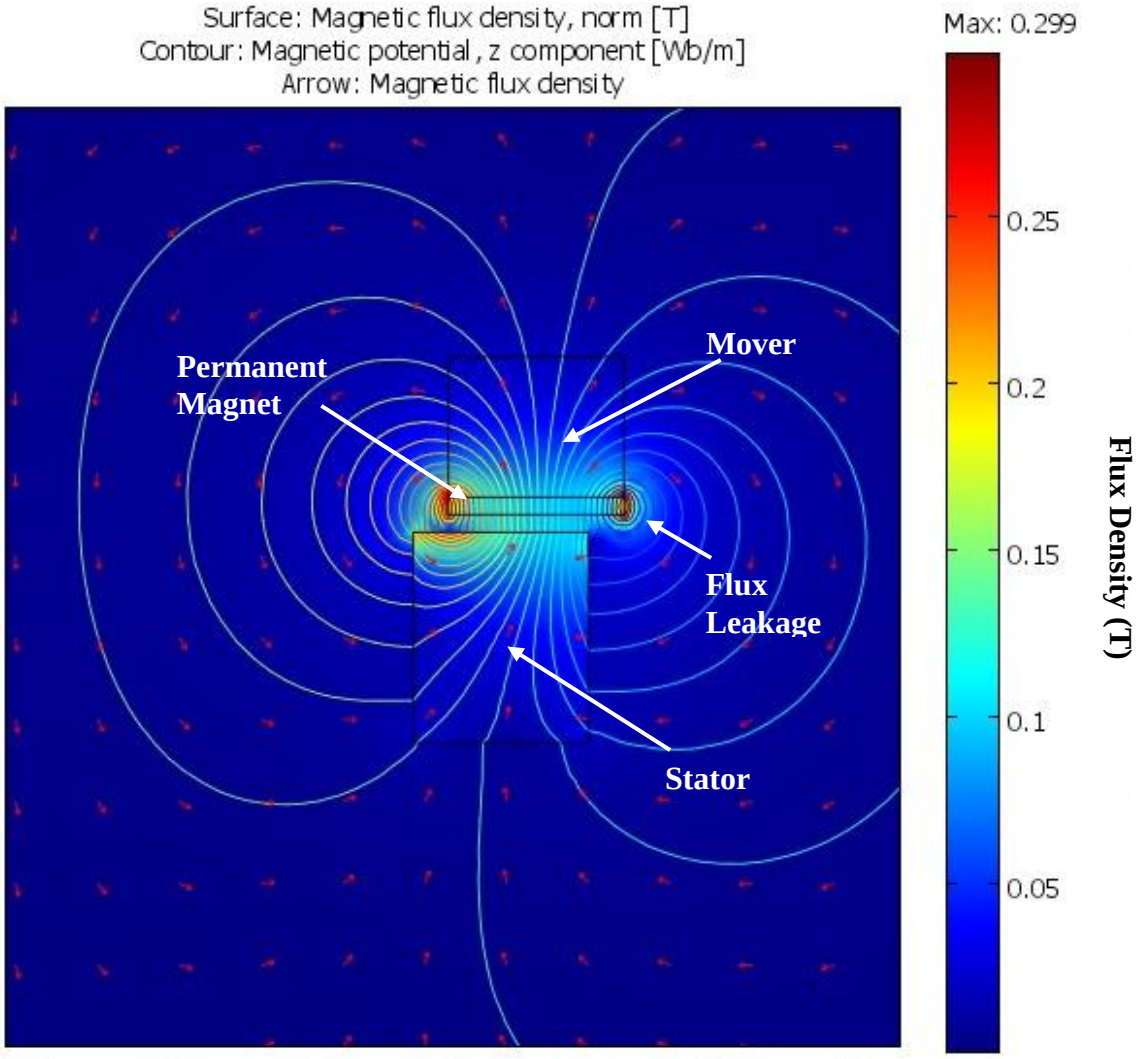

Figure 3-14. A finite element model of cogging within the test rig.

The tangential force is given by:

$$F_{COG} = F_{PM} \sin \alpha \tag{3.27}$$

Therefore the maximum tangential force (F_{COG}) was 106.5N; however, a load cell rated at 100N was selected as it offered greater sensitivities than the next larger (250N) load cell at small magnitudes of force, and it was expected that the actual maximum tangential force would be lower than 100N due to flux leakage.

Following the analysis of the coil cover (section 3.2.3) the lines of flux around the square coil may be assumed to be perpendicular at the midpoint of the pole,

therefore the maximum tangential force may be calculated using equation 3.1. This gives a maximum tangential force in configuration B of 19.6N, which is below the selected load cell rating of 100N.

3.2.5. AIR GAP

There was significant importance placed on noting any variations of the air gap between the stator and mover in configuration A, as the normal force between these two parts would change greatly based upon this value. This was of less importance with configuration B, however the greater the air gap the greater the flux leakage the less uniform the magnetic field would be.

As according to Biot-Savart's law (3.28) the magnetic flux density will reduce by the cube of the distance from the axis of the coil (Umashankar, 1989):

$$B(y) = \frac{\mu_0 I A_S}{2\pi y^3} \tag{3.28}$$

A maximum allowable total variation in the air gap (from flexure movement, shaft bending and flexure extension) was set at 5% which was equal to 0.25mm was considered to be a stringent but realistic criteria.

3.2.6. FLEXURES

Kinematic Flexure Analysis

The flexures were a significant contributor to variations in the air gap, as horizontal displacement of the flexures imposes a vertical displacement, shown in figure 3-16. A maximum range of 20mm (10mm each way) was selected for the flexures for a large signal to noise ratio in dynamic displacement tests; based upon this range, calculations were performed to note the maximum air gap variation due to flexure movement.

To calculate the maximum variation in air gap size it was necessary to understand the shape that flexure would take when deflected horizontally. As the flexures were clamped at each end the shape of the flexures would be an “S” shape (fig. 3-15a). However as the flexures are long compared to the size of the clamp and were also constantly under tension the shape was more comparable to a straight line (fig. 3-15b).

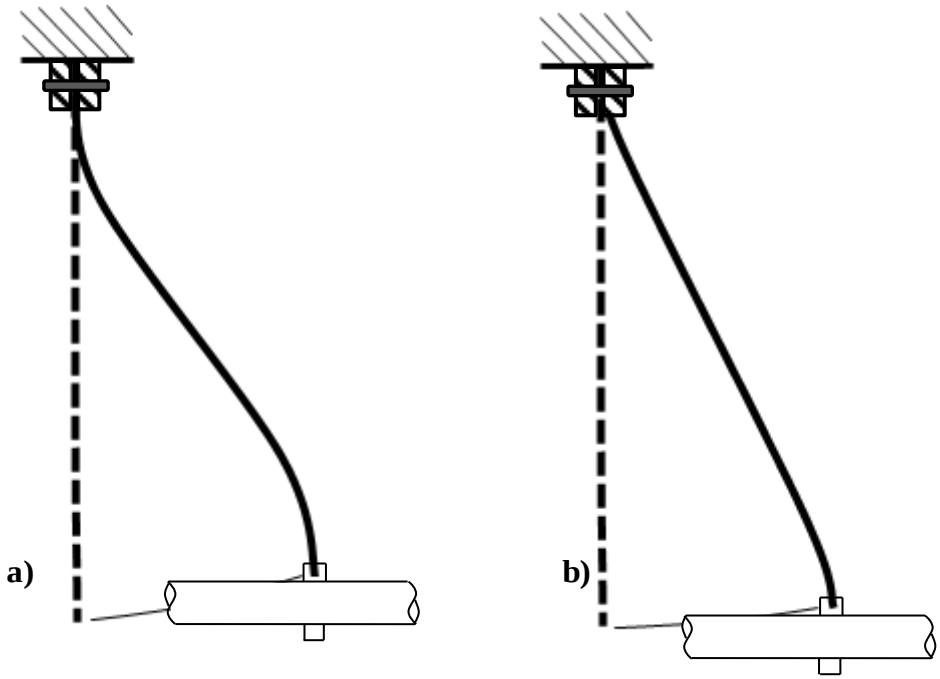

Figure 3-15. The shape of a) an unloaded flexure and b) a flexure under tension as it would be within the test rig.

Thus, assuming a straight-line approximation for the flexure, the variation of the air gap with respect to the horizontal deflection may be approximated using Pythagoras’ theorem (fig. 3-16).

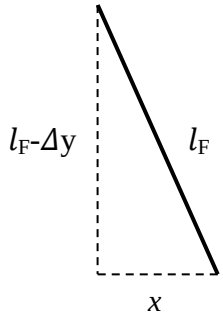

Figure 3-16. Flexure design using Pythagoras Theorem

Where:

$$\Delta y = l_F - \sqrt{({l_F}^2 - x^2)} \tag{3.29}$$

As the variation in air gap height due to the movement of the flexures were only of concern in dynamic tests, whereas issues of flexure extension and shaft bending would also be a factor in static tests, a larger proportion of the maximum 0.25mm variation in the air gap size was allocated to the movement of the flexures; 0.125mm. Substituting values into equation 3.29:

$$l_F = 400.1mm \tag{3.30}$$

A larger flexure length of 500mm was selected to further reduce the variation in the air gap whilst maintaining the overall desktop size. This meant that the maximum air gap variation was reduced to 0.11mm or 2.2% of the total air gap.

Flexure Extension

Extension of the flexures due to the forces acting upon it will also vary the air gap; the amount that each flexure will extend under the magnetic and gravitational forces was calculated by working out the stress acting upon it. The total extensional force (F_{EXT}) was calculated using:

$$F_{EXT} = F_{PM} + F_{EM} + M_{MS}g = 22.4 + 96.7 + 0.326g \\ = 122.3N \tag{3.32}$$

As the terms F_{PM} and F_{EM} are not applicable to configuration B, the maximum flexure extension would be in configuration A. The stress on the flexure was calculated using the following formula:

$$\sigma_F = \frac{F_{EXT}}{2t_F w_F} \tag{3.33}$$

Where F_{TOTAL} is the combined force from the stator and permanent magnet, M_{MS} is the mass of the mover and shaft, g is the gravitational field strength (9.81m/s^2), t_F is the flexure thickness (2mm) and w_F (20mm) is the flexure width (these values were

selected based upon numerous design iterations). Substituting values into equation 3.33 gives a stress on the flexure of 3.06MPa.

Assuming that the deformation is still elastic and therefore that the strain may be calculated using Hooke's Law:

$$\varepsilon_F = \frac{\sigma_F}{E_F} \tag{3.34}$$

Where σ_F is the stress on the flexure, ε_F is the strain of the flexure and E_F is the young's modulus of the flexures:

$$\varepsilon_F = \frac{3.057 \times 10^6}{25 \times 10^9} = 1.22 \times 10^{-4} \tag{3.35}$$

The extension of the flexure is therefore calculated using:

$$\Delta L_F = L_F \varepsilon_F = 0.057mm \tag{3.36}$$

This value meant that the air gap would vary by a maximum of 1.14% due to flexure extension (whilst applying maximal current).

3.2.7. SHAFT

Shaft bending would be another cause of air gap variation; following the calculation of the total extensive force (3.32), the amount the shaft will bend and the flexures will extend may be computed using the following model (fig. 3.17):

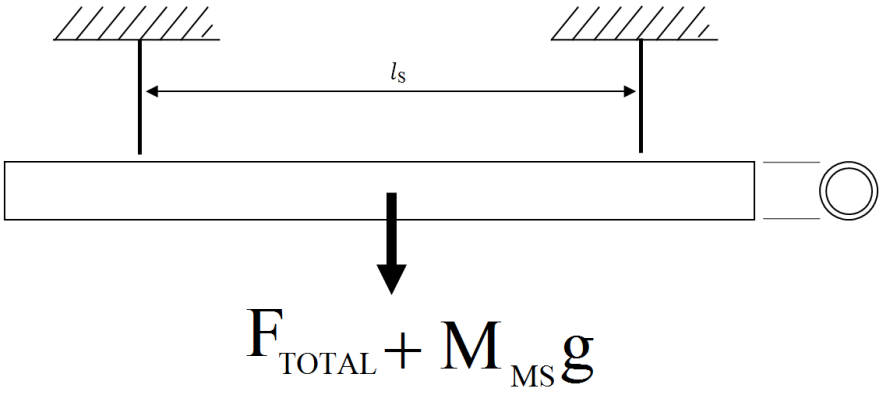

Figure 3-17. 3-Point bending model for the carbon fibre shaft.

The shaft deflection may be calculated using the Euler-Bernoulli beam bending equation for a simply supported beam with a load equidistant from the supports.

$$\delta_{MAX} = \frac{F_{EXT} {l_s}^3}{48 E_{SHAFT} I_A} \quad (3.37)$$

Where F_{TOTAL} is the load on the shaft, E_{SHAFT} is the young's modulus of the shaft (250GPa), L_S is the distance between supports (325mm) and I is the 2nd Moment of area where I may be calculated by:

$$I_A = \frac{\pi}{64}({\emptyset_0}^4 - {\emptyset_0}^4) \quad (3.38)$$

$$I_A = \frac{\pi}{64}((20 \times 10^{-3})^4 - (16 \times 10^{-3})^4) = 4.64 \times 10^{-9} m^4 \quad (3.39)$$

Therefore the maximum shaft deflection will be:

$$\delta_{MAX} = \frac{122.3 \times (325 \times 10^{-3})^3}{48(250 \times 10^9)(4.64 \times 10^{-9})} = 0.075mm \quad (3.40)$$

Therefore the maximum amount that the air gap would vary due to shaft bending, whilst applying maximal current, is 1.51%. This would give a total maximum air gap variation of 0.242mm or 4.84%.

3.3. MECHANICAL RESONANCE

The moving parts of the test rig comprise a mass (or moment of inertia), being subject to a restoring force (or torque) proportional to its displacement (or angle of rotation from its equilibrium position); hence, the system would be expected to exhibit lightly-damped oscillatory behaviour. If the frequency of an applied force (or torque) matches that of the natural frequency of this lightly-damped oscillatory behaviour resonance will occur.

In order to calculate resonance the system was modelled in the force experimentation set up, a blocked configuration (fig. 3-18). This is as in a free

configuration as used for displacement experimentation the natural frequency of the horizontal mode of vibration was lower than the minimum testing frequency.

$$\omega_n = \sqrt{\frac{g}{l}} = 0.71Hz \qquad (3.41)$$

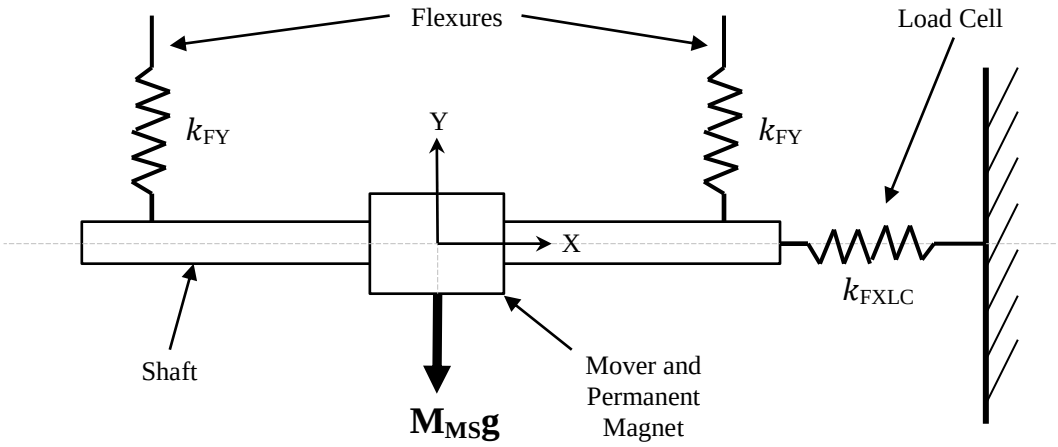

Figure 3-18. Test rig model of relevant inertias and stiffnesses for resonance modelling.

Modelling the test rig as a mass-spring-damper system (figure 3-18) and using Equation 3.42 (where 'k' is the stiffness of the system within the required mode and 'M' is the mass) the natural frequency of the X-Displacement and Y-Displacement Modes were calculated.

$$\omega_n = \sqrt{\frac{k}{M}} \qquad (3.42)$$

The resonant frequency (ω_R) is given by (Magee & Tooley, 2005):

$$\omega_R = \omega_n\sqrt{1 - 2\zeta^2} \qquad (3.43)$$

Where ζ is the damping ratio, defined as:

$$\zeta = \frac{c}{2M\omega_n} \qquad (3.44)$$

However as the damping ratio is much less than 1 the resonant frequency is approximately the natural frequency.

To calculate X-Displacement mode, the stiffness k_{FXLC} (the stiffness of the load cell and flexure when deflected along the x-axis) and k_{FY} (the flexure stiffness in the direction of the y-axis) were required. Since the load cell was almost rigid in comparison to the flexures, the flexure stiffness was negated and only the stiffness was calculated. The load cell gave a deflection at full load (100N) of 50µm (using the manufacturer's data sheet), it therefore followed that the stiffness of the load cell was 20MN/m.

To calculate the Y-Displacement mode, the flexure stiffness k_{FY} was derived from Hooke's Law stress-strain relationship (eq. 3.45); where L is the flexure length tangentially to the axis of the resonant mode; A is the flexure cross sectional area and E is the young's modulus (25GPa).

$$k = \frac{L}{EA} \tag{3.45}$$

The stiffness of the bending modes were calculated using Euler-Bernoulli beam bending equations; based on figure 3-18, Y-Bending was calculated by modelling the shaft as a simply supported beam (section 3.2.7), rearranging equation 3.37 the stiffness of Y-Bending is given by:

$$k = \frac{48E_{SHAFT}I_A}{{l_s}^3} \tag{3.46}$$

I_A (the second moment of area) of Y-Bending is defined by equation 3.38.

Using a similar technique for Z-Bending but was modelled as a cantilever beam instead of a simply supported beam:

$$k = \frac{3E_F I_A}{{l_F}^3} \tag{3.47}$$

Where I_A for Z-Bending is given by the following equation:

$$I_A = \frac{bd^3}{12} \qquad (3.48)$$

The mass of the mover, permanent magnet and shaft were found to be 0.3263kg in configuration A and 0.4029kg in configuration B; substituting these measurements along with the values of stiffness, into the equation 3.42, the natural frequency may be obtained for each displacement mode.

The calculated natural frequencies are shown in table 3-1 (verified in section 4.3.2).

	Configuration A Natural Frequency (Hz)	**Configuration B Natural Frequency (Hz)**
X-Displacement Mode (f_{RDX})	394.0	354.6
Y-Displacement Mode (f_{RDY})	410.4	369.0
Z-Bending Mode (f_{RBZ})	62.1	55.9
Y-Bending Mode (f_{RBY})	354.8	319.3

Table 3-5. Resonant frequencies of configurations A and B.

3.4. EXPERIMENTAL VERIFICATION

Minimising noise and distortion within the experimental signals was of significant importance for measurement of voltage, current, displacement and force. As the majority of coil experiments were conducted in the frequency domain, the magnitude of a signal from a coil will reduce with frequency (after it's breakpoint frequency) due to the inductive reactance of the coil. This meant that as the signal power drops at high frequencies, without a sufficient signal to noise ratio, the signal would become mostly noise and distortion. A series of experiments were conducted to ensure that the signals produced were the correct representation and to quantify the noise and distortion. This section explores some of the processes that were used to ensure that the signals obtained were an accurate representation of the system.

3.4.1. LOW POWER EXPERIMENTAL SETUP SIGNAL ANALYSIS

A low-power test rig was used for experimental investigation into the frequency response of admittance. This setup was used in order to prevent back EMF production due to the test rig in motion and other effects present in high power applications such as saturation. To conduct the current response experimentation, a coil was wound and surrounded by a removable close-fitting aluminium cylinder to create a shorted-turn effect. The coil resistance was measured using an Ohmmeter. The inductance was then identified by measuring the frequency-response of impedance and applying a 1st-order RL coil model, with L optimised to match the breakpoint frequency. This gave a coil resistance (R_1) of 22.9Ω and a self-inductance (L_1) of 18mH.

The low power experimental setup relied on accurate voltage measurement. The accuracy of these voltages was verified using both the DAQ and oscilloscope. The majority of measurements in this setup were to be collected through a frequency sweep. This set up was validated by producing a Bode plot of a single 22.5Ω resistor; this would be expected to have a uniform impedance independent of frequency, with $\left|\frac{I}{V}\right| = \frac{1}{22.5} = -27.04dB$ and a phase of 0 degrees. The Bode plot (fig. 3-19) showed that the magnitude of admittance is accurate to ±0.01dB whereas the phase was accurate to 0.61° except at 1kHz where the error was 1.32°.

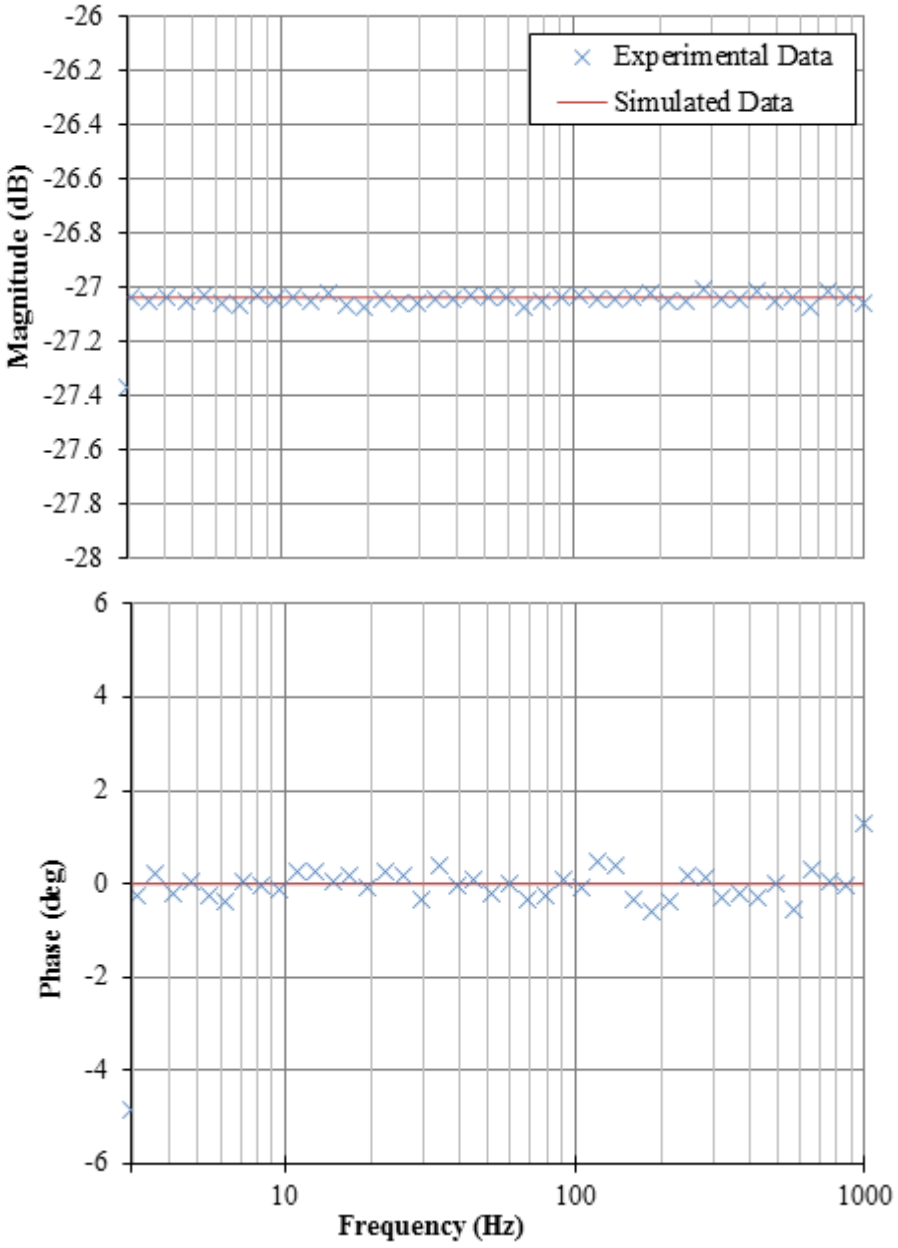

Figure 3-19. A Bode plot of a resistor connected to the low power experimental setup.

The verification of the low power experimental setup was extended with the frequency response of a coil (Fig. 3-20) in order to ensure that the system follows the typical first order LR circuit transfer function (3.49).

$$\frac{I_T(s)}{V(s)} = \frac{1}{R_1 + L_1 s} \qquad (3.49)$$

Figure 3-20 shows that the system closely follows the LR circuit model except high frequency phase lead, which was also apparent with the resistor testing. The probable cause of this were small values of V and I_T making it difficult to measure the phase accurately at higher frequencies; the results were however a good fit to the LR model especially in the most important area, around the breakpoint frequency.

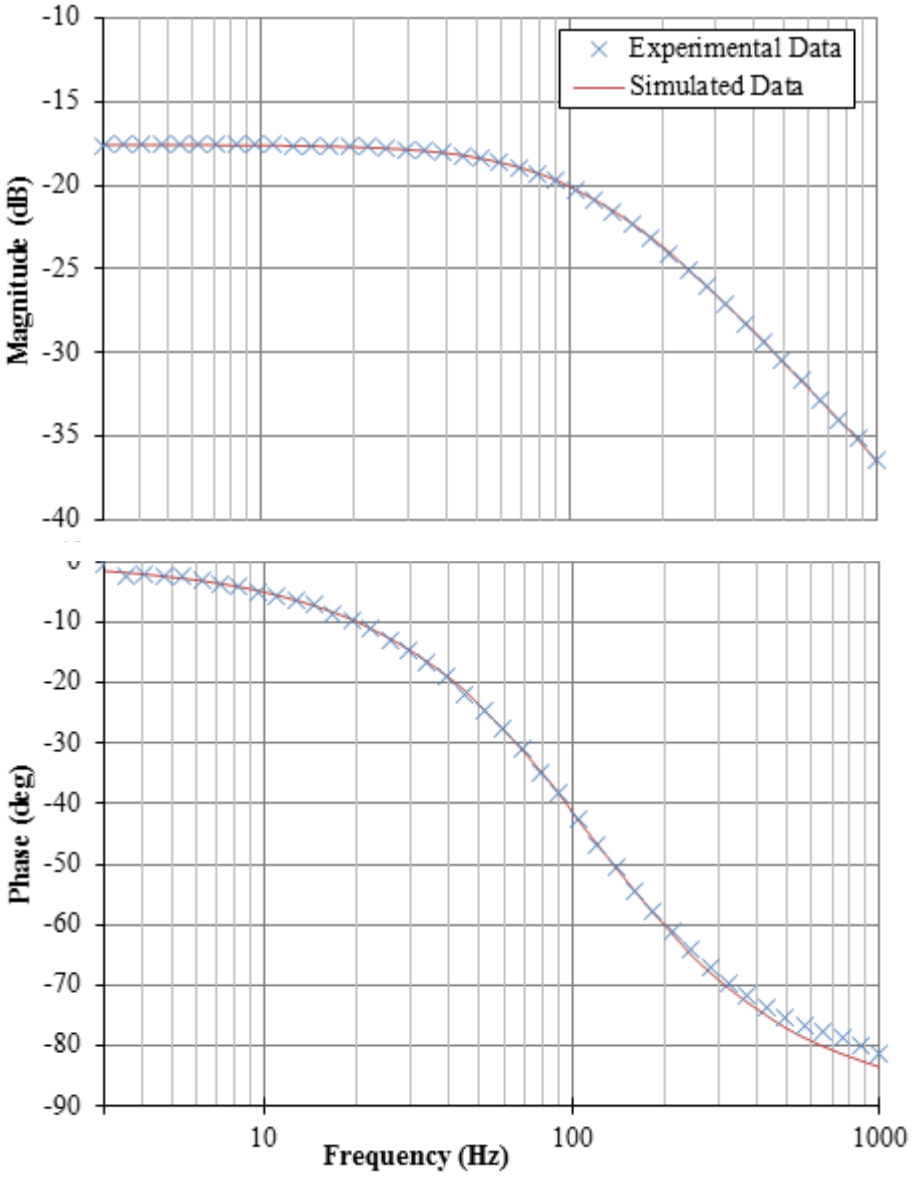

Figure 3-20. A Bode plot of a coil connected to the low power experimental setup.

3.4.2. HIGH POWER EXPERIMENTAL SETUP SIGNAL ANALYSIS

To generate a current large enough to produce a force and displacement signal with a large signal to noise ratio; a high power set up was used (as described in figure 3.7). There were five signals were to be measured in the high power experimental setup.

1. $V_{OUT}(t)$ – The demand signal
2. I(t) – The current signal
3. $V_1(t)$ – The voltage signal
4. F(t) – The force signal
5. x(t) – The displacement signal

The demand signal was a DC test signal measured by connecting the DAQ output signal directly to an oscilloscope input to ensure that the requested voltage was the voltage that was actually being applied to the amplifier. Measuring the requested demand against the actual achieved demand produced an average variation of 0.05%.

The relationship between the demand, V_{OUT} and the measured voltage V_1 were related by the amplifier response, figure 3-21. This figure shows the frequency response of the amplifier; it would be expected that the magnitude of the amplifier gain should remain constant throughout its operation whilst the phase should exhibit pure delay characteristics, due to the on-board controller processing delay with a time constant of 17.5ms. The actual frequency response however shows that, whilst the phase does exhibit pure delay characteristics, the magnitude shows a slight decline of around 0.3dB from 3Hz to 1000Hz, this correlates to a 3.5% reduction in voltage.

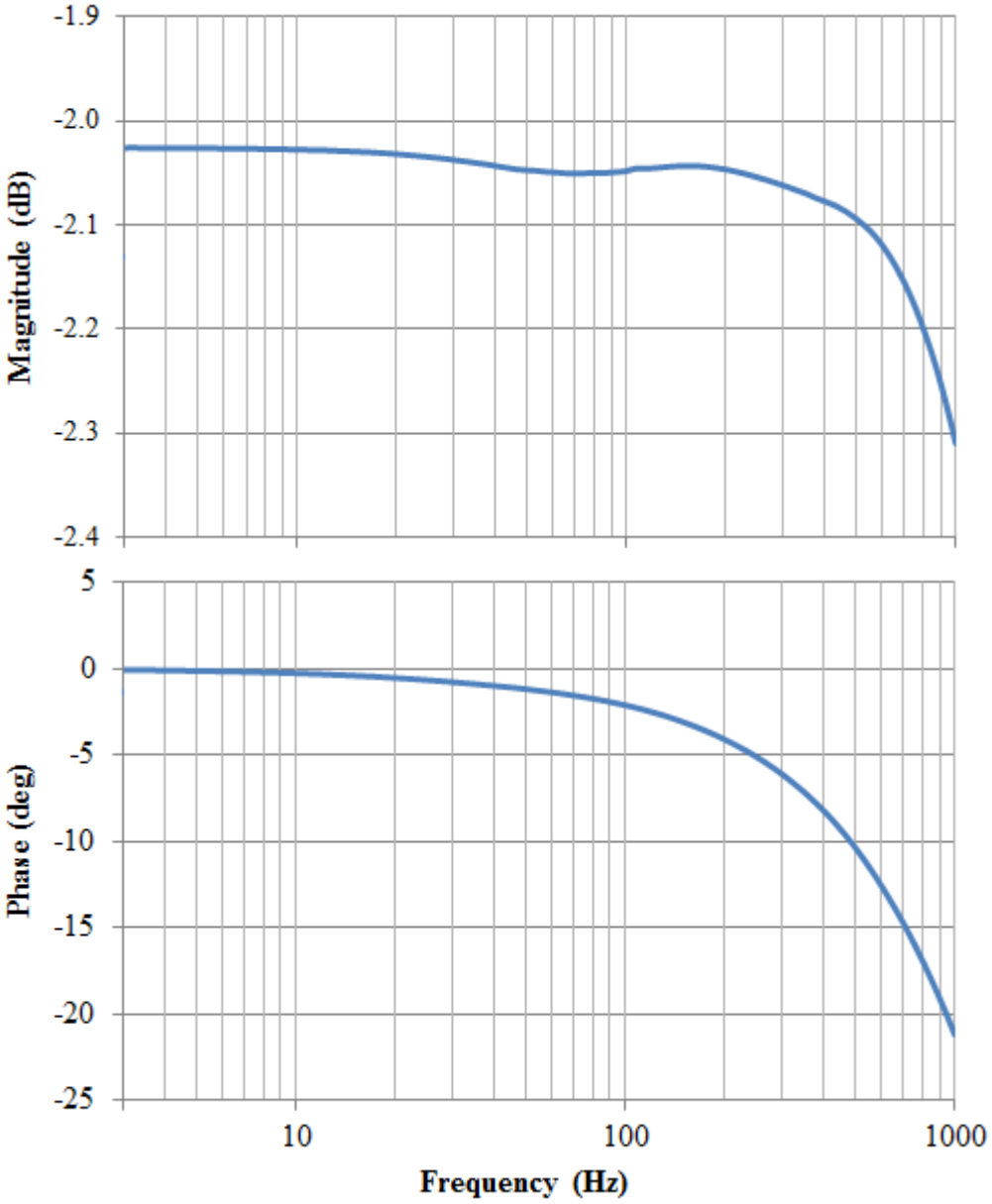

Figure 3-21. The amplifier frequency response

The current signal was verified by applying the voltage across a known resistance and ensuring the current signal obeys Ohm's Law. The current was measured using a current clip meter with a sensitivity of 100mV/A.

The force signal measured using a load cell and a strain gauge amplifier was connected as displayed in figure 3-22; whereby a DAQ powers a strain gauge amplifier which in turn delivers an excitation voltage to the load cell. The output is

the amplified by the strain gauge amplifier and interpreted by the DAQ to produce a meaningful output.

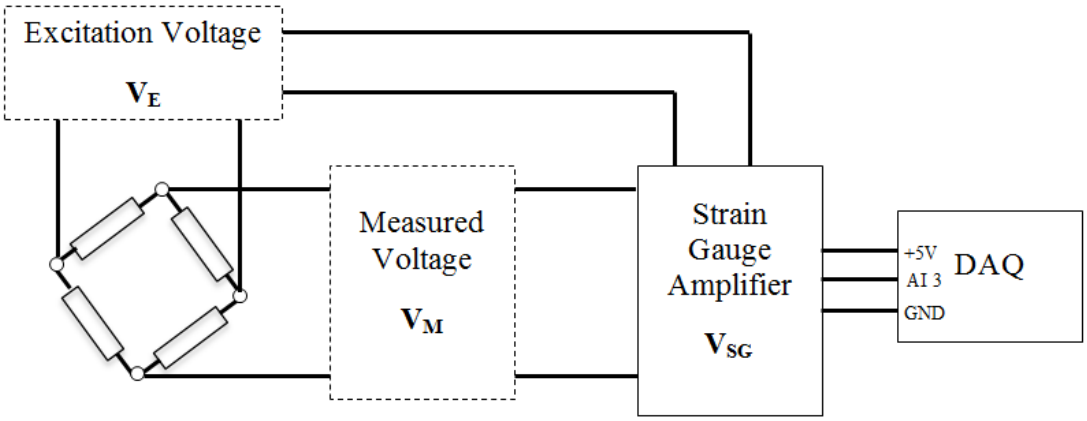

Figure 3-22. The force measurement set up.

Following computation of the strain gauge amplifier gains, a relationship between voltage measured from the strain gauge (V_{SG}) and the force output in compression was given by:

$$F_M = 39.185 V_{SG} \qquad (3.50)$$

To verify the accuracy of this calculation the load cell was calibrated using a series of masses in both tension and compression, the result of this calibration may be seen in table 3-6. This had an average variation between the known load (accurate to ±0.01N) and the calculated reading of only 0.29%.

Load (N)	Experimental Reading (N)
0.30	0.27
0.90	0.90
1.51	1.50
2.32	2.32
10.0	10.0
19.60	19.60
50.00	49.80

Table 3-6. Verification of load cell accuracy.

The current, voltage and force signals all displayed noise; quantitative analysis of this noise and distortion in the system was conducted by calculating the total harmonic distortion plus noise. The total harmonic distortion plus the noise distortion (THD+N) is a sum of all the powers of all the harmonics divided by the fundamental frequency (eq. 3.51), this produces a quantitative method of describing the distortion of a signal (Bollen & Gu, 2006) and (Kester, 2005).

$$THD + N = \frac{\sum_{n=2}^{\infty} Harmonic\ Powers_n + Noise\ Power}{Power\ of\ Fundamental\ Frequency} \quad (3.51)$$

The results of this analysis are shown in section 3.3.4

The laser sensor produced an output from -10V to +10V over the full range of 100mm; this was verified by manually measuring the displacement of the test rig shaft and mover. The displacement measurements were not filtered, as displacement experiments were conducted independently of other signals and any drop in magnitude was undesirable as measurements were conducted in the time domain.

3.4.3. SIGNAL CONDITIONING

An extensive investigation into the source of the force, current and voltage noise was conducted. This was achieved using spectral analysis whereby the signals were sampled at very high frequencies (50 MHz) under no-load conditions and then analysed to gauge the frequencies that were most significant within the noise signals. The analysis was used to decide whether to filter the signals using software or hardware filtering; software filtering is a very adaptable convenient method of filtering signals, however it is limited by the sampling rate, so therefore if there were any significantly noisy components above the DAQ's maximum sample rate for 5 signals of 50kHz analogue filtering would be required. Figures 3-23, 3-24 and 3-25 show the results of this analysis.

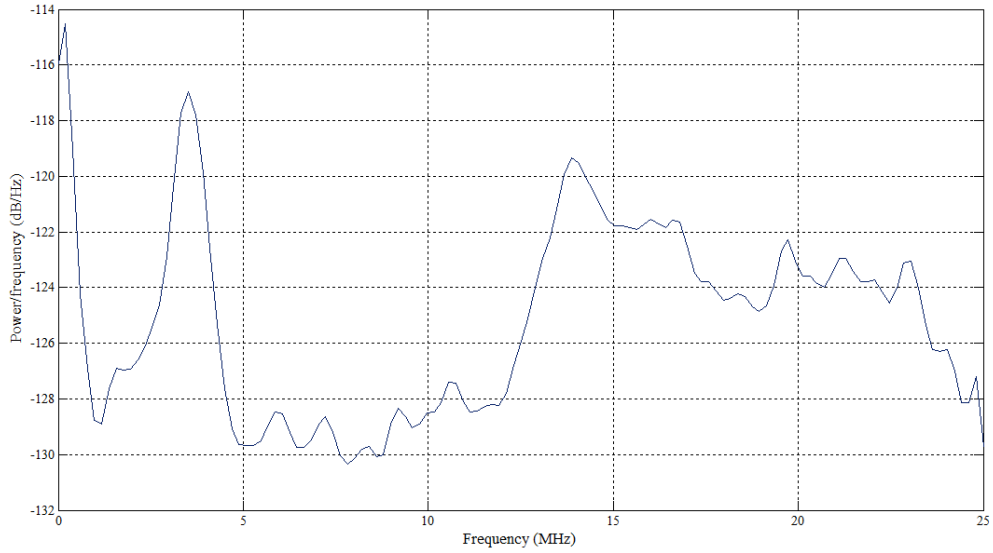

Figure 3-23. Spectral analysis of the unfiltered voltage signal.

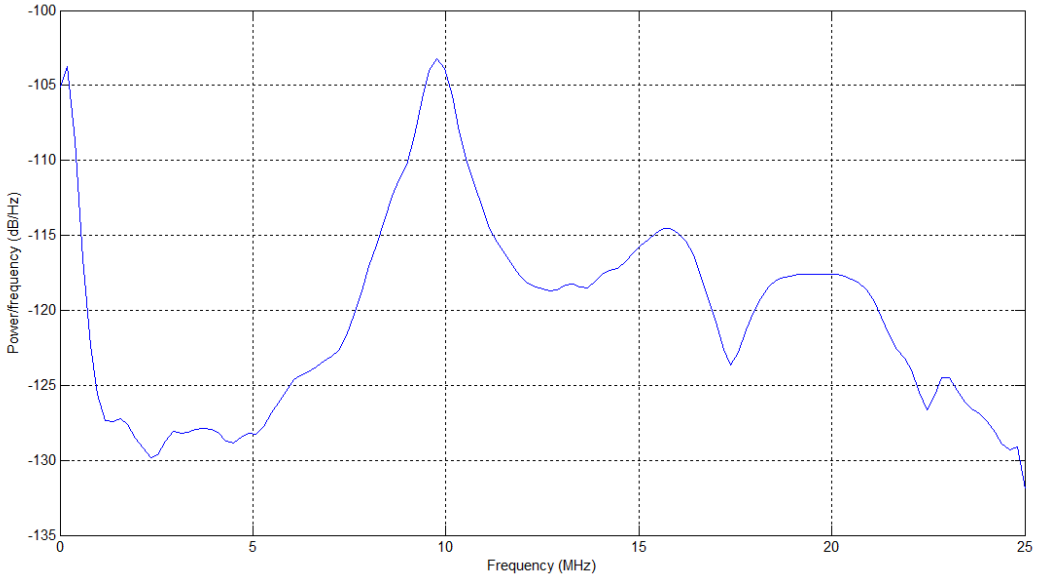

Figure 3-24. Spectral analysis of the unfiltered current signal.

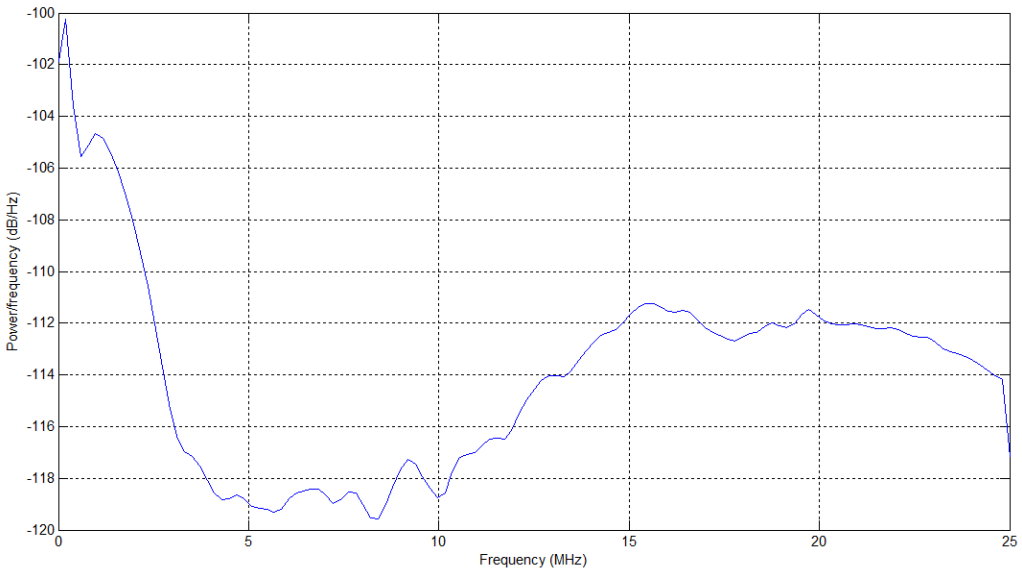

Figure 3-25. Spectral analysis of the unfiltered force signal.

Figures 3-23 to 3-25 displayed noise in excess of 1MHz with the current signal producing a noise power in excess of the fundamental frequency. Whilst the current signal showed the most prominent peak within this range, the force showed the largest sustained level of noise of around -111dB/Hz. These high levels of noise well in excess of the DAQ's maximum sample frequency of 50kHz demonstrated the necessity of using analogue filters to eliminate noise.

The results of this analysis (detailed in table 3-7), showed that 20.06% of the force signal (the most distorted signal) was noise and distortion. This was unacceptable as the fundamental frequency used was 20Hz and as the fundamental frequency becomes closer to the maximum operating frequency of 1kHz, the power of this frequency would be reduced making the signal mostly noise and distortion; therefore filtering was designed and applied.

3.4.4. FILTER DESIGN

A simple first order low pass filter was chosen to eliminate the high frequency noise detailed in section 3.4.3.

The low pass filter comprised of a RC circuit as shown in figure 3-26:

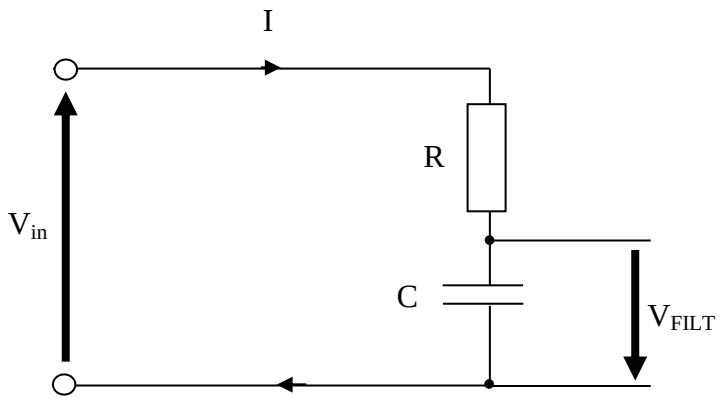

Figure 3-26. Analogue low pass filter circuit design.

Which had a cut of frequency (Ω) of:

$$\Omega = \frac{1}{RC} \tag{3.52}$$

The filter was designed so that the magnitude of admittance (Y_{COIL}) at 1000Hz was a minimum of 95% of its unfiltered value.

$$\left|\frac{V_{out}}{V_{in}}\right| = 0.95 = \frac{1}{\sqrt{\left(\frac{\omega}{\Omega}\right)^2 + 1}} \tag{3.53}$$

This gave a cut off frequency (Ω) of 3042Hz.

Using standard component values of a 1kΩ resistor and a 47nF capacitor, the filtered magnitude at 1kHz was 95.6% of the unfiltered magnitude.

Post-filtering, signals experienced significant reductions in the values of total harmonic distortion and noise (table 3-7) with the voltage, current and force experiencing drops of 16.27%, 11.49% and 51.65% respectively.

	Unfiltered THD + Noise (%)	Filtered THD + Noise (%)	Percentage Reduction (%)
Force	20.06	10.36	48.35
Voltage	1.32	0.21	84.09
Current	4.47	0.51	88.59

Table 3-7. A comparison of the reduction in distortion using total harmonic distortion plus noise analysis of the voltage, force and current signals.

The results of the THD analysis demonstrated the effectiveness of filtering. Although the force signal appears to still display a large amount of noise and distortion, by comparing a) the original unfiltered signal; and b) the filtered signal of figures 3-27 to 3-29, it becomes apparent the force signal is mostly distortion from the lightly damped flexure setup.

a)

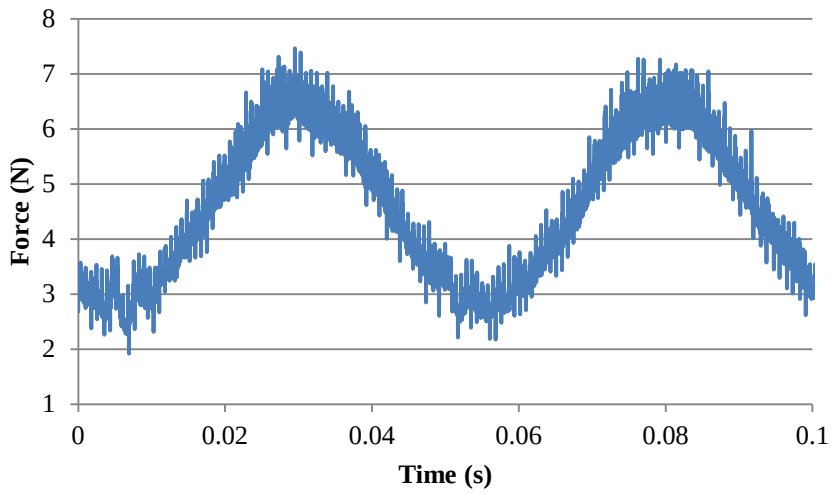

b)

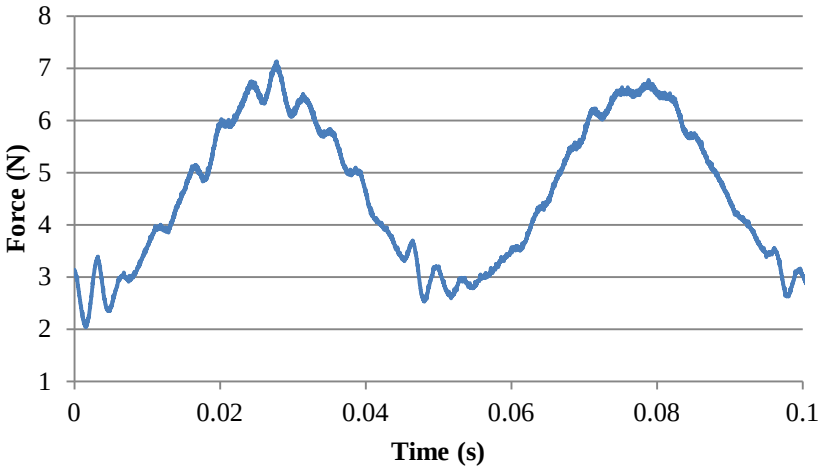

Figure 3-27. The force signal a) unfiltered b) filtered.

a)

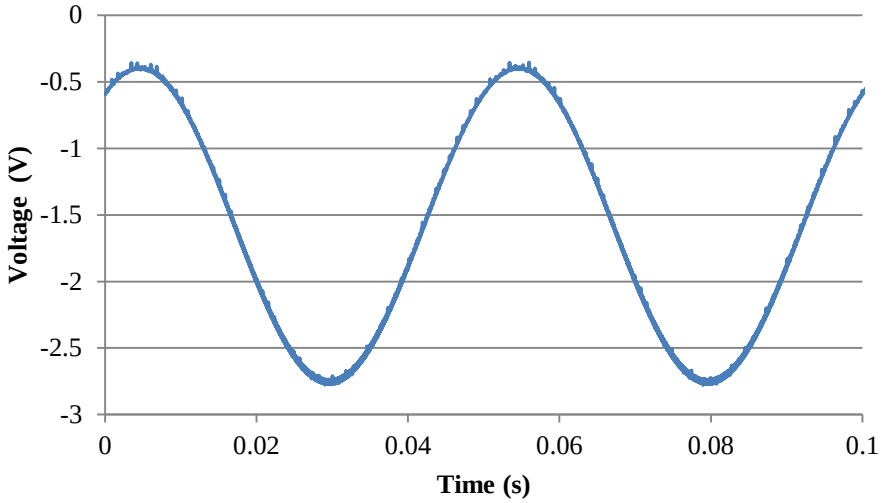

b)

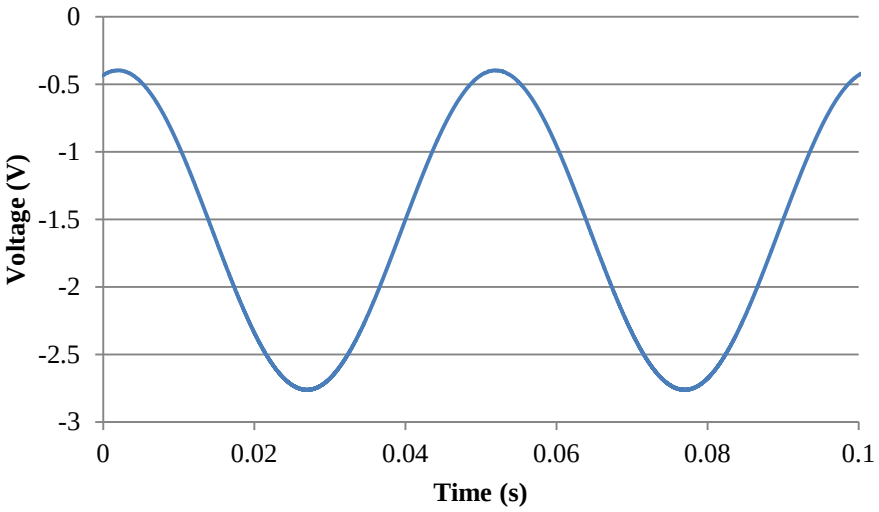

Figure 3-28. The voltage signal a) unfiltered b) filtered.

a)

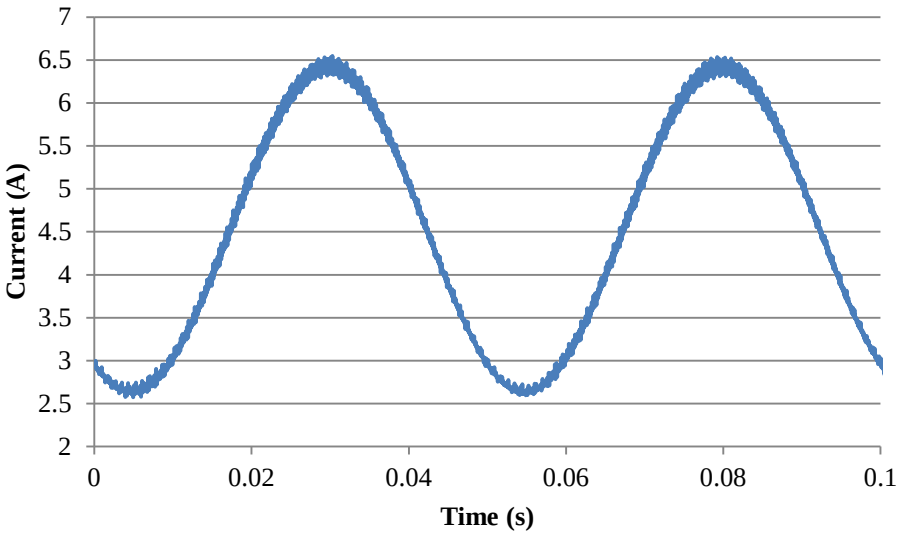

b)

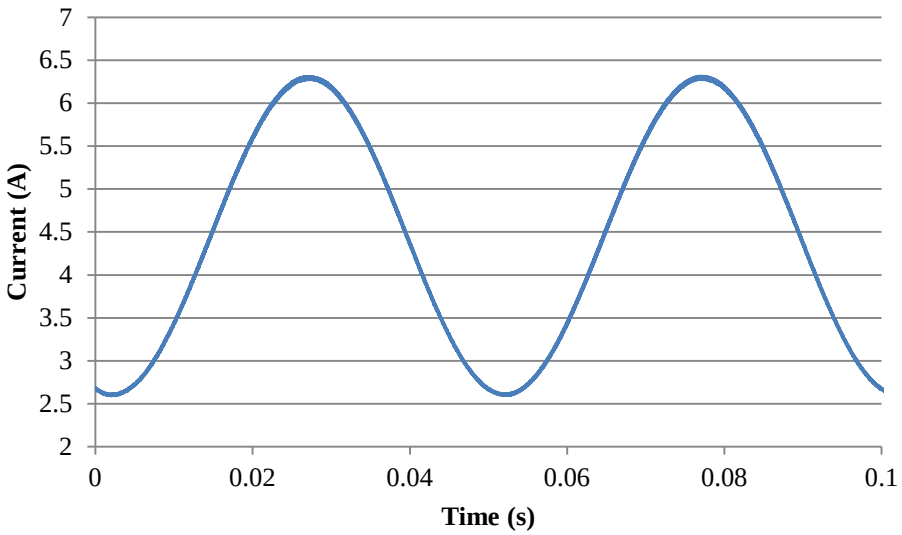

Figure 3-29. The current signal a) unfiltered b) filtered.

.

3.5. SUMMARY OF ERROR SOURCES

Within the system there are a range of effects that will affect the accuracy of any calculations and simulated results; these effects are listed below in order of importance.

- Resonant effects mean that peaks and troughs will be expected in force measurements due to the system mechanics (table 3-4).
- Noise and/or distortion, as quantified by the total harmonic distortion and noise analysis (table 3-7) will degrade the measurement resolution at high frequencies.
- The roll-off of the analogue filters will cause magnitude and phase inaccuracies that are more significant at frequencies closer to the cut-off frequency; a variation of up to 2.31% at 1000Hz is possible due to variations in component manufacture.
- The air gap between the shaft and stator vary by up to 4.84%, this would cause variation in flux density (due to flux leakage) varying the stator force.

4. Experimental Investigation

Using the experimental setup as described in Chapter 3, a series of tests were conducted to ascertain the electrical and dynamic implications of using a shorted turn with electromechanical devices. This chapter details the findings of experimentation into the effect of shorted turns on current, displacement and force characteristics of a system for improved dynamic performance and range.

4.1. CURRENT RESPONSE

The work of Chai and Lisser (Chai & Lissner, 1988) which stated that a shorted turn reduced the primary coil rise time was confirmed experimentally by figure 4-1. This improved transient response will manifest in the frequency domain as increased high frequency admittance and/or a reduced high frequency phase lag, therefore ideally any results collected in this domain would display these characteristics.

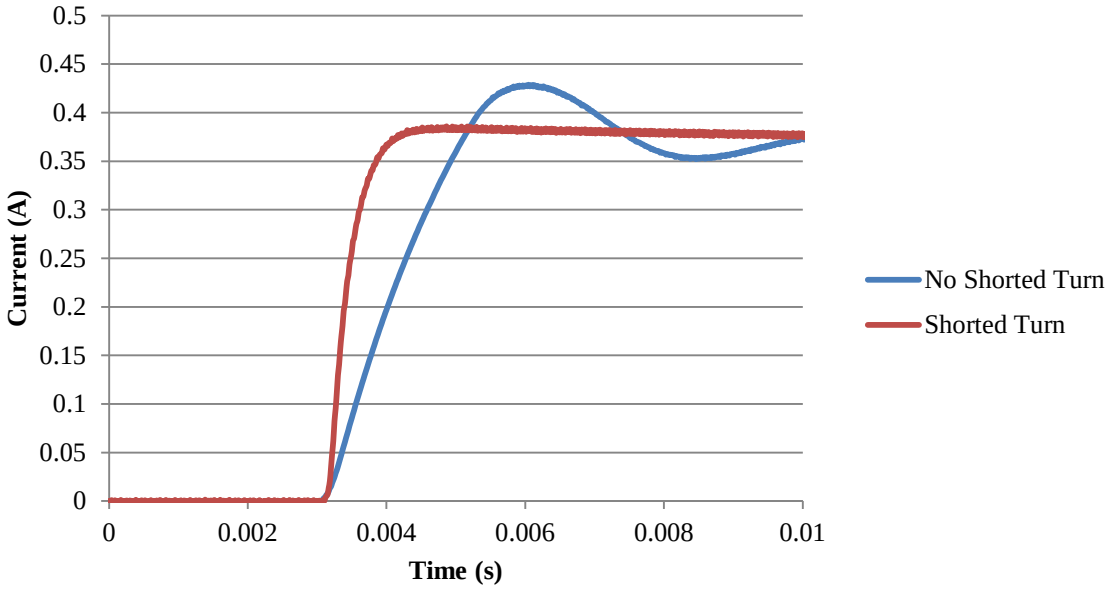

Figure 4-1. The current response to a step input of a coil with and without a shorted turn.

In order to investigate and demonstrate the effects of shorted turn parameters on this improved transient response (high frequency admittance), linear transfer models of the primary coil admittance were created.

4.1.1. LINEAR TRANSFER FUNCTION MODEL OF SHORTED TURN

In order to analyse the effects of applying a shorted turn to an on electromechanical device a relationship must be derived between the shorted turn parameters (resistance and inductance) and the electrical properties of the primary coil windings.

The basis of the shorted turn analysis is a model of a transformer based model first presented by J. A. Wagner (Wagner, 1982).

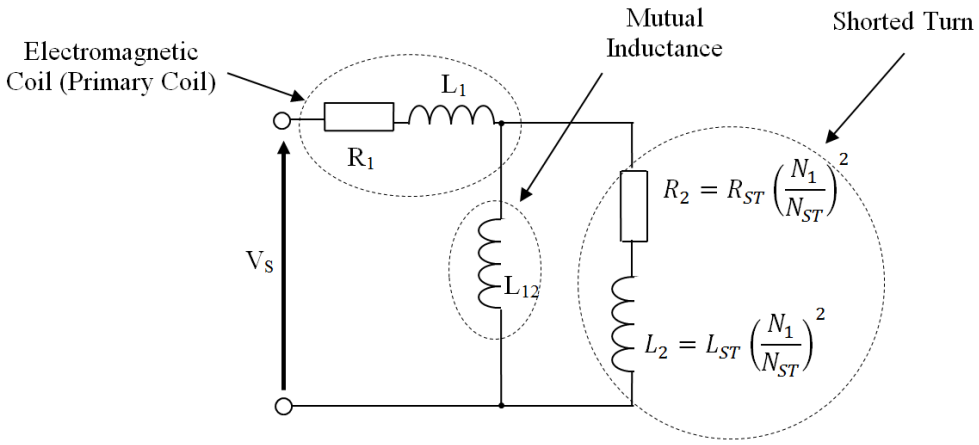

Figure 4-2. An equivalent circuit of the shorted turn transformer model.

Wagner's analysis of the equivalent circuit (Fig. 4-2) was performed solely in the time domain, detailing the effect on coil current rise time (Wagner, 1982); however within this thesis this equivalent circuit has been modelled in order to produce a transfer function relating the shorted turn resistance and inductance to coil admittance. Coil admittance (which was analysed in the frequency domain) was presented instead of impedance as it provides a more intuitive view, being proportional to the coil's current when driven under constant-amplitude voltage

conditions. The equivalent circuit relates the coil resistance and leakage inductance to the resistive and inductive properties of the shorted turn, however it is important to note that the resistance and inductance used in the model are as viewed from the primary coil, therefore the actual shorted turn resistance and leakage inductance are scaled by the turns ratio $\left(\frac{N_1}{N_{ST}}\right)^2$, where N_1 is the number of turns in the primary coil and N_{ST} is the number of turns in the shorted turn; throughout the thesis the terms apparent shorted turn resistance and inductance will be termed R_2 and L_2.

Figure 4-3 describes the shorted turn model in terms of coil impedances; the derivation of a transfer function of admittance was achieved by calculating the total system impedance and then using Ohm's Law to derive a relationship between the voltage and the total current.

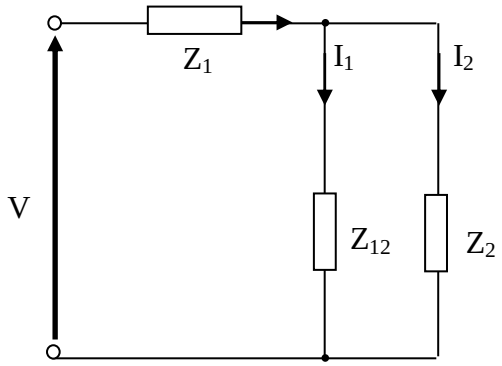

Figure 4-3. Wagner's shorted turn circuit model in terms of impedance.

Calculating the total impedance:

$$Z_{12} \parallel Z_2 = \frac{Z_{12}Z_2}{Z_{12} + Z_2} \tag{4.1}$$

$$Z_T = \frac{Z_{12}Z_2}{Z_{12} + Z_2} + Z_1 \tag{4.2}$$

$$Z_T = \frac{Z_{12}Z_2 + Z_1(Z_{12} + Z_2)}{Z_{12} + Z_2} \tag{4.3}$$

Using Ohm's Law:

$$V = I_T \left[\frac{Z_{12}Z_2 + Z_1(Z_{12} + Z_2)}{Z_{12} + Z_2}\right] \tag{4.4}$$

A transfer function of impedance was obtained by taking Laplace transforms and substituting the actual impedances $Z_1 = R_1 + L_1s$, $Z_2 = R_2 + L_2s$ and $Z_{12} = L_{12}s$:

$$\frac{V(s)}{I_T(s)} = \frac{[L_1(L_{12} + L_2) + L_{12}L_2]s^2 + [R_1(L_{12} + L_2) + R_2(L_{12} + L_1)]s + R_1R_2}{(L_{12} + L_2)s + R_2} \tag{4.5}$$

This relationship can also be expressed as admittance, as described, this will be used:

$$\frac{I_T(s)}{V(s)} = \frac{(L_{12} + L_2)s + R_2}{[L_1(L_{12} + L_2) + L_{12}L_2]s^2 + [R_1(L_{12} + L_2) + R_2(L_{12} + L_1)]s + R_1R_2} \tag{4.6}$$

Equation 4.6 is a transfer function of coil admittance including the effect of the shorted turn; this transfer function will be the basis for analysing the current response of the shorted turn.

In order to investigate and demonstrate the effects of shorted turn parameters on this improved transient response (high frequency admittance), linear transfer function models of the circuits' admittance were initially considered. Without a shorted-turn effect, the coil has a transfer function as follows:

In order to investigate and demonstrate the effects of shorted turn parameters, linear transfer function models of the circuits' admittance were initially considered. Without a shorted-turn effect, the coil has a transfer function as follows:

$$\frac{I_T(s)}{V(s)} = \frac{1}{R_1 + L_1s} \tag{4.7}$$

Based on analysis of the shorted-turn circuit analysis, the transfer function for a coil with a shorted turn becomes as follows:

$$\frac{I_T(s)}{V(s)} = \frac{(L_2 + L_{12})s + R_2}{(L_1L_2 + L_{12}L_1 + L_{12}L_2)s^2 + [R_1(L_2 + L_{12}) + R_2(L_1 + L_{12})]s + R_1R_2} \quad (4.8)$$

Figure 4-4 shows the verification of equation 4.8 with experimental results of a frequency response of coil admittance, compared to a first-order transfer function coil model. Measurements were considered valid through the range of experimental frequencies, the highest of which had a discrepancy to the linear model of less than 1%. As shown by figure 4-4, the shorted turn increases the high frequency coil admittance and reduces the high frequency phase lag; the degree of this admittance increase and reduction phase lag will be referred to as the magnitude of the shorted turn effect. Values of (R_{ST} = 0.275mΩ and L_{ST} = 0.1μH) were used for the shorted turn resistance and inductance in the admittance transfer function, throughout this thesis these values will be used to demonstrate the design principles as typical values of shorted turn resistance and inductance.

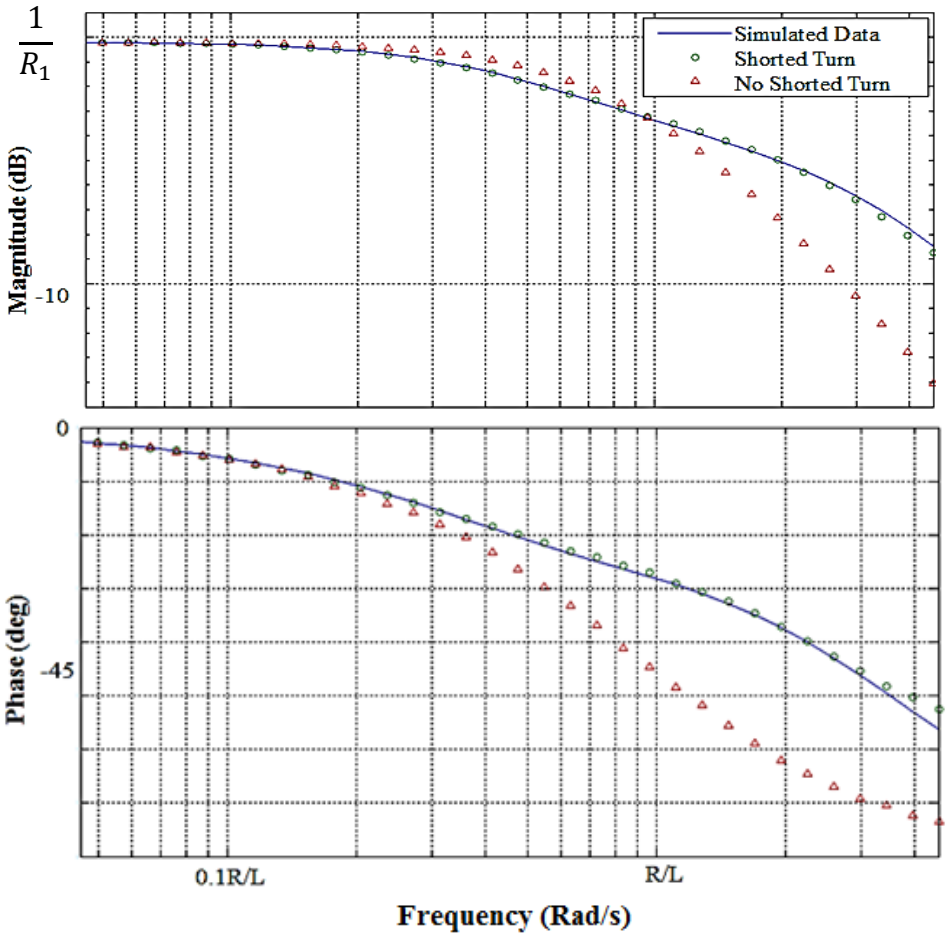

Figure 4-4. Frequency response of admittance (Y_{COIL}) of a coil with a shorted turn: experimental results and linear transfer function model.

Following the comparison of the two transfer functions (equations 4.7 and 4.8) it may be seen that a shorted turn adds one extra pole with break frequencies at:

$$f_{p1,}\ f_{p2,} = \left(\frac{1}{2\pi}\right)\frac{-b \pm \sqrt{b^2 - 4ac}}{2a} \tag{4.9}$$

Where f_{p1} and f_{p2} are in Hz; from (4.9):

$$\mathrm{a} = L_1L_2 + L_{12}L_1 + L_{12}L_2 \tag{4.10}$$

$$\mathrm{b} = R_1(L_2 + L_{12}) + R_2(L_1 + L_{12}) \tag{4.11}$$

$$\mathrm{c} = R_1R_2 \tag{4.12}$$

And a zero with a break frequency at:

$$f_z = -\frac{\mathrm{R}_2}{(\mathrm{L}_2 + \mathrm{L}_{12})} \tag{4.13}$$

All poles and zeros were negative and real signifying a stable system response.

Considering the response from low- to high-frequency, from a DC resistance of $\frac{1}{R_{DC}}$; the first pole (f_{p1}) manifests as the frequency above which the magnitude of admittance begins to decay. The presence of the opposing zero, at (f_z), mitigates this initial decrease and is responsible for the increased admittance at frequencies above the breakpoint frequency of the coil. The second pole, at (f_{p2}), then causes the decreasing admittance and 90° phase lag observed at higher frequencies. The frequency responses of the individual pole-zero components are shown in figure 4-3.

4.1.2. PARAMETRIC SHORTED TURN DESIGN

Splitting the frequency response of $\mathrm{Y_{COIL}}$ into pole/zero components (fig. 4-5); analysis into the effects of varying isolated properties of a shorted turn ($\mathrm{R_{ST}}$ and $\mathrm{L_{ST}}$) may be conducted and utilised to produce design guidelines regarding the selection

of such shorted turn properties. Although complete isolation of R_{ST} and L_{ST} without affecting L_{12} (the mutual inductance) is unlikely in practice, the results of such analysis may aid in selecting the most suitable shorted turn configuration, detailed in section 4.1.1, for a given application.

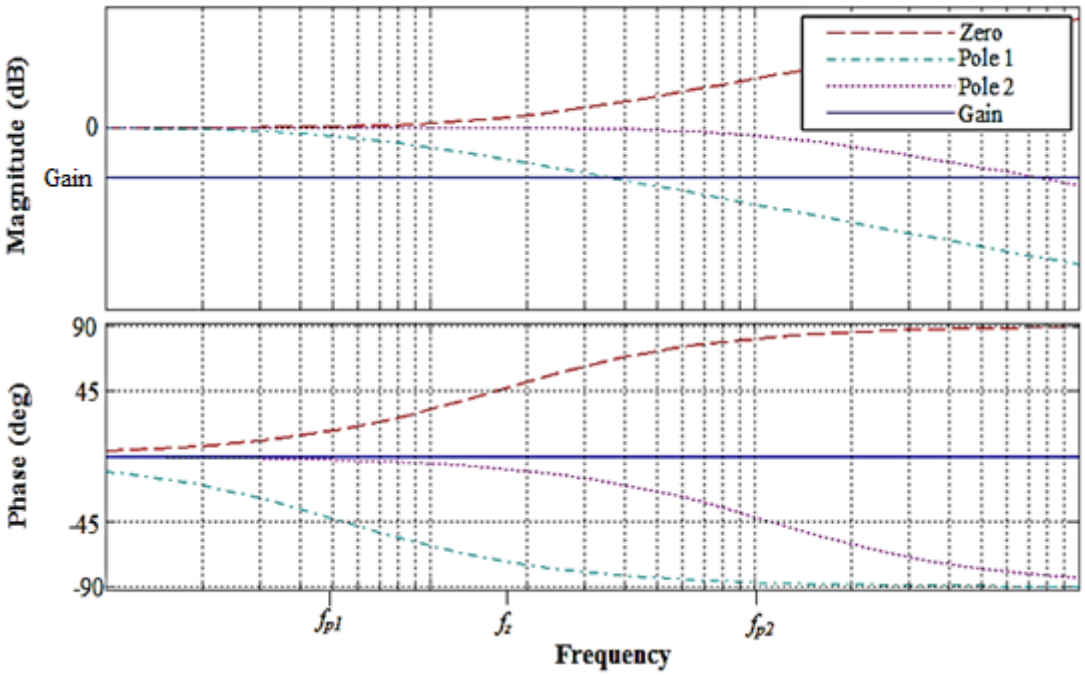

Figure 4-5. Frequency responses of component parts (poles, zero) of the shorted-turn circuit model.

Analysing figure 4-5 reveals that the lower-frequency pole (f_{p1}) produces the initial decrease in primary coil admittance, which is offset by the higher frequency zero (f_z). In order to minimise this initial admittance drop, and minimise the phase lag, the shorted-turn should be designed so that the zero is as close as possible to f_{p1} on the frequency scale (f_{p1} is necessarily lower than f_z).

Equations 4.10 to 4.12 illustrate that when b is of a large magnitude, f_{p1} and f_{p2} will have a higher breakpoint frequency. And when c is of a large magnitude, f_{p1} will have a larger frequency difference between the two poles (fig. 4-5). This is due to the small magnitude of inductance in comparison to resistance. Therefore a reduced shorted turn resistance (R_{ST}) will produce a lower break frequency for f_{p2}, and hence a lower frequency increase in coil admittance around the primary coil's breakpoint frequency (assuming constant values for the inductances of the coil and shorted turn and their mutual inductance).

A larger R_{ST} will increase the range of frequencies between f_{p1} and f_z, shift the frequency of the increase in coil admittance to a higher frequency (in excess of the primary coil breakpoint frequency). This large R_{ST} also has the effect of moving the phase lag reduction to a higher set of frequencies significantly reducing the high frequency lag. Dependent on the nature of the application this may be desirable; for example systems with a phase of -180 degrees at higher frequencies would benefit from high frequency phase lag reduction, as this would translate to improved stability margins.

Figure 4-6 illustrates how a parametric plot may be used to identify optimal values for shorted-turn design. In this example, typical values for a small coil are used (as detailed in section 4.2.1):

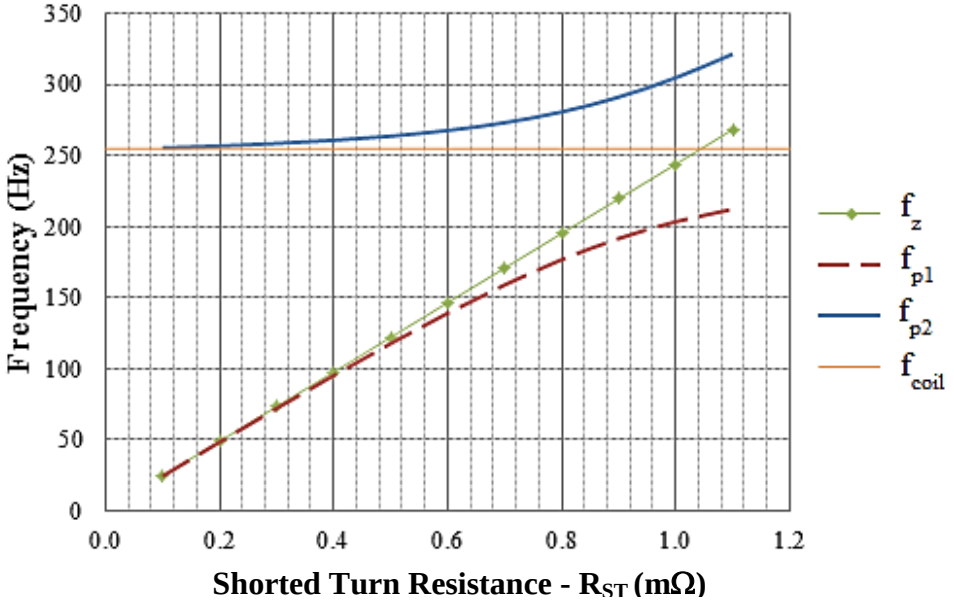

Figure 4-6. Effect of shorted turn resistance on breakpoint frequencies of poles and zeros (of primary coil transfer function model).

The optimal resistance will vary, based on the shorted turn's application: For a higher frequency reduction of phase lag (often this is optimal as the phase lag increases to 90 degrees at higher frequencies), the largest f_{p1} should be selected; on figure 4-6 this refers to the largest shorted turn resistance (1.1mΩ). For an increase in magnitude of admittance close to the primary coil breakpoint frequency, the resistance (R_{ST}) with the smallest difference between f_{p1} and f_z should be selected, lower resistances; on figure 4-6 this refers to the lowest resistance (0.1mΩ).

Figure 4-7 further demonstrates the effects of shorted-turn inductance: Higher shorted turn inductances (L_{ST}) produce a similar effect to low shorted turn resistances, with the smallest difference between f_{p1} and f_z and therefore the greatest magnitude of coil admittance at high frequencies. Lower shorted turn inductances (L_{ST}) have the effect of producing the greatest high frequency phase lag reduction. As with the resistance based parametric analysis whether an increased shorted turn range or larger admittance at high frequencies would be more desirable, is application dependent.

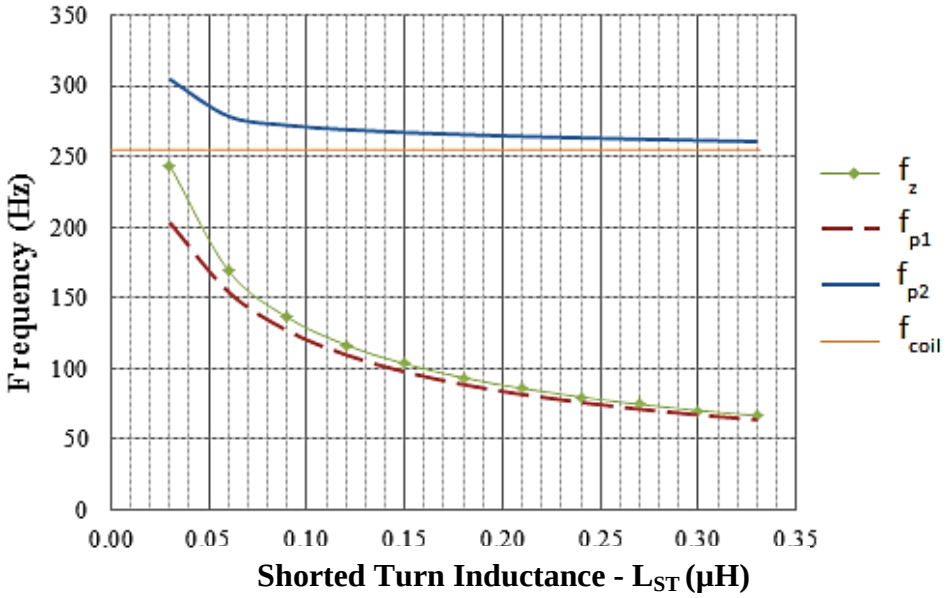

Figure 4-7. Effect of shorted turn inductance on breakpoint frequencies of poles and zero.

4.1.3. CURRENT RESPONSE EXPERIMENTAL RESULTS

The electrical impedance of an electromagnetic coil at high frequencies (above the coil's breakpoint frequency) will increase in magnitude proportionally to the frequency of AC current. When using a limited-voltage supply, this increasing impedance reduces the current through the coil and therefore also reduces the magnetic field strength. In many electromagnetic applications, this high-frequency effect restricts the dynamic performance e.g. read/write head acceleration within a hard disk drive or linear actuator. The impedance also causes a phase lag between

the coil voltage and current at high frequencies. These effects cause reductions in stability margins in closed-loop control situations; therefore the ability to modify impedance above a coil's natural breakpoint frequency has the potential to offer great advantages in controllability and performance of electromechanical systems.

This section details the results of experimentation into the effect of a shorted turn on the current response (e.g. current magnitude and phase). Design guidelines are developed with the aim of improving the potential frequency response of the coil current, which could offer performance improvements to many electromechanical devices. As discussed in section 3.1 testing was performed on a low power set up to avoid any effects such as saturation, or the production of back emf due to the movement of the mover over the coil.

Following the parametric analysis, design guidelines for a shorted turn have been set out in terms of shorted turn resistance (R_{ST}) and shorted turn inductance (L_{ST}). As in reality perfect isolation of these parameters from each other is unlikely; experimentation was therefore conducted, not only to ascertain the accuracy of hypothesis derived from parametric analysis but also how these hypotheses translate to the physical attributes of a shorted turn.

4.1.4. CURRENT RESPONSE EXPERIMENTAL SETUP

A range of removable aluminium cylinders (shorted turns), which fitted closely around the primary coil (with the aim of achieving close inductive coupling), were designed to investigate the effect of shorted turn properties on coil admittance. A series of experiments were designed to gain insight into how a shorted turn would behave within real world applications and derive relationships between the shorted turn's inductive and resistive properties and the primary coil's current response.

Each experiment was designed to examine one property of a shorted turn (although complete isolation of resistance and inductance was unlikely to be feasible) these experiments are detailed below.

Experiment A: Vary the air gap between the coil and the shorted turn (with the cylinder wall thickness kept constant) to investigate the effects of a change in mutual inductance (L_{12}). From preliminarily experimentation it is hypothesised that the smallest air gap between the coil and the shorted turn would produce the most significant shorted turn effects (fig. 4-8).

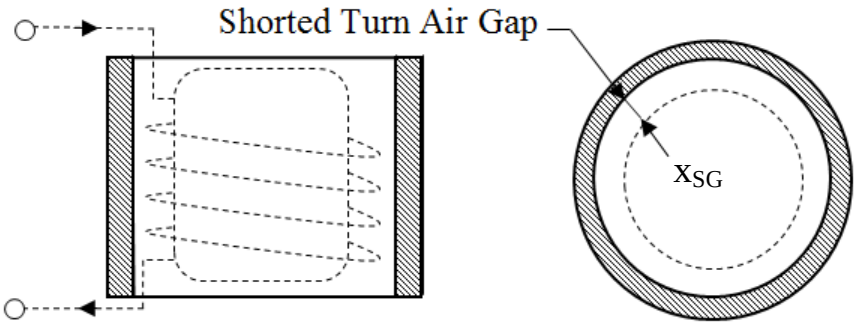

Figure 4-8. Experiment A; an investigation into the effect of the air gap between the shorted turn and coil on the primary coil (x_{SG}) current response.

Experiment B: Vary the height of the shorted turn in relation to the coil (e.g. 100% height is equal to the coil height), although this will investigate the effect of varying two parameters, shorted turn resistance (R_{ST}) and the closeness of coupling (L_{12}), this was still explored as from a design perspective it would be a very practical method of "tuning" the shorted turn effect. It was hypothesised that the shorted turn with the smallest height covering the stator would produce the least significant shorted turn effects, due to an increased flux leakage and resistance (fig. 4-9).

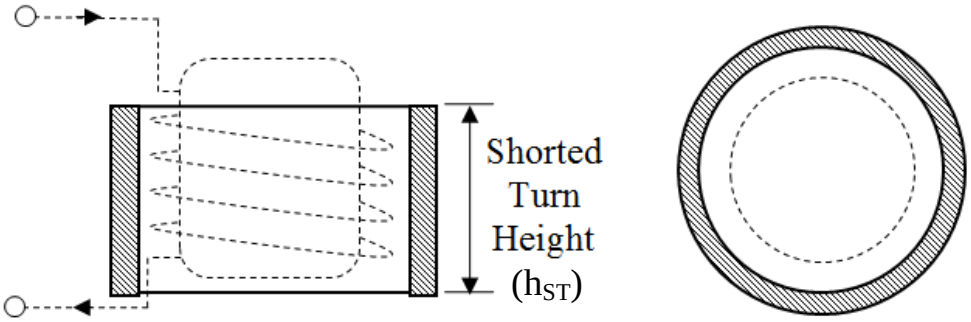

Figure 4-9. Experiment B; an investigation into the effect of shorted turn height on the primary coil current response.

Experiment C: Vary the proportion of the shorted turn covering the coil by moving a full height shorted turn (the same height as the coil) so that it was only partially covering the coil; this was to investigate the effect of a change in mutual inductance (L_{12}) due to an increased flux leakage, whilst keeping the resistance constant. It was hypothesised that the shorted turn covering the biggest proportion of the coil would produce the most significant shorted turn effects (fig. 4-10).

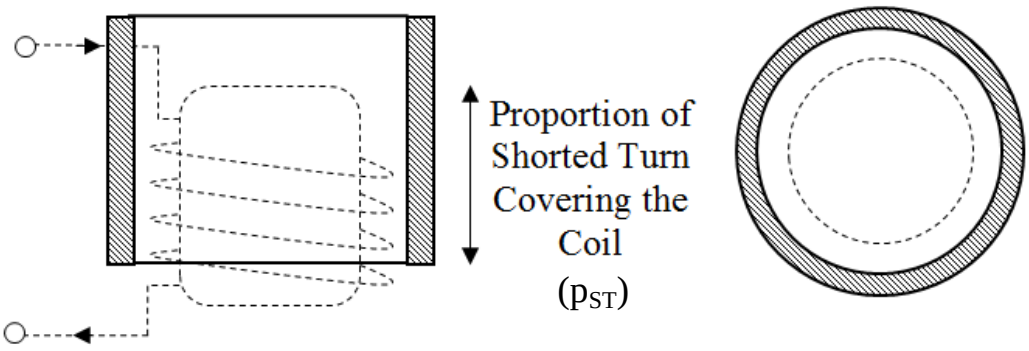

Figure 4-10. Experiment C; an investigation into the effect of the proportion of shorted turn covering the coil (p_{ST}) on the primary coil current response.

Experiment D: Vary the wall thickness of a close fitting shorted turn to investigate the effects of reducing the shorted turn resistance (R_{ST}) due to an increase in the cross sectional area. Based on the work of Stamp and Hanson (Stamp & Hanson, 2011) and linear transfer function analysis (section 4.1) it was hypothesised that the thicker lower resistance shorted turns would produce a greater coil admittance at high frequencies, whilst the thinner higher resistance shorted turns would produce a greater shorted turn range. It was also hypothesised that due to the skin thickness of aluminium any increases would reduce after a wall thickness of 2.68mm (fig. 4-11).

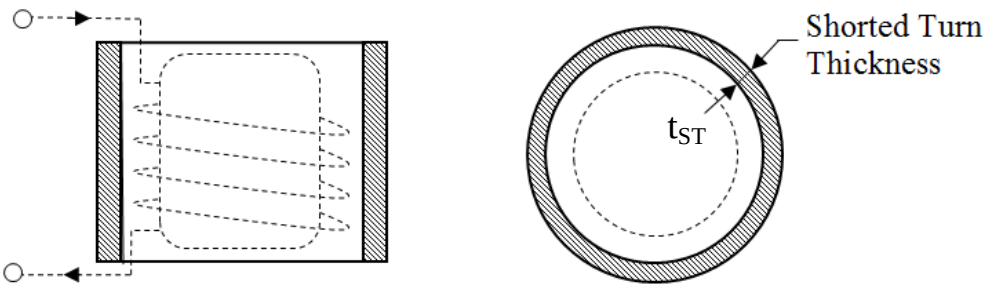

Figure 4-11. Experiment D; an investigation into the effect of shorted turn thickness (t_{ST}) on the primary coil current response.

Experiment E: Using a shorted turn with a complete slit across the cylinder wall and applying a variable resistance across the break in the circuit, via connection of various gauge wire in order to, based on Moser's work (Moser, 1996), investigate the feasibility of controlling the shorted turn effect by connecting electrical components in series to the shorted turn (fig. 4-12).

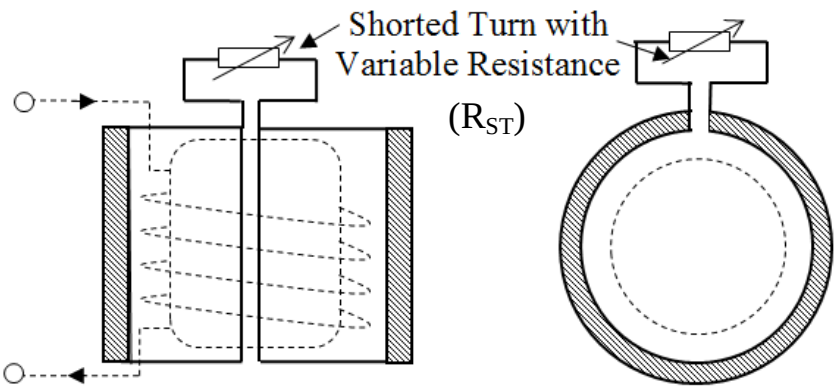

Figure 4-12. Experiment E; an investigation into the effect of shorted turn resistance (R_{ST}) on the primary coil current response.

Experiment F: Wrapping a secondary coil around the primary coil with its ends connected in a "shorted" manner, termed an "S-Coil", and was investigated using different gauges of wire to assess the effect of N_{ST} on the shorted turn effect. Adding more turns would increase the actual and apparent shorted turn (S-Coil) inductance (L_{ST}) and reduce the apparent coil resistance (R_2) even though the shorted turn resistance (R_{ST}) would increase. This is as although the doubling the number turns (assuming the length doubles) will double the shorted turn resistance, the apparent resistance (R_2) will actually half due to the turns ratio (eq. 3.53):

$$R_2 = R_{ST}\left(\frac{N_1}{N_{ST}}\right) \qquad (3.54)$$

A switch was also investigated in the experimentation to evaluate the possibility of using electrical components, such as relay switches, in series with a shorted turn to "switch" the shorted turn effect on and off (fig. 4-13).

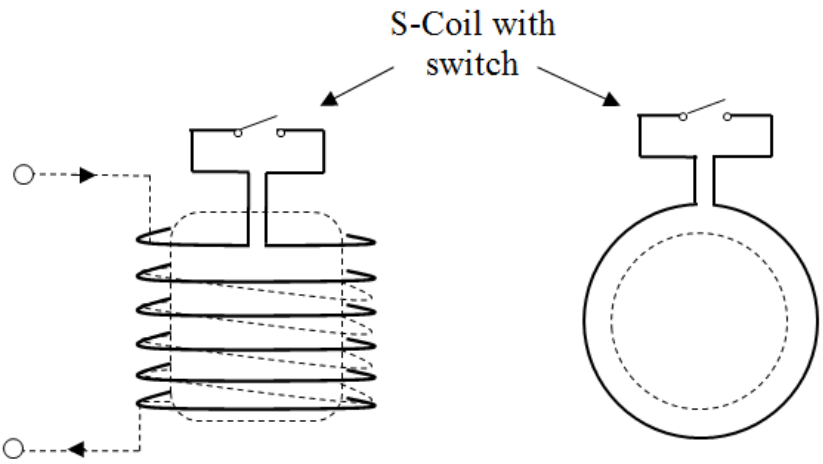

Figure 4-13. Experiment F; an investigation into the effect of using an S-Coil instead of a shorted turn on the primary coil current response.

4.1.5. CURRENT RESPONSE EXPERIMENTAL RESULTS

Experiments A, B and C all investigated the hypothesis that increasing the physical separation of the shorted turn to the primary coil (by either increasing the air gap between the coil and the shorted turn, decreasing the height of the shorted turn or reducing the coil coverage of the shorted turn) would in turn decrease the magnitude of the shorted turn effect (reduced phase lag and increased admittance at high frequencies) due to a reduction in the mutual inductance (L_{12}). Figures 4-14, 4-15 and 4-16 show that the experimental results match this hypothesis, as an increase in the physical separation of the shorted turn from the primary coil corresponds to a reduction in the magnitude of the shorted turn effect. This is shown by a larger magnitude of admittance and reduced phase lag at high frequencies; there are however a range of frequencies (around the breakpoint frequency) whereby the magnitude of admittance drops relative to a coil alone. This was expected as the pole f_{p1} always occurs before the zero f_z.

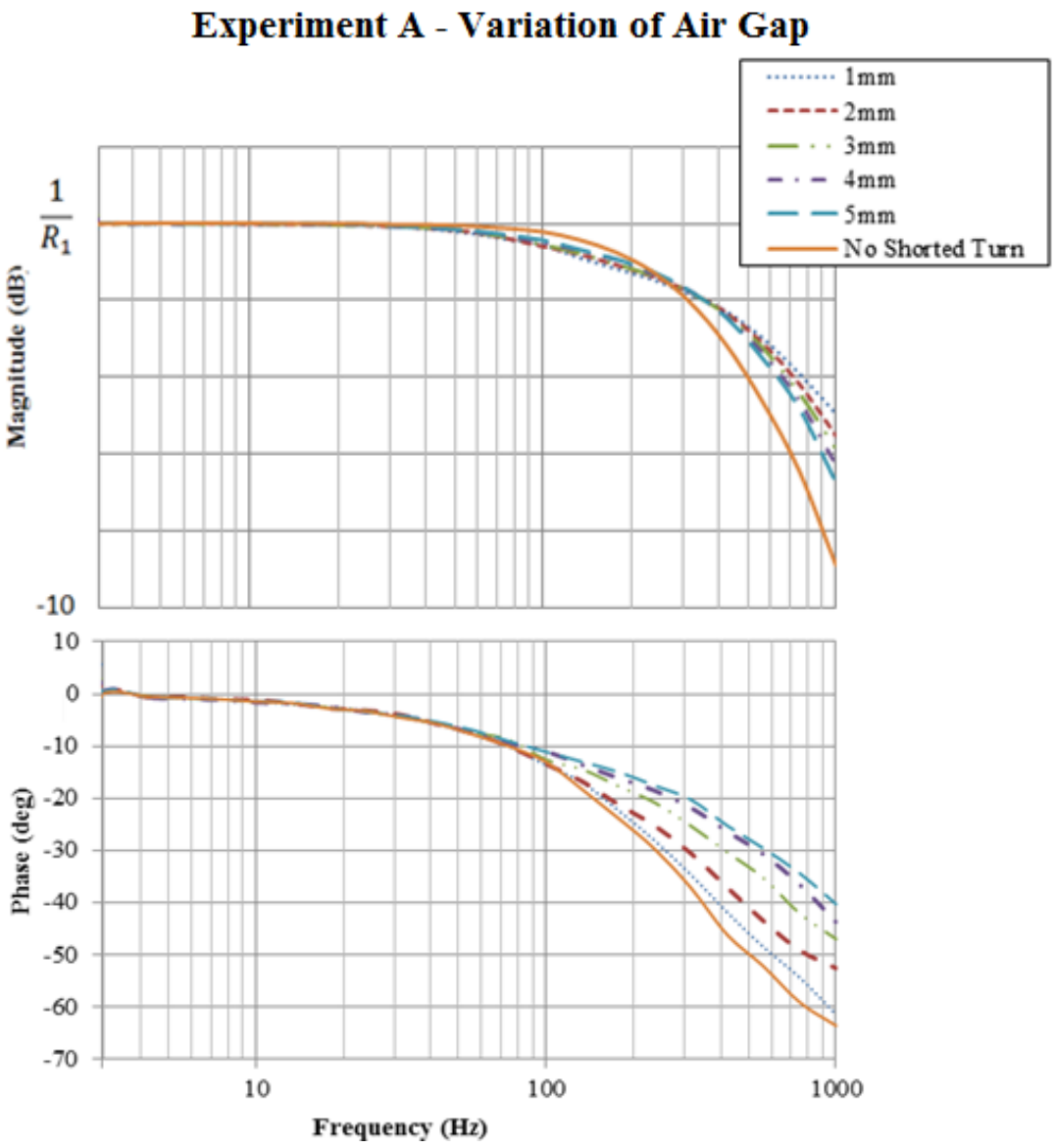

Figure 4-14. Experiment A (fig. 4-8): A Bode plot of Y_{COIL}, varying air gap between the primary coil and shorted turn.

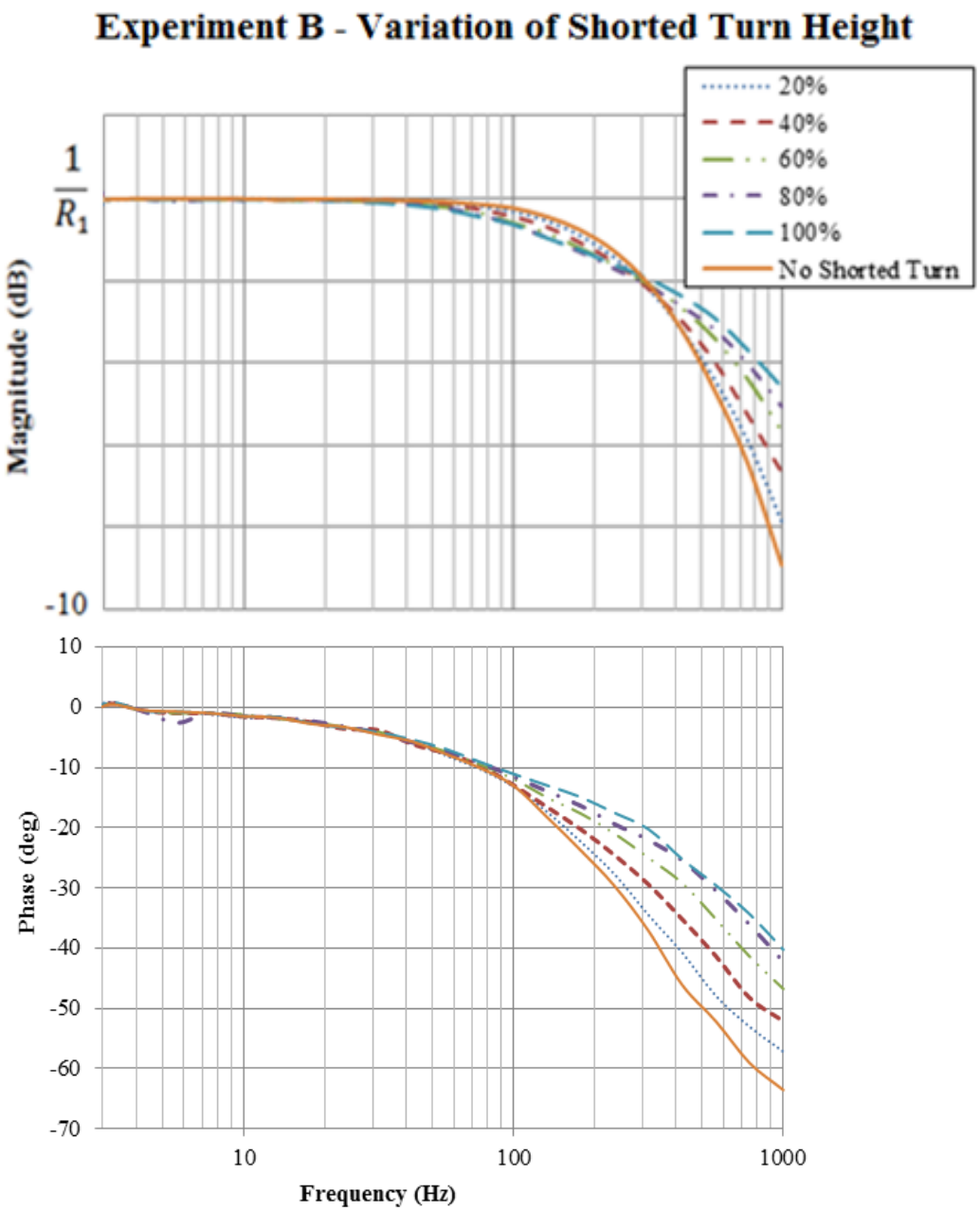

Figure 4-15. Experiment B (fig. 4-9): A Bode plot of Y_{COIL}, varying the height of a close-fitting shorted turn covering a primary coil.

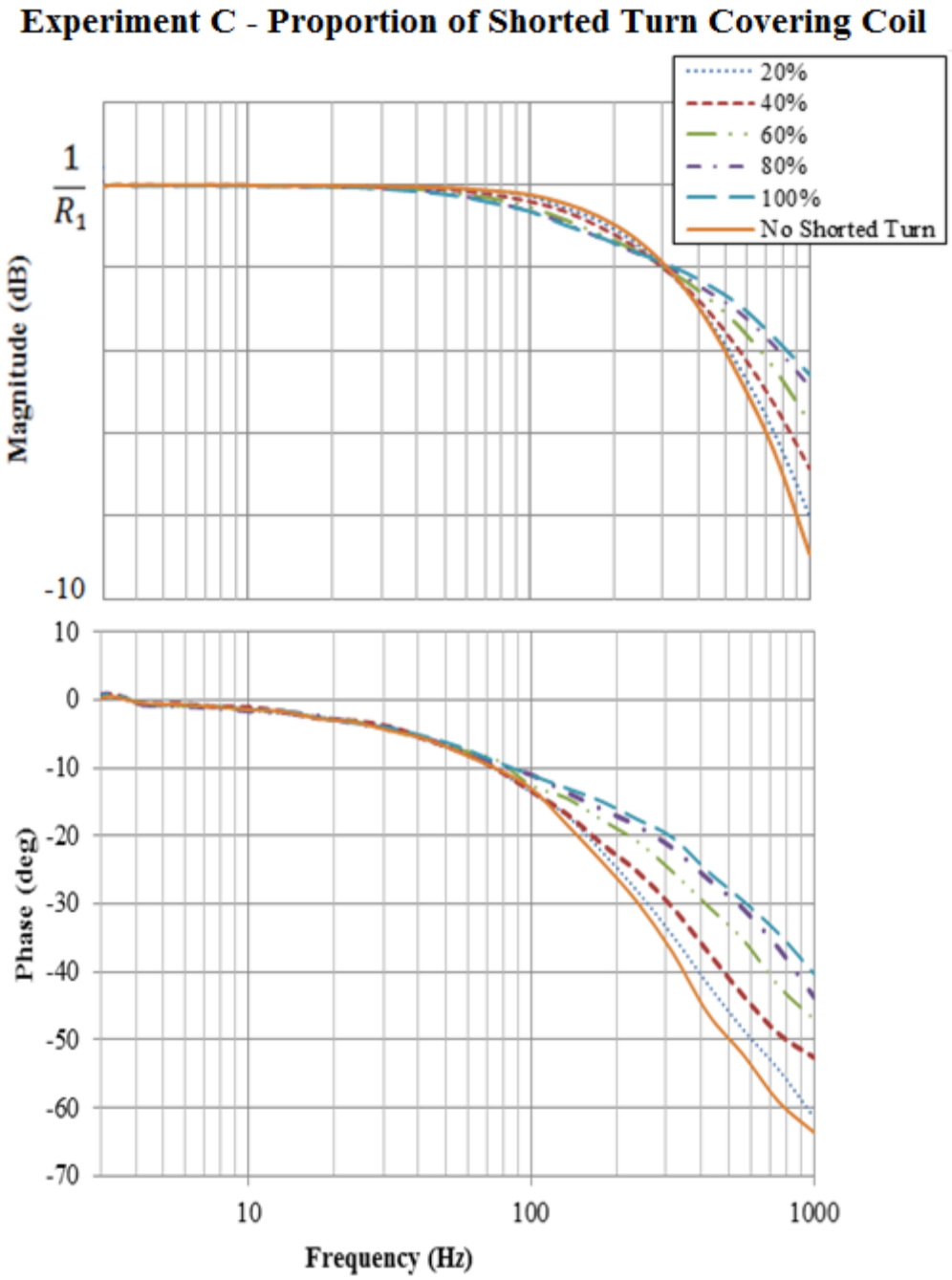

Figure 4-16. Experiment C (fig. 4-10): A Bode plot of Y_{COIL}, varying the proportion of a shorted turn covering a primary coil.

The magnitude of the shorted turn effect in figures 4-14, 4-15 and 4-16 were quantified based on a cost function (appendix 1), this cost function (also used to optimise the shorted turn parameters R_{ST} and L_{ST} to experimental data of a frequency sweep of Y_{COIL}) calculated the sum squared difference to quantify the reduction of the shorted turn effect in relation to a full height 5mm thick shorted turn, with no air

gap and full coverage (the shorted turn that produced the most significant effect). Plotting the results of this quantitative analysis demonstrated that the shorted turn has a linear relationship to the size of the air gap (fig. 4-17), whilst quadratic functions were fitted to the other methods of varying the physical closeness (figs. 4-18 and 4-19).

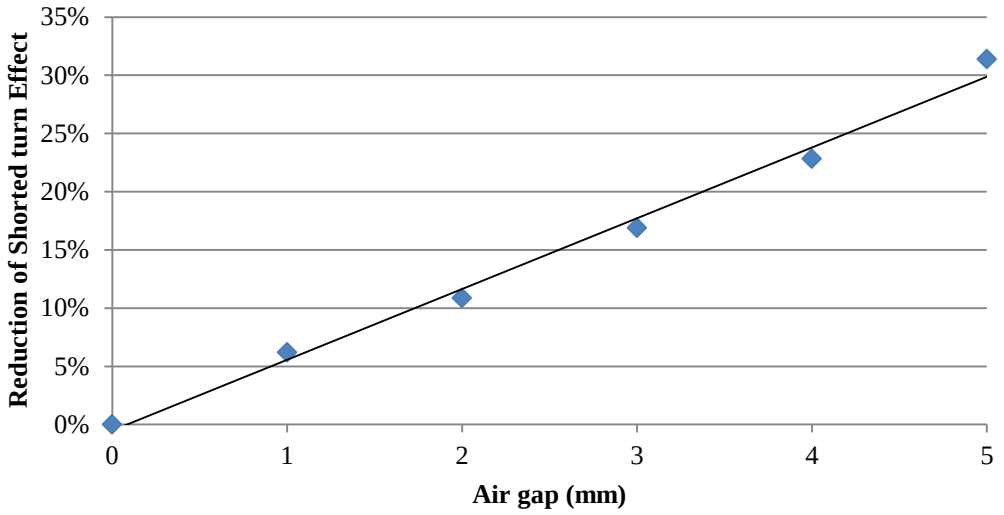

Figure 4-17. The reduction of shorted turn effect based upon a change in air gap between the primary coil and shorted turn.

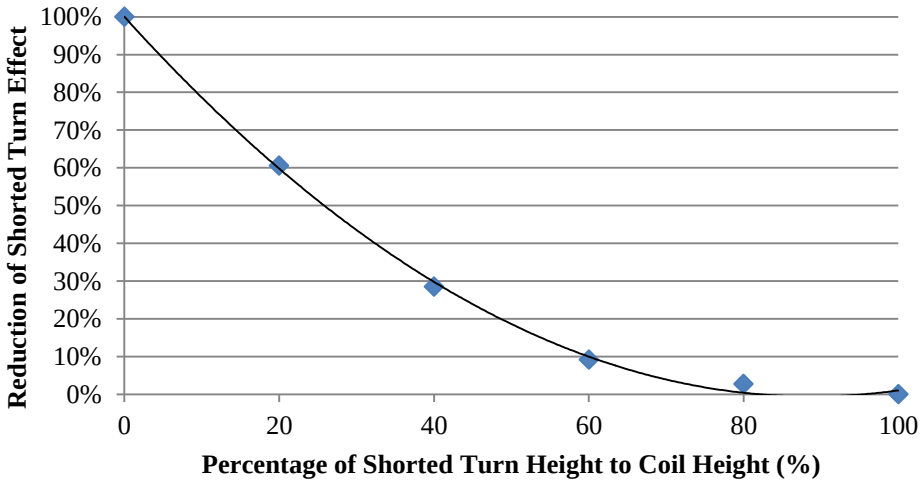

Figure 4-18. The reduction of shorted turn effect based upon a change in the shorted coil height relative to the primary coil.

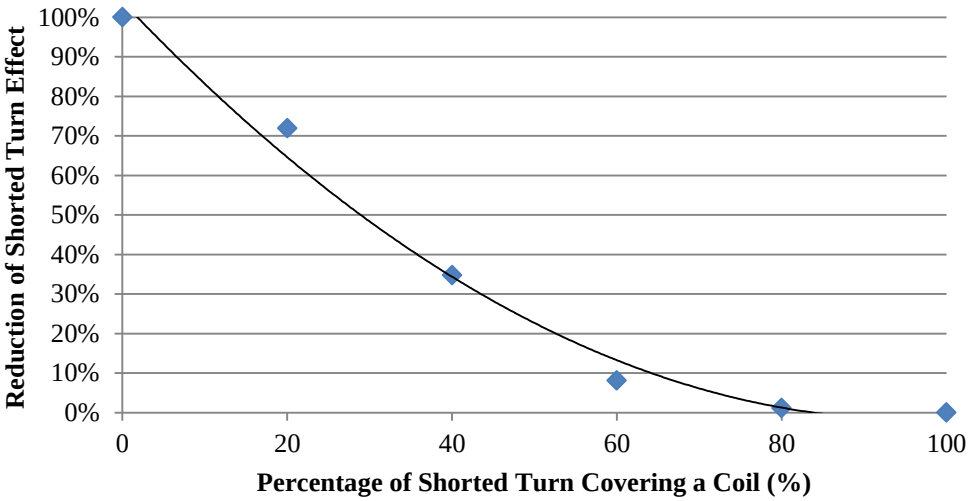

Figure 4-19. The reduction of shorted turn effect based upon a change separation between the coil and shorted turn.

Experiment D investigated the effects of varying the shorted turn thickness and therefore the resistance (R_{ST}) on the shorted effect; the results agreed with the hypothesis (derived from linear transfer function analysis of section 4.1.1) with the thicker (lower R_{ST}) shorted turn producing the greatest magnitude of admittance around the breakpoint frequency and a reduced phase lag also around this frequency. The thinner, higher resistance shorted turns did however display the smallest phase lag at 1000Hz (figure 4.20).

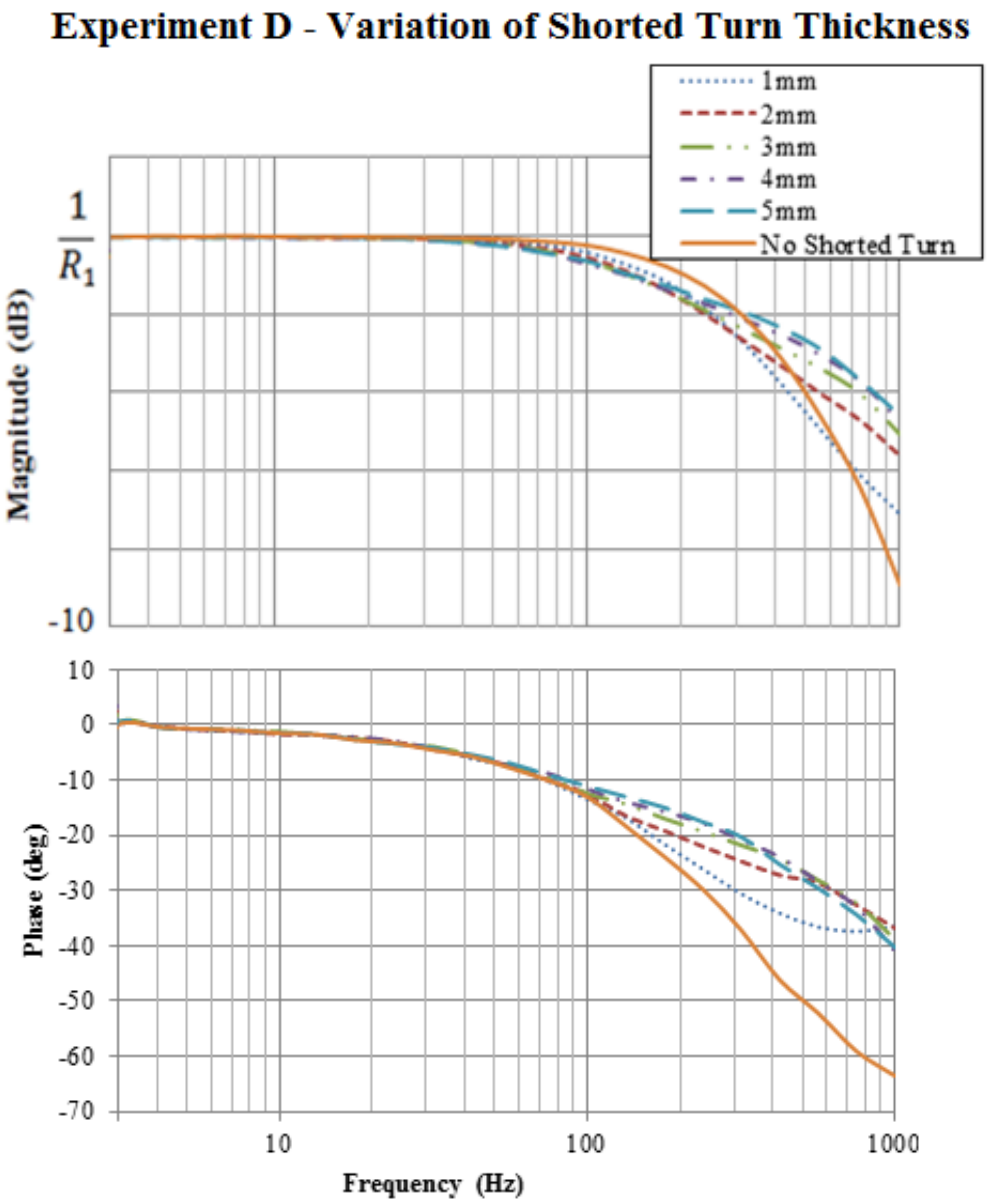

Figure 4-20. Experiment D (fig. 4-11): A Bode plot of Y_{COIL}, varying height of a shorted turn fitted over a primary coil.

Experiment E used terminal posts (wire clamps ensuring a good electrical contact) to connect various gauge wire across a slit, to investigate the possibility of connecting electrical components to the shorted turn in series. It was hypothesised that whilst the shorted turn with a full slit alone would completely remove the shorted turn effect, connecting across the terminals would restore the magnitude of this effect again. Both of these hypotheses were false as the full slit produced a very small increase in coil admittance (fig. 4-21) at high frequencies over a coil with no shorted

turn; the likely cause of this was small circulating eddy currents. The full slit produced comparable results to connecting wire across this slit, suggesting that it would not be possible to control this type of shorted turn using electrical components such as relays due to the high contact resistance, as even the relatively low total contact resistance of 20mΩ for the terminal posts was too large in comparison to the shorted turn resistance (R_{ST}) of 0.28mΩ to produce a shorted turn effect.

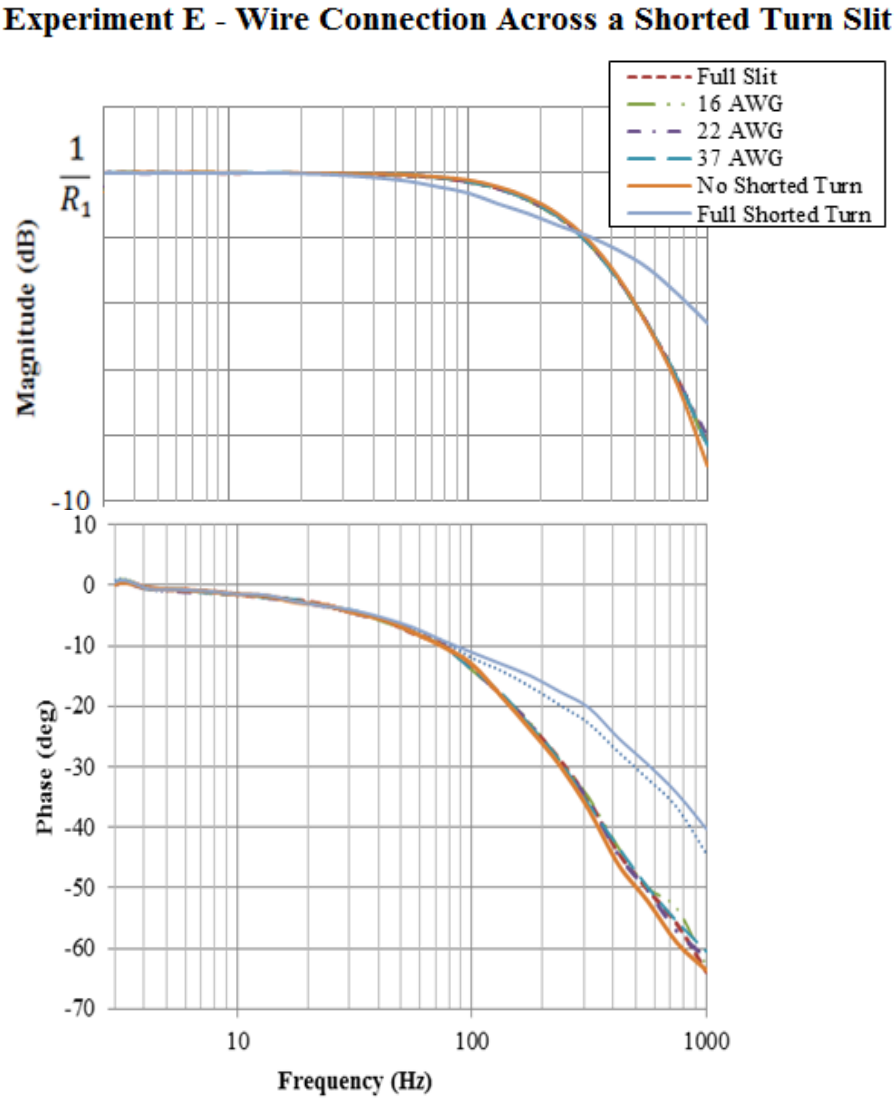

Figure 4-21. Experiment E (fig. 4-12): A Bode plot of Y_{COIL}, varying the gauge of wire connected across a shorted turn with a full slit fitted over a primary coil.

Experiment F used enamelled copper wire, wound around the outside of a coil to make a “shorted coil” (S-Coil); two S-Coils were formed a thick 14 SWG (Standard

Wire Gauge) coil and a thinner 22 AWG (American Wire Gauge) coil. Based on the parametric analysis of section 4.1.1, it was hypothesised that an S-Coil with more turns (large N_{ST}) and therefore larger inductance (L_{ST}) would produce greater coil admittance at high frequencies. Figures 4-22 and 4-23 show that these hypotheses were accurate; further authenticating the validity of the design recommendations of section 4.1.1. The S-Coil Bode plots also showed that the thicker gauge wire (small R_{ST}) S-Coil however produced comparable effects with as little as 20 turns (fig. 4-22) whereas the thinner (larger R_{ST}) wire required 100 turns (fig. 4-23); this agreed with the hypothesis as a larger shorted turn resistance (R_{ST}) would require a smaller turns ratio $\left(\frac{N_1}{N_{ST}}\right)^2$ and therefore a larger amount of S-Coil turns (N_{ST}) to produce the same apparent resistance (R_2).

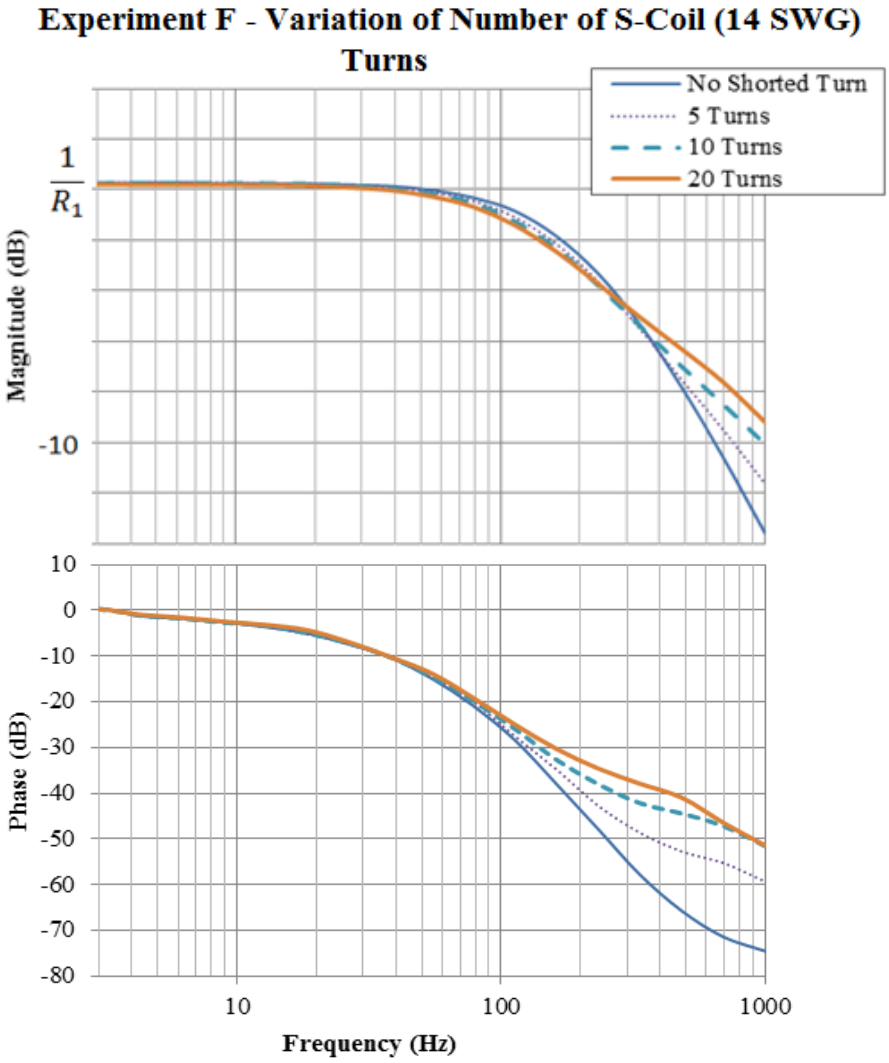

Figure 4-22. Experiment F (fig. 4-13): A Bode plot of Y_{COIL}, varying the number of turns of a 14 SWG thick S-Coil around a primary coil.

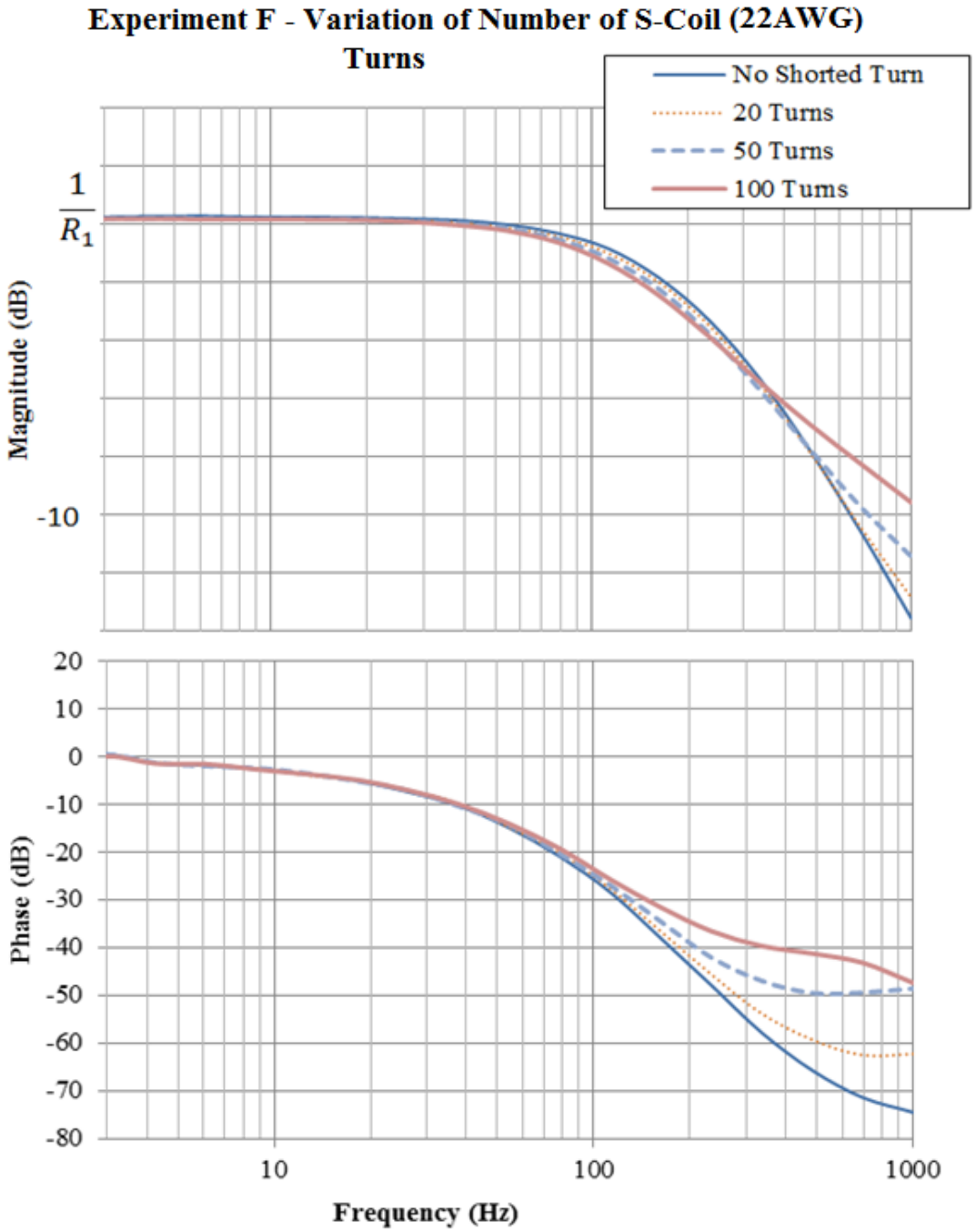

Figure 4-23. Experiment F (fig. 4-13): Frequency response plots of Y_{COIL}, increasing the number of turns in a thin (22 AWG) S-Coil.

Connecting a switch across the S-Coil supported the hypothesis that the contact resistance of the terminal posts was too large when compared to the resistance of the shorted turn to produce a significant shorted turn effect (fig. 4-21). This was as a switch connected across the higher resistance (0.50Ω) 22 AWG wire, produced a

much more significant shorted turn effect than when connected to the lower resistance (0.11Ω) 14 SWG wire (figs. 4-24 and 4-25).

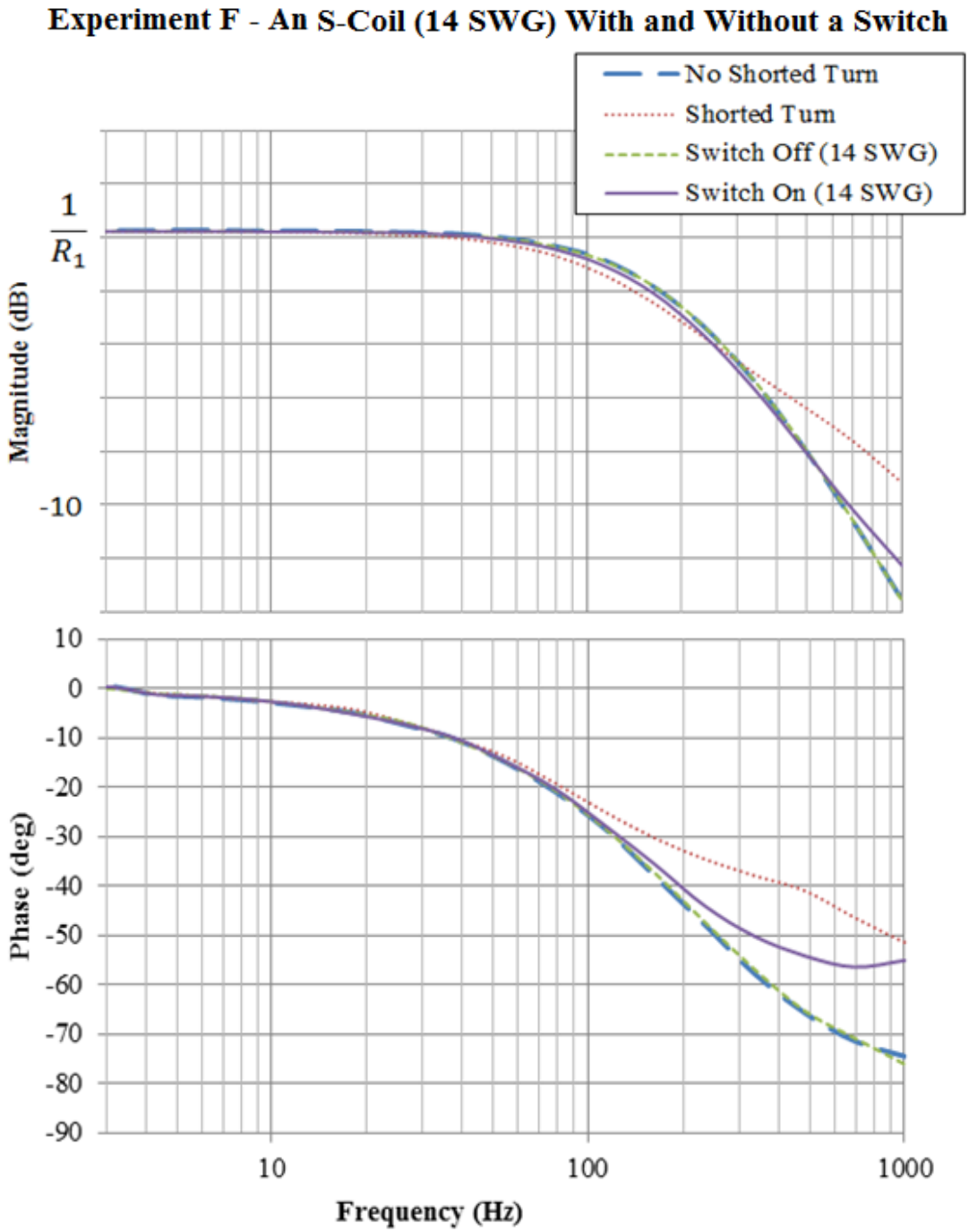

Figure 4-24. Experiment F (fig. 4-13): A Bode plot of Y_{COIL} with a thick (14 SWG) S-Coil and switch.

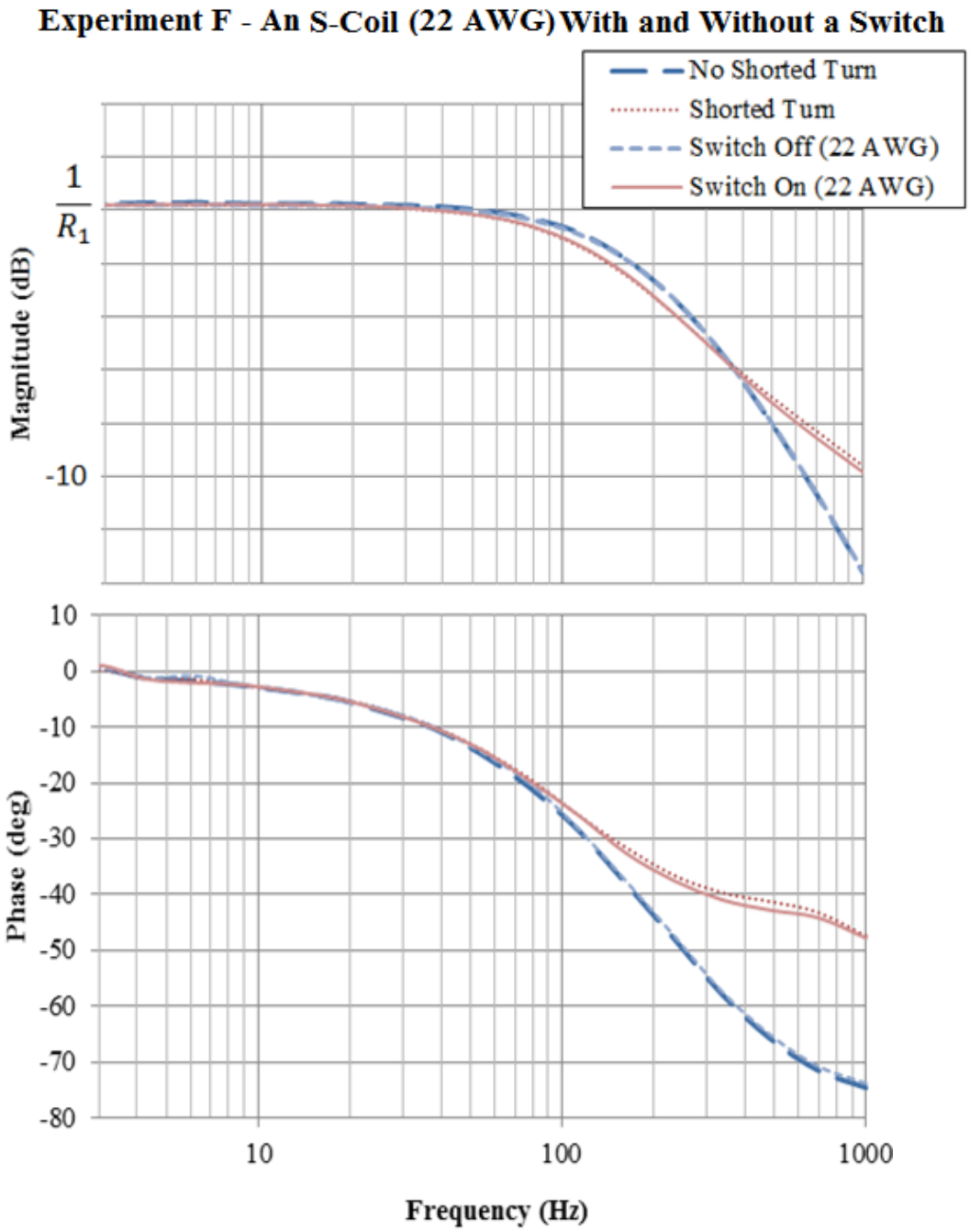

Figure 4-25. Experiment F (fig. 4-13): A Bode plot of Y_{COIL} with a thin (22 AWG) S-Coil and switch.

4.2. FORCE RESPONSE

Experimentation and theoretical analysis demonstrated that a shorted turn increased the apparent primary coil admittance at frequencies above its breakpoint frequency. This section investigates whether or not this increase in coil admittance could produce an increase in the force generated; or whether the actuator's motor constant was also frequency dependent.

Investigation into the shorted turn-force relationship was conducted using the test rig in both configurations A and B (figs. 3-2 to 3-3). It was hypothesised that K_M would remain consistent throughout the range of experimental frequencies.

An experimental model was then derived for the relationship between the shorted turn parameters (resistance and inductance) and force. This would help create design criteria for maximising force response.

4.2.1. FORCE EXPERIMENTATION SETUP

The test rig was set up to apply force against the load cell, ensuring a positive force at all times to avoid the shaft and load cell losing contact. To maintain shaft-load cell contact an offset was applied to the demand signal meaning that all aspects of the force output would be positive.

The motor constant (K_M) is the force from the load cell divided by the amplitude of the sinusoidal primary coil current (this is only considering the fundamental frequency and ignoring any harmonics due to distortion). To ensure that the coil current and therefore force remained constant throughout the experimentation, the amplifier was used in current-control mode.

4.2.2. FORCE EXPERIMENTAL RESULTS

Table 4-1 shows a range of motor constants for configurations A and B at increasing values of amplifier demand at a fixed frequency. It would be expected that the K_M would be constant throughout all demands as the force should have the same relationship to current irrespective to the demand voltage. However as can be seen from the table as the motor constant shows some non-linearity, this may be due to hysteresis effects, however this effect should not affect the experimentation as the demand is kept at a constant amplitude sinusoidal voltage over the range of experimental frequencies.

Demand (V)	Configuration A Motor Constant - K_M	Configuration B Motor Constant - K_M
0.1	0.823	4.921
0.2	0.841	5.735
0.3	0.851	6.050
0.4	0.852	6.243
0.5	0.852	6.376
0.6	0.854	6.481
0.7	0.860	6.556
0.8	0.861	6.642
0.9	0.864	6.717
1.0	0.865	6.777

Table 4-1. Motor Constants of the test rig at a fixed frequency in configurations A and B.

In order for the increase in coil admittance caused by the shorted turn to translate into a greater force, a constant K_M should be seen on the Bode plots of systems with a shorted turn. Otherwise additional frequency-dependent effects were added by the shorted turn. Figure 4-26 shows a Bode plot of the motor constant of a system with no shorted turn, at lower frequencies the motor constant exhibits no frequency dependent affects however there were some significant resonant effects at frequencies in excess of 70Hz; this meant that there were peaks which produced a larger motor constant. Some of these peaks were characterised by the resonance calculations of section 3.3 and corresponds to the peaks found in the experimental results for both configurations A and B. However, there are additional resonant

modes that, due to the complexity of the test rig system mechanics, were not modelled. Although the resonance calculations only accounted for 4 out of the multiple modes of vibration, the accuracy of these modes were significant enough to assume that this represented a system with a constant K_M and that any deviation from this was due to the resonant effects.

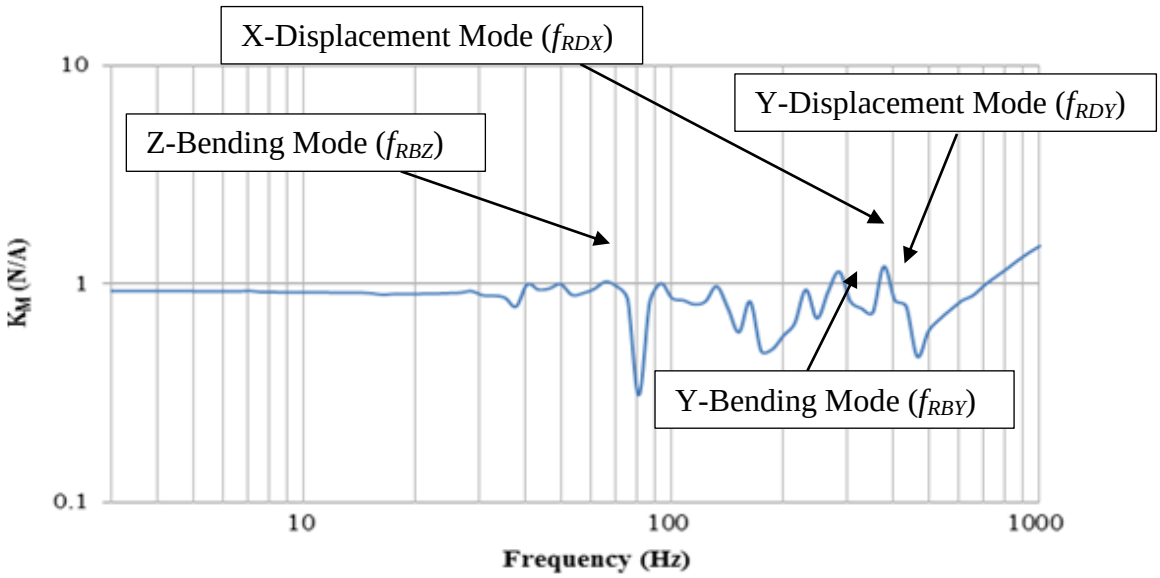

Figure 4-26. Resonant peaks of configuration A

Figure 4-27 illustrates that the shorted turn reduces the motor constant at high frequencies, meaning that a smaller magnitude force was recorded for the same magnitude of primary coil current.

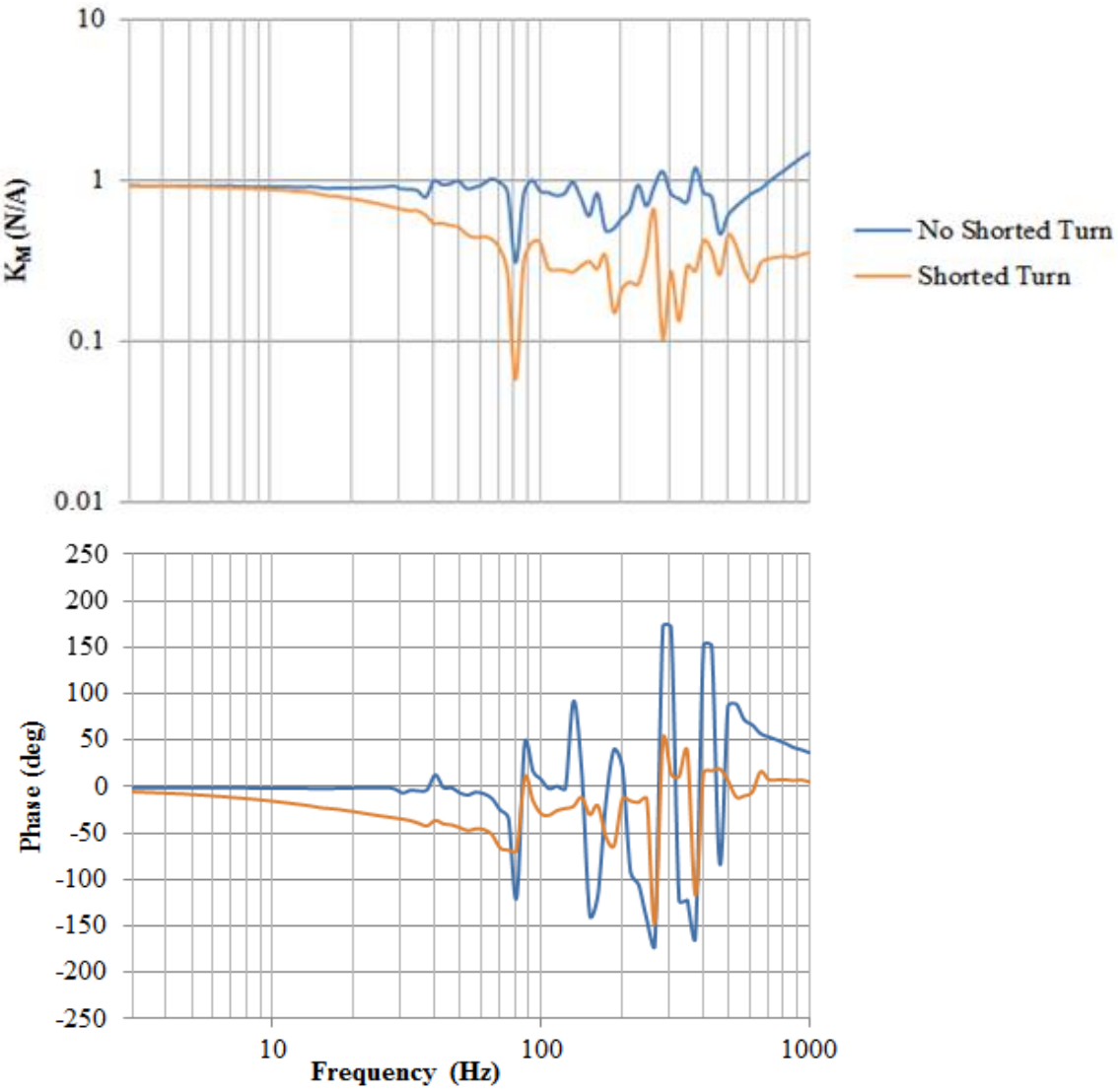

Figure 4-27. A Bode plot of the motor constant of configuration A with and without a 5mm thick shorted turn.

Figure 4-28, the Bode plot of the motor constant of configuration B, due to small magnitudes of currents at high frequencies, was only reliable up to 400Hz. These small magnitudes of coil current were due to the inherently high motor constant of this configuration limiting the maximum current that could be applied before the low friction system became unstable in resonant conditions.

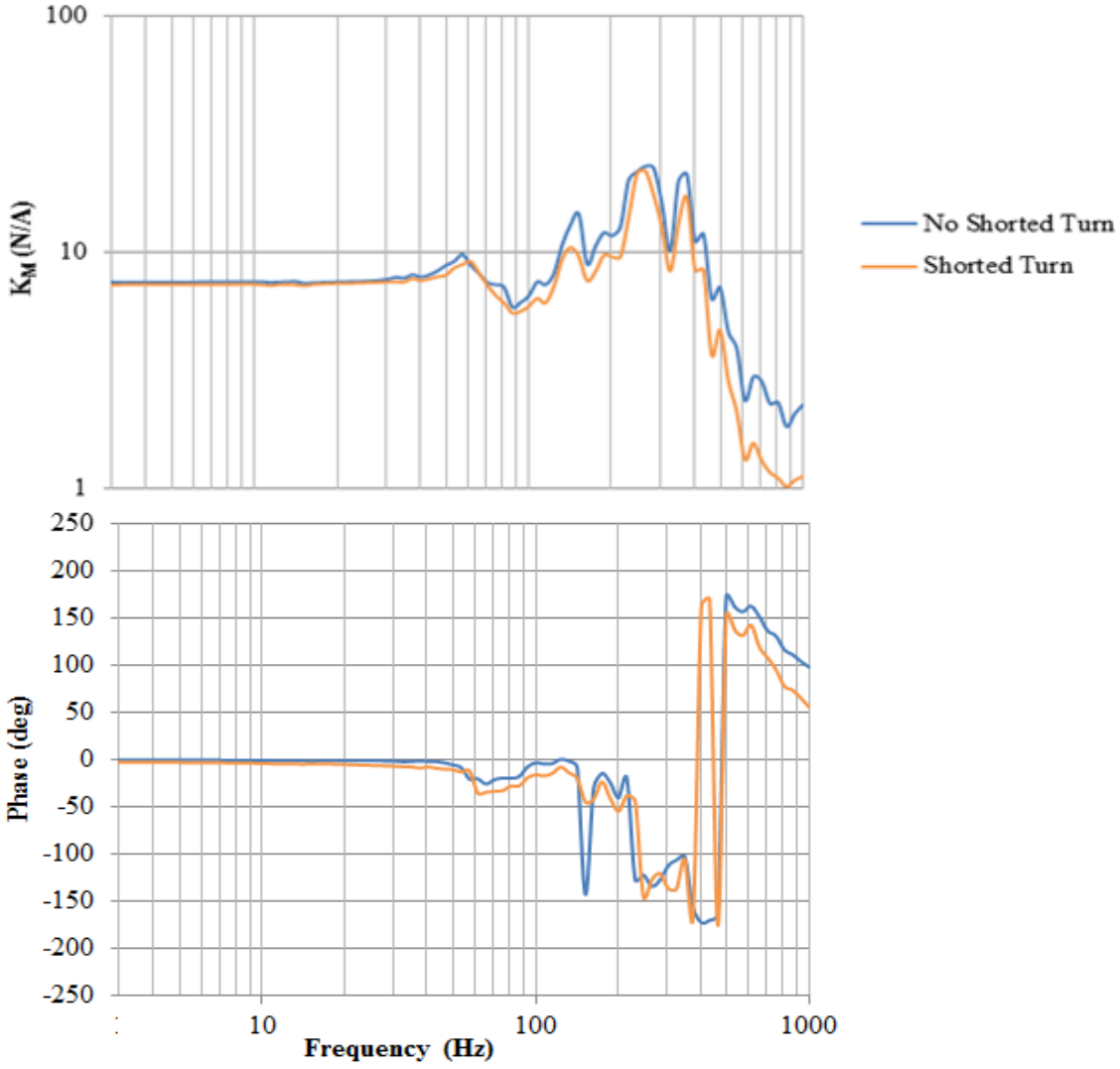

Figure 4-28. A Bode plot of the motor constant in configuration B, with and without a shorted turn.

Although the shorted turn reduced the magnitude of the force at higher frequencies it also reduced the magnitude of resonant peaks in the system response for both configurations. This may be beneficial in producing damping effects as the magnitude of resonant peaks of the Bode plots were attenuated in both configurations A and B. To provide a demonstration of how resonant peaks could manifest in practice, step responses was conducted. Figures 4-29 and 4-30 confirm that damping was produced by the shorted turn as the settling time with the shorted turn was significantly reduced (the settling time, to within 5% of steady state was 0.45s for a system without a shorted turn, to only 0.035s for the shorted turn - a 92% reduction in settling time).

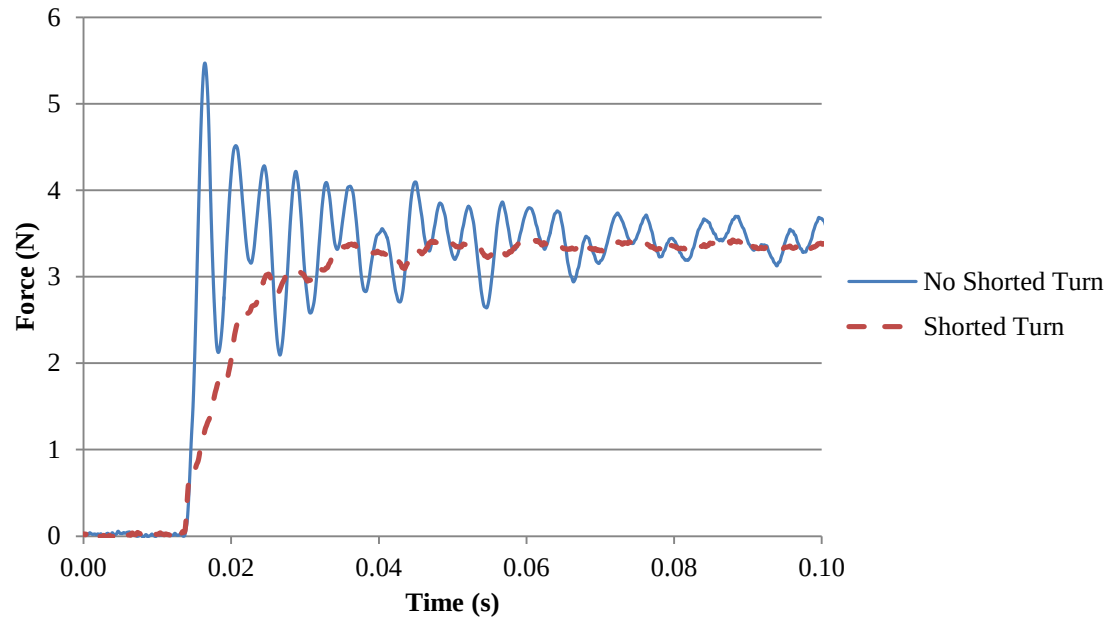

Figure 4-29. The effect of a shorted turn on a step response of force.in configuration A.

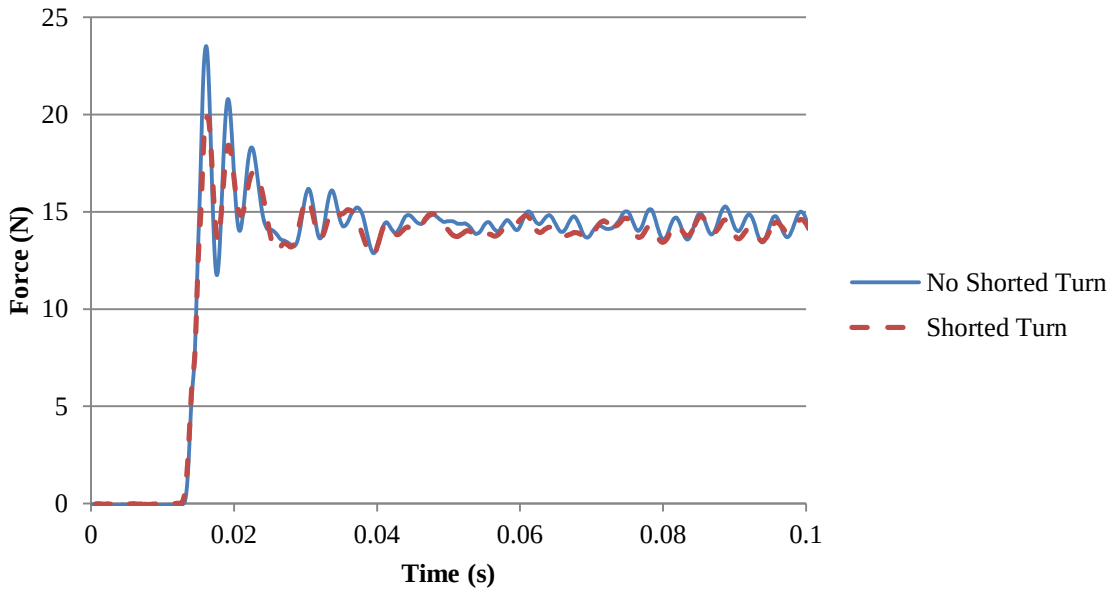

Figure 4-30. The effect of a shorted turn on a step response of force.in configuration B.

4.2.3. FORCE ANALYSIS

As shown by figures 4-29 and 4-30, the motor constant of a coil is reduced at high frequencies when a shorted turn is utilised. This discrepancy may be described by a decrease in the effective total coil current, $I_{T.}$ To model this reduction in motor constant K_M Figure 4-31 was used to extend Wagner's shorted turn model; creating a magnetising current based model of admittance to gain a greater insight into the effects of a shorted turn on magnetising current (I_M); in this model Z_1 represents the coil impedance and Z_2 represents the shorted turn impedance and Z_{12} represents the mutual inductance.

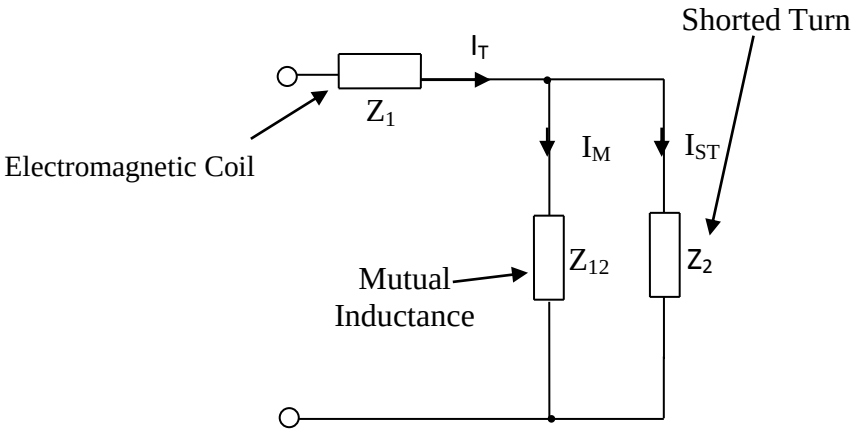

Figure 4-31. Wagner's shorted turn circuit diagram in terms of impedance.

A transfer function of magnetising current admittance was calculated using figure 4-31. From this figure, the total current is given using ohms law:

$$Z_{12} \parallel Z_{12} = \frac{Z_{12}Z_2}{Z_{12} + Z_2} \tag{4.14}$$

$$I_T = \frac{V}{Z_1 + \frac{Z_{12}Z_2}{Z_{12} + Z_2}} \tag{4.15}$$

Modelling as a current divider produces the following relationship between voltage and magnetising current.

$$I_M = \frac{Z_2}{Z_{12} + Z_2} I_T \tag{4.16}$$

$$I_M = \frac{Z_2}{Z_{12} + Z_2} \times \frac{V}{Z_1 + \frac{Z_{12}Z_2}{Z_{12} + Z_2}} \tag{4.17}$$

$$I_M = \frac{Z_2 V (Z_{12} + Z_2)}{(Z_{12} + Z_2)[Z_1(Z_{12} + Z_2) + Z_{12}Z_2]} \tag{4.18}$$

A transfer function of magnetising current admittance is obtained by taking Laplace transforms and substituting for the actual impedances $Z_1 = R_1 + L_1 s$, $Z_2 = R_2 + L_2 s$ and $Z_{12} = L_{12} s$.

$$\frac{I(s)}{V(s)} = \frac{[L_2 \Psi s^2 + R_2(2\Psi)s + {R_2}^2]}{\Psi \varphi s^3 + \{R_2 \varphi + (L_1 + L_{12})\lambda\} s^2 + \{R_2 \lambda + R_1 R_2 \Psi\} s + R_1 {R_2}^2} \tag{4.19}$$

$$\psi = (L_{12} + L_1) \tag{4.20}$$

$$\Psi = (L_{12} + L_2) \tag{4.21}$$

$$\varphi = (L_1 \Psi + L_{12} L_2) \tag{4.22}$$

$$\lambda = (R_1 \Psi + R_2 \psi) \tag{4.23}$$

Plotting the results of this transfer function showed that the thicker, lower resistance shorted turns producing a lower frequency drop in the admittance of magnetising current, Y_M (fig. 4-32).

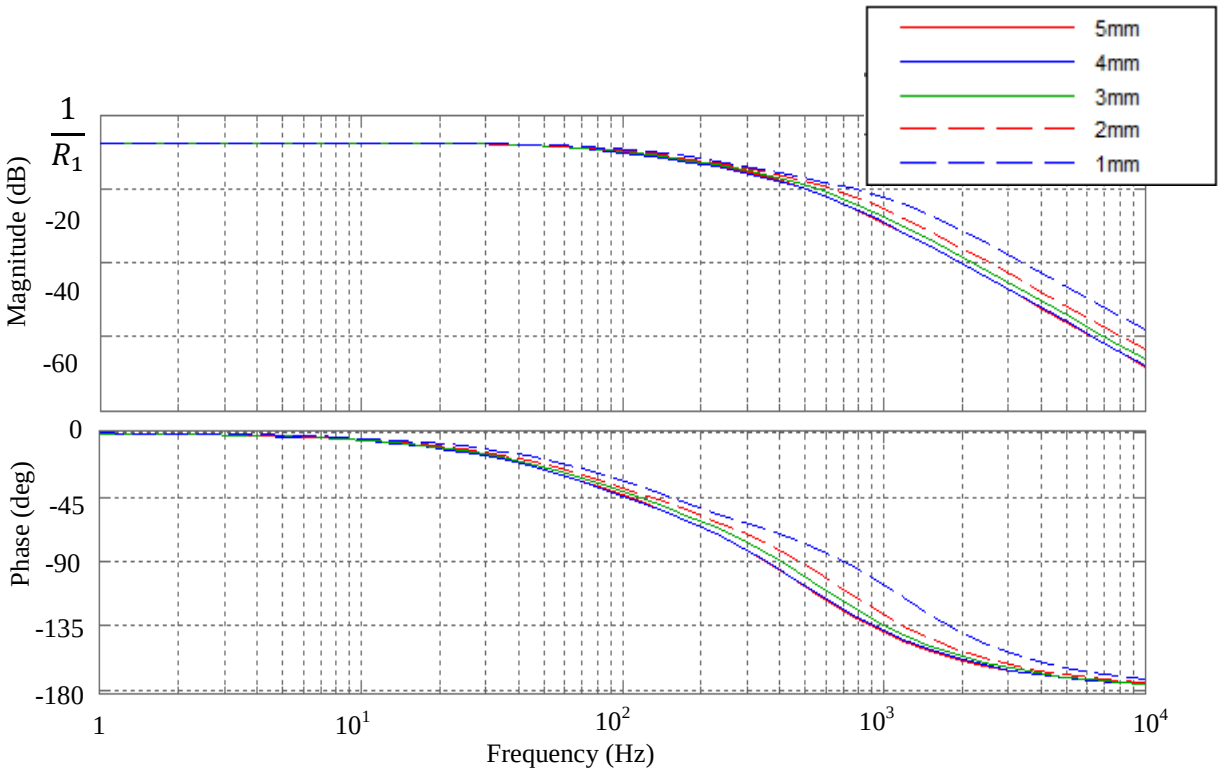

Figure 4-32. Calculation of Y_M with various thicknesses of shorted turn.

The results of figure 4-32 (the calculated values for magnetising current admittance with various thicknesses of shorted turn) were directly comparable with the experimental data of the force produced per volt, $G_M(s)$ (fig. 4-33), meaning that the motor constant between force and magnetising current (K_{MM}) was constant.

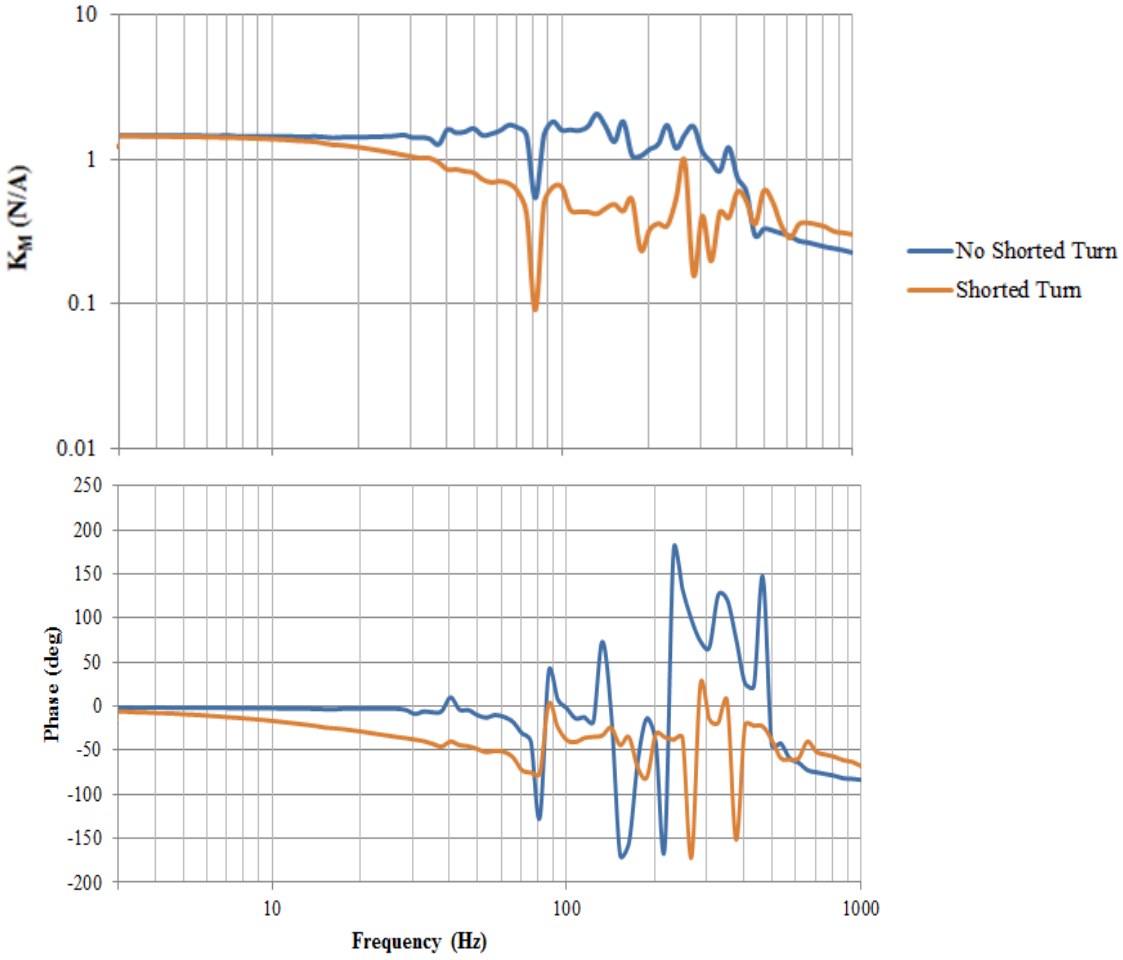

Figure 4-33. Experimental results of $G_M(s)$ with various thicknesses of shorted turn.

4.3. DISPLACEMENT RESPONSE

Force measurements demonstrated that a shorted turn produces a damping effect, attenuating resonant peaks and suppressing the overshoot in a step response of force (figs. 4-29 and 4-30). This section will investigate that relationship between a shorted turn's resistive (R_{ST}) and inductive (L_{ST}) properties and damping. To investigate this relationship, an impulse was applied to the mover whilst displacement measurements of the oscillatory decay were taken using the laser sensor. A pendulum based model was then derived and used to identify a damping constant in N/ms^{-1}.

Comparison of these damping constants were used to produce a relationship between shorted turn parameters and the damping constant, this will allow a shorted turn to be designed in such a way that a system would experience a minimal high frequency force reduction but maximal damping is produced. This will be particularly useful for systems that utilise PID feedback control, as attenuation of certain disturbances and resonances may allow greater magnitudes of controller gains to be applied before the system begins to become unstable.

4.3.1. DISPLACEMENT EXPERIMENTATION SETUP

In order to investigate damping, the load cell was removed from the test rig set up so that the mover was unimpeded; the laser sensor was used to take readings without disturbing the movement of the shaft and mover. An impulse of 0.12Ns (a force of 12N for a period of 0.01s) was applied to the mover and the decaying oscillatory motion was recorded. The magnitude of impulse was selected because it produced a large displacement relative to the full test rig range. Analysis of the experimental results was performed by varying the damping constant (C) of a damped pendulum model to match the system behaviour. The system was matched based on the logarithmic decrement (the natural logarithm of two successive peaks) of the first and second peaks, the second and third peaks and settling time (within 5% of equilibrium position).

Shorted turns of various thicknesses were tested, as previous experimentation suggested that high frequency force was reduced with shorted turn thickness, it was hypothesised that damping would increase with thickness. S-Coils with a range of resistances and inductances were also tested to ascertain whether it was possible to control the damping effect.

4.3.2. DISPLACEMENT EXPERIMENTATION RESULTS

Figure 4-34 shows the settling time of a system in configuration A with no shorted turn. It can be seen that the system reaches its equilibrium position in excess of the 5s time period (a settling time of 5.4s). However the decay in displacement magnitude illustrates the inherent damping in the test rig, due to air resistance and the movement of the permanent magnets over the iron stator inducing eddy currents, dissipating energy and damping the motion.

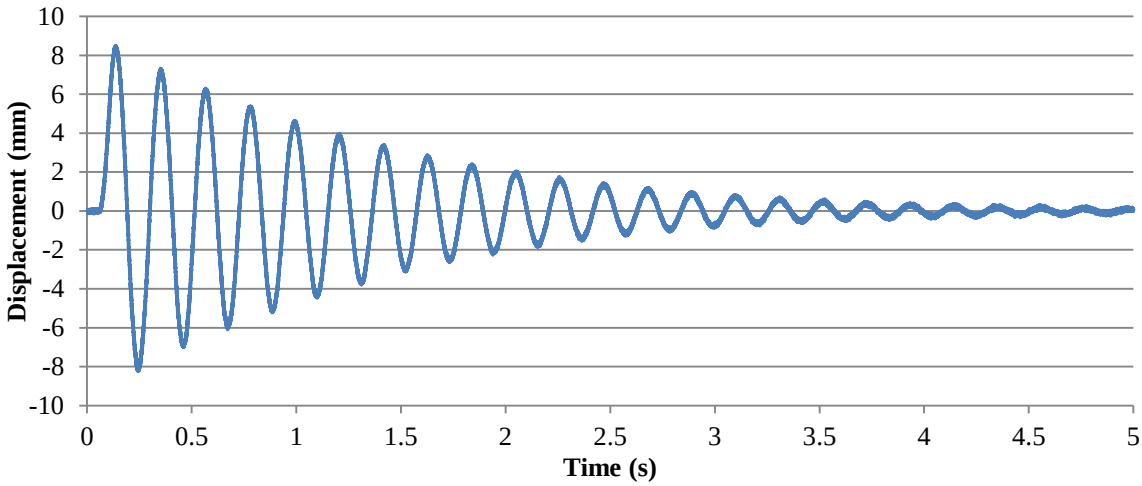

Figure 4-34. Impulse response of configuration A with no shorted turn.

Figure 4-34 was used as the baseline displacement response characterising a system with no shorted turn damping, therefore if a system was to exhibit additional damping it would be expected that the low frequency oscillations would decay faster. One example out of 5 repetitions showed that adding a shorted turn produces a displacement response as shown in figure 4-35, the shorted turn produces a significantly reduced settling time with a settled motion (within 0.2mm of displacement) reached after a time period of just 2.3s ± 0.1s a 57.4% reduction in the settling time when compared to the baseline experiment, demonstrating damping effects. It may also be seen that the amplitude of displacements have also significantly been reduced; this was true of both configurations. These results confirmed the findings of the step responses of section 4.2 with the shorted turn producing damping effects.

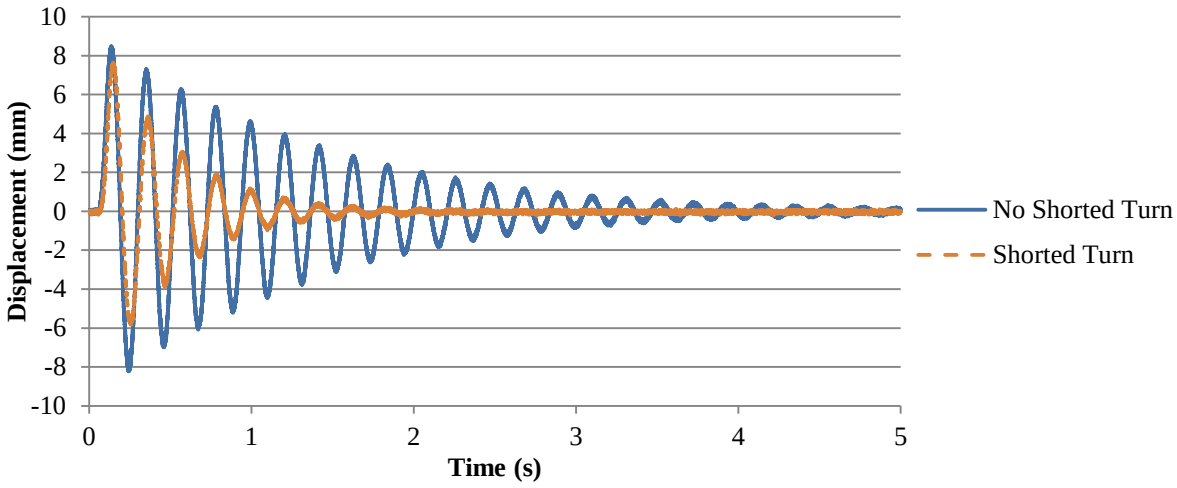

Figure 4-35. Impulse response of configuration A with and without a shorted turn.

Shorted turns of various thicknesses were used in experimental testing; experimental results were collected and analysed using pendulum-based modelling to fit damping constants to the experimental data (a more detailed description of this analysis may be found in section 4.3.3), with the results detailed in (Table 4-2). These results demonstrate a relationship between shorted turn thickness and the damping constant

Shorted Turn Thickness	Damping Constant - c
1mm	2.2
2mm	2.4
3mm	2.7
4mm	3.2
5mm	4.1

Table 4-2. The relationship between the thickness of shorted turn and damping constant – see section 4.4.3 for damping constant derivation and analysis.

Plotting the damping constants of table 4-2 against thickness (fig. 4-36) shows that the damping constant is proportional to the square of the thickness, this suggests a relationship between shorted turn damping and eddy current damping; this is described in more detail below.

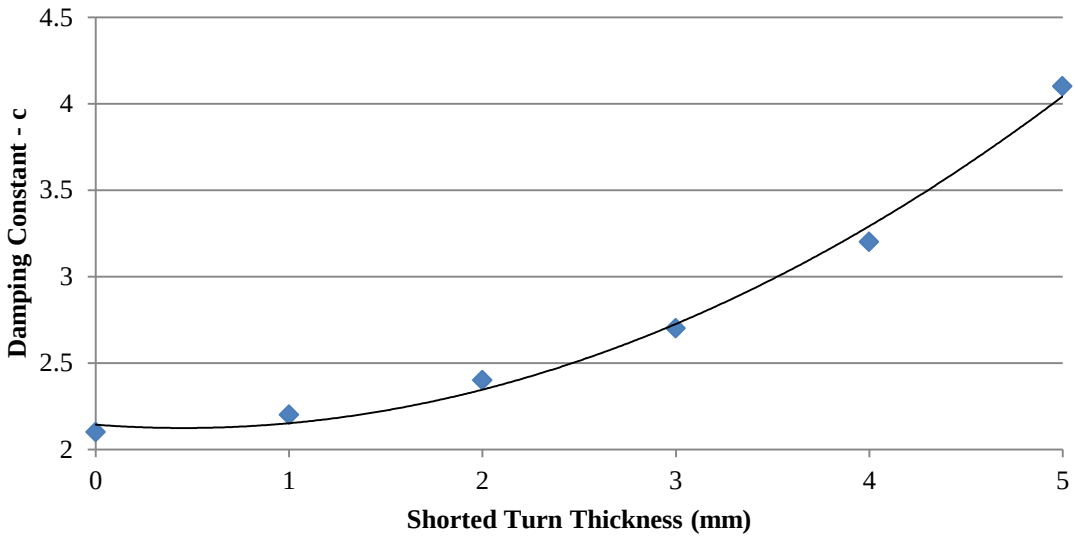

Figure 4-36. The effect of shorted turn thickness on the damping constant.

The power dissipated from a system due to a linear damper with damping constant, c:

$$P = cv^2 \tag{4.24}$$

The power dissipated by eddy current damping is given by:

$$P_{EDDY} = \frac{\pi^2 B_P^2 t^2 f^2}{K_{EDDY} \rho D} \tag{4.25}$$

where B_P is the peak magnetic flux density, t is the thickness perpendicular to the magnetic field, f is the speed at which the magnetic field is changing (frequency) in Hz, ρ is the resistivity, D is the specific density and K_{EDDY} is a constant that is related to set up that is causing the eddy current damping (typically 6 for thin sheets or 12 for wires) (Oatley, 1976):

As the peak magnetic flux density, resistivity and specific density are constant throughout the experimental testing these may be replaced with a constant K_{EVAL} giving the following relationship:

$$P_{EDDY} = K_{EVAL} t^2 f^2 \tag{4.26}$$

$$c_{EDDY} = K_{EVAL} t^2 \tag{4.27}$$

$$c_{EDDY} \propto t^2 \tag{4.28}$$

Showing that the power dissipated from eddy current damping would be proportional to the thickness squared as with the experimental results.

Investigating the damping produced by an S-Coil, showed that compared to a typical (single loop) shorted turn the maximum damping constant of configuration A was equivalent to a 2mm thick single loop traditional shorted turns. Repeating the S-Coil experimentation for configuration B however revealed that the damping constant achieved did increase with the number of turns (table 4-3); this was found to be due to the geometrical design of the stator and coil.

	Damping Constant - c (Configuration A)	**Damping Constant - c (Configuration B)**
No S-Coil	2.1	2.4
S-Coil (20 Turns)	2.3	2.7
S-Coil (50 Turns)	2.3	3.1
S-Coil (50 Turns) -Switch On	2.3	3.1
S-Coil (50 Turns) -Switch Off	2.1	2.4
Wide S-Coil (20 Turns)	2.8	n/a

Table 4-3. The relationship between the number of S-Coil turns and damping constant – see section 4.4.3 for damping constant derivation and analysis.

As a link between shorted turn thickness and the damping constant has been demonstrated, this would explain why the damping constant would increase with the number of S-Coil turns in configuration B (which had a smaller coil height, therefore more turns equalled a thicker coil, d_{ST}) and this would not be the case with configuration A (where many turns could be applied for a very small change in coil thickness, d_{ST}) (fig. 4-37).

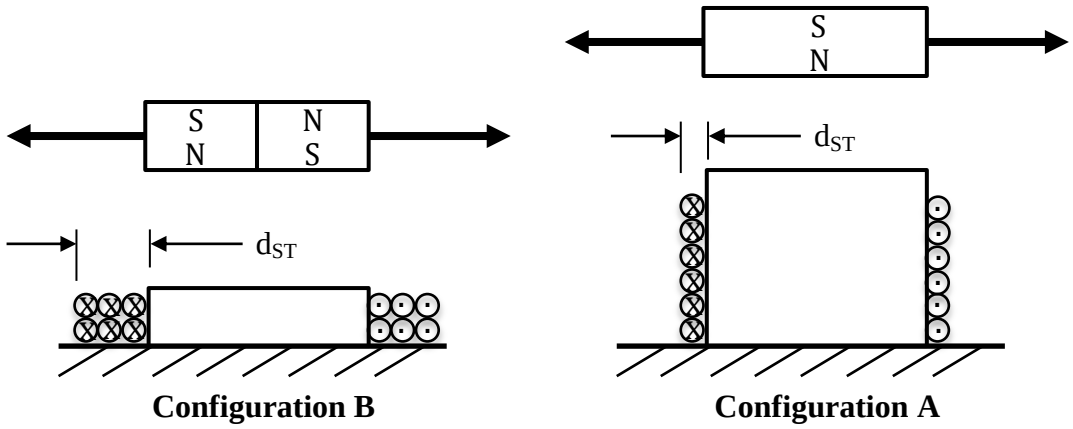

Figure 4-37. The variation in S-Coil thickness in different configurations for the same number of turns.

In order to test the finding that the damping produced by the S-Coil was dependent on its arrangement; an S-Coil, of identical length and gauge to the 20-Turn S-Coil previously tested on configuration A, was moulded into a spiral shape meaning that a larger overall thickness could be produced. This was found to produce a significantly larger damping force (fig. 4-38) confirming that it is the thickness of the S-Coil relative to the permanent magnet (moving in the x-direction) that produces the damping force. The damping constants produced with the S-Coil may be found in Table 4-3.

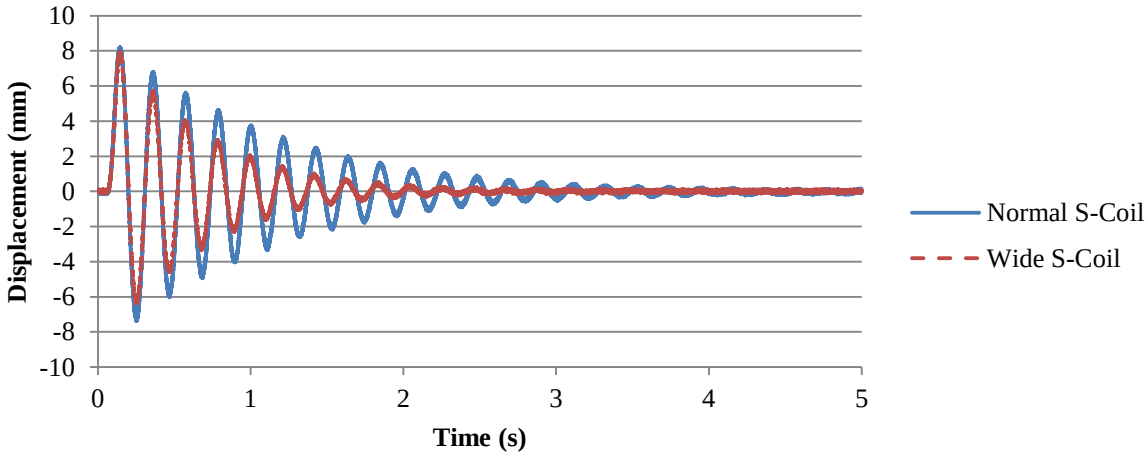

Figure 4-38. Impulse response of a spiral vs. helical S-Coil.

4.3.3. DISPLACEMENT ANALYSIS

In order to obtain quantitative results in a form that would be applicable for modelling purposes, a system model was created to predict the damping constant for a given shorted turn based upon the experimental results of the displacement amplitude and settling times.

A pendulum model was used to represent the flexure system of the test rig (fig. 4-39).

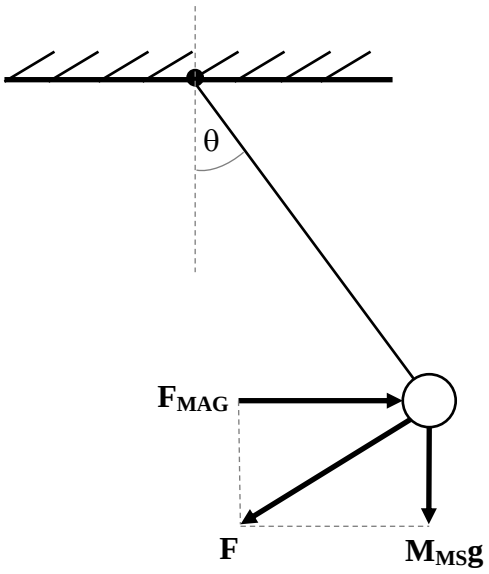

Figure 4-39. Pendulum model of the test rig flexures.

$$\ddot{\theta} = \frac{F_{MAG}}{M_{MS} l} - + \frac{g}{l}\theta \tag{4.29}$$

Figure 4-40 details a complete system (neglecting resonant effects) model using $\ddot{\theta}$ as shown in equation 4.29. This model may be analysed (from the pendulum model block) within Simulink to produce an output in terms of the displacement (x).

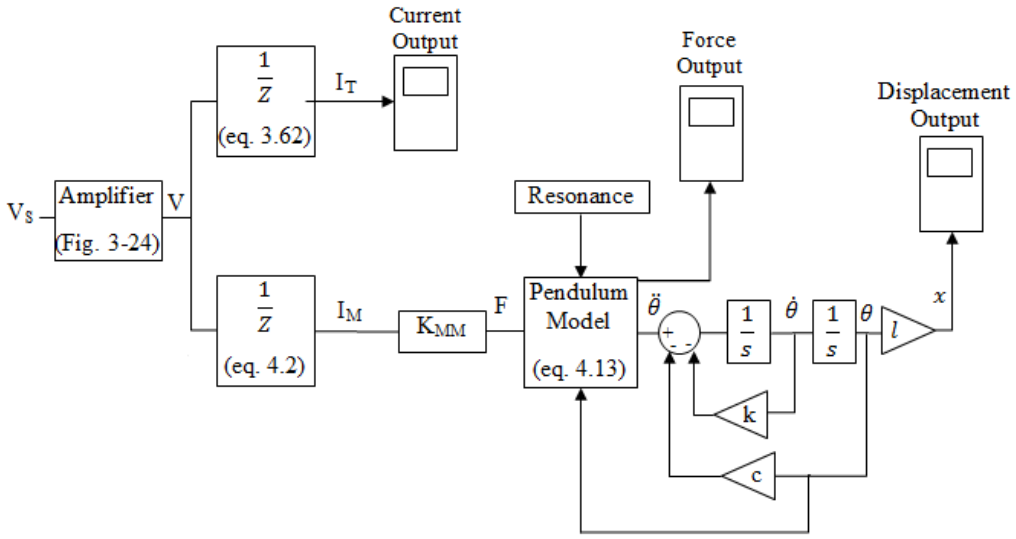

Figure 4-40. A complete system model of the test rig setup.

Using flexure stiffness (k_F) of 576.9N/m (obtained experimentally using Hooke's Law) and using the mass of mover and shaft in configuration A; the damping constant (C) may be calculated.

When real parameter values were used, the model produced results that matched both the amplitude and frequency of experimental test results (fig. 4-41). This showed that the system model (fig. 4-40) was an accurate representation of the actual test rig set up; allowing for reliable estimation of damping constants (C).

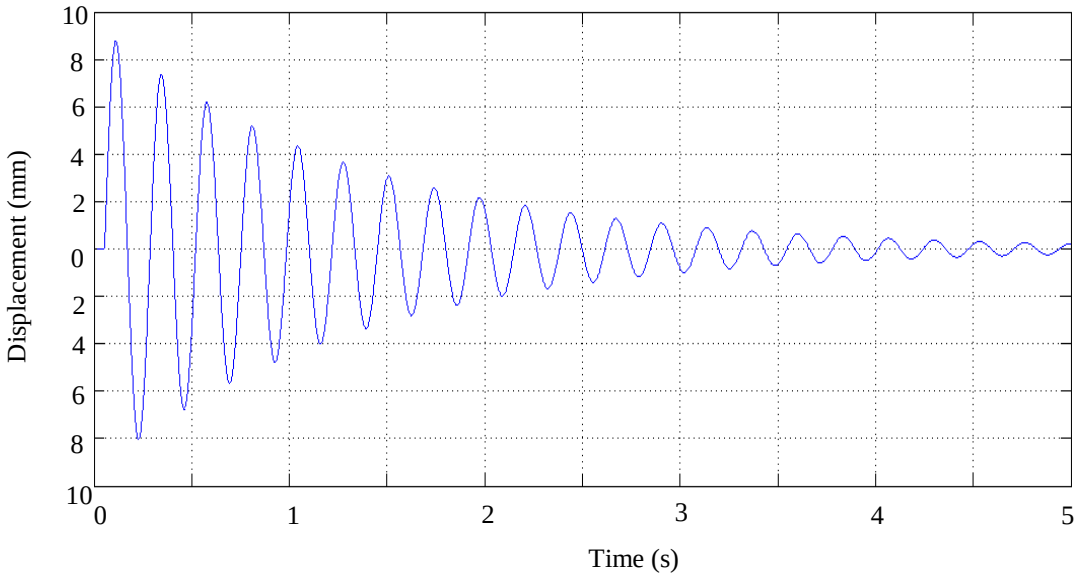

Figure 4-41. Simulation of the pendulum model displacement response.

5. Discussion

The results of chapter 4 demonstrate that a shorted turn reduces the high frequency phase lag and increases the high frequency coil admittance, meaning that a shorted turn will not only improve the transient response of the coil current, but (dependent on where the open-loop gain is at 0dB) may also increase stability margins; improving the dynamic performance and range.

There are however a range of frequencies around the breakpoint frequency whereby the shorted turn reduces the coil admittance. This is as the shorted turn zero (f_z) is always at a higher frequency than the first pole (f_{p1}); according to the linear transfer function analysis (section 3.1) the range of frequencies that experience this drop in admittance increases with shorted turn resistance. However this reduction in coil admittance does not reduce improvements in the current rise time, meaning that this is likely to only be of concern for systems that operate with very narrow gain margins around the breakpoint frequency.

To tune a shorted turn the results have shown that reducing resistance and increasing inductance are both beneficial for improving dynamic range and performance. When using a cylinder type shorted turn, reducing the resistance may be achieved by increasing the wall thickness, however (with aluminium) the benefits reduce after 3mm due to the skin thickness. The inductance may also be increased by taking steps to ensure that the flux leakage is kept as minimal as possible, for example an air gap between the coil and the shorted turn that is as small as possible.

The results show that a convenient way of “tuning” these parameters is using an S-Coil, an S-Coil may be used to increase the coil inductance and because of the turns ratio this also reduces the apparent resistance. Other benefits of an S-Coil are that it may be retrofit into existing devices, and the results of figure 4-25 also show that an S-Coil may be used in conjunction with electrical components to control the shorted turn effect.

Experimentation (figs. 4-24 and 4-25) suggests that to use electrical components, such as switches and relays, an S-Coil with a resistance comparable to the electrical

component to be connected in series is required. Varying the S-Coil resistance would best be achieved by selecting the gauge of wire accordingly and increasing the inductance (number of turns) until the required magnitude of effect is achieved.

Controlling a shorted turn would allow the benefits of an improved dynamic range and performance to be utilised whilst providing greater flexibility in mitigating any possible negative shorted turn effects; such as the "braking" effect on the acceleration and deceleration phases of a voice coil motor performance, as detailed by M. A. Moser (Moser, 1996). Based on Moser's work one possible control strategy would be to use a "switched off" shorted turn to maximise acceleration but a "switched on" shorted turn for the deceleration phase for a reduced move time. Figure 5.1 demonstrates how an S-Coil may be used in practise to improve device performance.

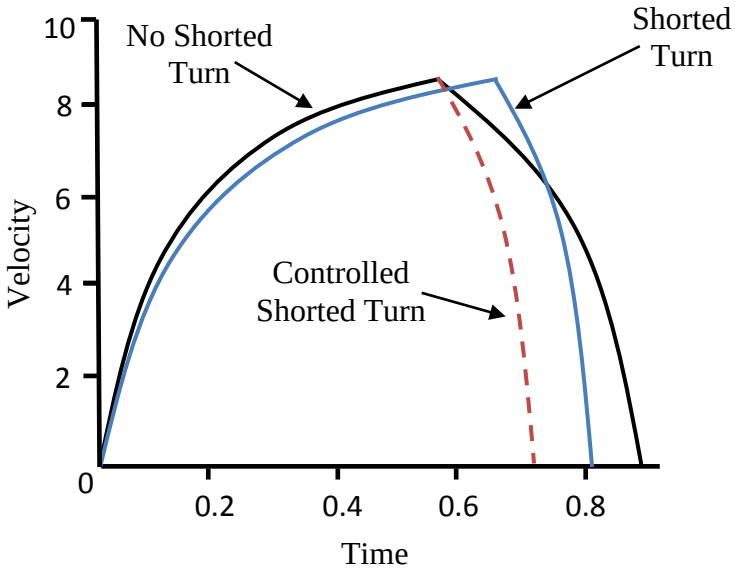

Figure 5-1. An example of controlling a shorted turn for improved device performance.

The control benefits and improvements in the current response produced by a shorted turn or S-Coil come at a cost with a reduction of the motor constant. The results of section 4.2 confirm the findings of Hirano (Hirano, Naruse, & Tsuchiyama, 1989) and show that the shorted turn does indeed reduce the motor

constant. This implies that whilst a shorted turn may improve the current response for faster initial acceleration, it is also likely to reduce the maximum velocity achieved after this initial larger current, due to the reduction in motor constant outweighing the improvements in current response. This explains why shorted turns are typically used in fast accelerating positioning devices, which tend to have a small range of movement, such as voice coil motors, as in this situation the initial current response is the most important for improving performance. This issue highlights another potential benefit for the control of an S-Coil in devices that have a larger range of motion, with the S-Coil being switched off after the initial current increase for faster overall device acceleration. Figure 5.2 demonstrates the effect of a shorted turn on device acceleration, whereby improvements in the current rise time improves the initial acceleration this is degraded later by the lower motor constant.

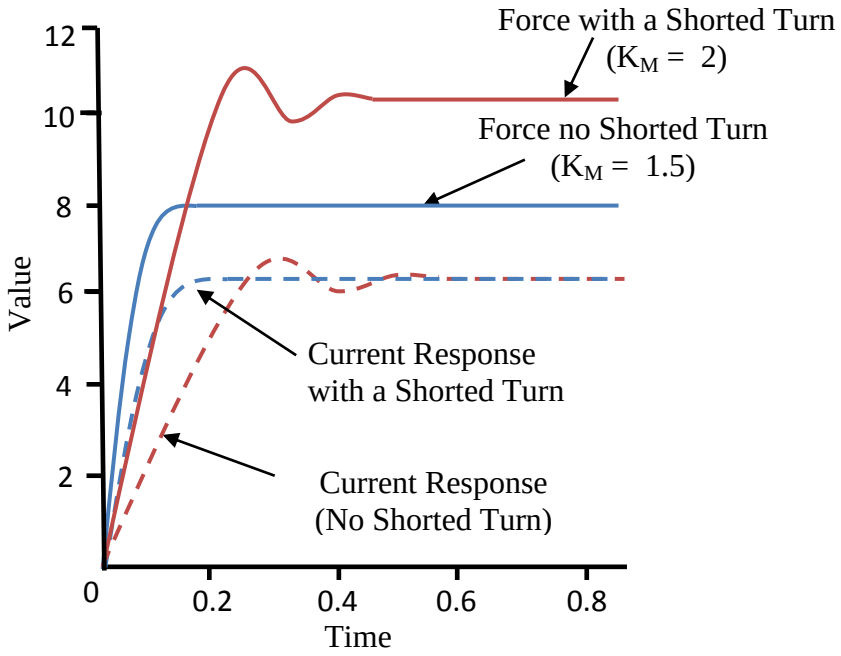

Figure 5-2. The effect of a shorted turn on force output.

The shorted turn has also been shown to produce eddy current damping with the results quantified in section 4.3. The cylinder type shorted turn has been shown to produce the most significant damping due to the wall thickness, however the S-Coil also produced damping effects, which like the current response may be controlled. This damping may be potentially useful for low friction systems, such as linear

motors, and may also increase stability margins allowing larger controller gains to applied for a more responsive system.

6. Conclusions

The experimental results of the previous chapter confirmed the validity and flexibility of a transformer circuit model (fig. 4-20) to represent the shorted-turn effect. To maximise the magnitude of the shorted turn effect the research has shown that shorted turns should be designed so that they are physically close to the primary coil with a low resistance; the exact shorted turn properties required are however application dependent. Parametric analysis has been shown to be a valuable design tool, allowing selection of the shorted turn parameters that would best suit any given application. Analysis also showed that a reduced shorted turn resistance will produce a lower break frequency for f_{p2}, producing an increase in coil admittance (relative to the primary coil) that would be around the primary coil breakpoint frequency (assuming constant values of shorted turn inductance and mutual inductance). A large shorted turn resistance (R_{ST}) may however also be beneficial, as this has the effect of moving the reduction of phase lag to a higher frequency allowing it to be utilised at frequencies where the primary coil admittance approaches 90 degrees; this may be particularly desirable as this could translate to improved stability margins.

The hypothesis that the magnitude of the shorted turn effect would change in relation to the physical separation of a shorted turn to the primary coil was confirmed with experiments A, B and C all producing the same result of a reduced magnitude of shorted turn effect with a larger physical separation (e.g. larger air gap, smaller percentage of shorted turn covering the coil). Experiments D, E and F also confirmed the parametric analysis; showing that a larger shorted turn resistance reduces the magnitude of the shorted turn effect, for a given inductance (L_{ST}).

Attempts to control the effect of a shorted turn were unsuccessful due to the large contact resistance of electrical components in comparison to the low shorted turn resistance (section 4.1.3). Therefore mechanical control methods that utilise flux leakage to control the shorted turn prominence are likely to be the most practical methods of modifying the effect of that type of a shorted turn. Moving the shorted turn by 60% would reduce the shorted turn effect by only 34.7% (based on the sum

squared difference – appendix 1) meaning that, dependent on the application, it may be necessary to completely remove the shorted turn from the coil.

An S-Coil is an extension of the shorted turn principle (chapter 1) which involves winding a secondary coil (with its terminals connected in a "shorted" manner) around the primary electromechanical device coil. This may allow the shorted turn effect to be utilised whilst adding controllability. Experimentation of a circuit breaking switch significantly reduced the magnitude of shorted turn effect of a thicker, lower resistance S-Coil, with a drop in the magnitude of the shorted turn effect of 24.1% (fig. 4-17) compared to just a 0.48% drop in the thinner coil (fig. 4-18). The thinner coil however required significantly more turns to produce a comparably distinct shorted turn effect. This highlighted that the main design consideration of this type of shorted turn is the apparent shorted turn resistance (R_2). For electrical components to be used with an S-Coil, it was found that the component's contact resistance must be of a similar magnitude, preventing an excessive increase in shorted turn resistance R_{ST}. To compensate for this increased resistance (R_{ST}) it is necessary to increase the number of turns in the S-Coil (N_{SC}), reducing the turns ratio and the apparent resistance.

Chapter 4 demonstrated the feasibility of controlling the shorted turn effect (figs. 4-17 and 4-18). This may be particularly beneficial in systems such as the rotary voice coil described by M. A. Moser (Moser, 1996), whereby the shorted turn applied "braking" to both the acceleration and deceleration phase of the movement, therefore in the shorted turn could be "switched off" in the acceleration phase and switched on for the deceleration phase, leading to improvements in the dynamic performance.

Force experimentation showed that a shorted turn inhibits the high frequency force production of a coil, with lower resistance (thicker) shorted turns lowering the frequency at which the motor constant exhibits a drop in magnitude. Analysis showed that force is proportional to magnetising current (fig. 4-33) and not the primary coil current (as supplied to the actuator). Therefore, for the reduction in force production to occur at a higher frequency a larger shorted turn resistance (R_{ST}) would be required (figures 4-33 and 4-34). This would mean that although there will

still be a reduction in force, it will be less significant at higher frequencies, possibly increasing the coil acceleration relative to lower resistance shorted turns.

The force experimentation also highlighted the importance of holistic design within electromechanical devices as shorted turns are often inadvertent creations which could be inhibiting high frequency force production and device performance.

Step responses (figures 4-30 and 4-31) showed the shorted turn produced a damping effect, attenuating resonant peaks; depending on the frequencies that this resonance acts at, this may increase the stability margins of a system.

An S-Coil may be the most desirable way to achieve additional damping, as using a thinner wire reduces the reduction in motor constant, K_M at high frequencies due to the large shorted turn resistance. The displacement response due to an S-Coil was also analysed and showed that the damping was not related to the number of turns (fig 3-39 and Table 4-3) but instead the thickness in relation to the movement of the magnetic field. It was found that modifying the geometry of the S-Coil to a wider, thicker shape significantly increased the damping, while disconnecting the S-Coil removed the damping effect completely (table 4-3). This demonstrated that as with the current response the damping may be controlled with its geometric arrangement and its effects controlled with a switch, producing a controllable damper that may be applied to a wide range of electromechanical systems. It should however be noted that even with a large number of turns the S-Coil failed to produce the same level of damping as a single loop shorted turn. From further analysis of the displacement response; a model of the system was created in Simulink which gave a representation of the test rig's dynamic behaviour (fig. 4-41). This model was then used to estimate a range of damping constants showing that the damping was proportional to the square of the shorted turn thickness as would be consistent with eddy current damping.

The thesis demonstrates that although a shorted turn reduces the motor constant and magnitude of force at high frequencies, it does improve the transient response of the total coil current (fig. 4-19). This would suggest that a shorted turn may be very beneficial for positioning systems as the faster transient response could translate to faster settling times (Parker Hannifin, 2010). When these disturbances are around

the frequency where the open loop phase lag is 180 degrees this damping could also reduce the gain margin, and allow larger controller gains to be applied before the system reaches instability.

Based on the original aims outlined in chapters 2 and 3 the research detailed throughout this thesis has been successful. The aim of producing a comprehensive study of shorted turns was achieved by investigating the effect of a shorted turn on current, force and displacement responses and even investigating the effect of shorted turn parameters (R_{ST} and L_{ST}) on system behaviour. The only aspect of this research that prevents this from being a truly comprehensive study is that the research into shorted turns is only conducted on the test rig and not implemented into real-world electromechanical devices.

The aim of producing a shorted turn design framework was also achieved as parametric analysis produced a design tool for estimating the resistive and inductive properties of a shorted turn required for a certain application. It was also shown that, as well as producing a faster current response, a shorted turn also reduced the force output and applies damping; the thickest shorted turn available should be used for maximum damping effect. Following on from this research, for a more complete design framework, the next step would be to quantify the point at which the reduction in K_M negates the improvements in transient response.

A novel aspect of this research was the production of a controllable shorted turn, utilising an S-Coil. This could be a low-cost and mechanically-simple addition to existing devices that would allow optimisation of the shorted turn effect, minimising the negative aspects of shorted turns (such as a reduction in K_M). This additional flexibility may also allow the possibility of controllable damping.

7. Recommendations for Future Research

This work has demonstrated that a shorted turn may be used to reduce the high frequency coil impedance and phase lag within the testing rig used throughout this research. This opens avenues for further research into the effect of shorted turns on real world electromechanical devices. Pilot investigations outside the scope of this thesis, on a 3-phase AC permanent magnet motor, made it apparent that the Wagner transformer model only partially explains the current response of this system; with each phase producing a slightly different current response. This may have been due to the device casing; however, this may also be due to the phase connection method, such as a delta connection producing inductive effects. Therefore the next step would be to model these systems to produce an enhanced shorted turn 3-phase coil model.

Further investigation into 3-phase systems should be conducted to investigate whether the shorted turn or S-Coil could reduce the undesirable effects of commutation; e.g. reducing torque ripple offering further possible improvements in the dynamic performance.

The S-Coil has shown that it may offer significant benefits to an electromechanical device. However, the potential controllability is a feature that has never been seen on a shorted turn and would need further investigation into its applicability to real world devices. For example, if it is possible to use it with bang-bang control of a voice coil motor to improve move times.

8. Acknowledgements

I would like to give my deepest thanks to the many people who made this thesis possible. Firstly I would like to thank my Ph.D. supervisor Dr Ben Hanson for his enthusiasm, ideas, guidance and most of all patience. Words cannot express my gratitude.

I would like to thank UCL for funding that allowed me to deliver a conference paper in Malaysia, EPSRC for supporting me throughout this research and also a massive thank you to everyone at Instron for supplying the load cell, supporting me and making my time working in your offices an enjoyable experience. I would especially like to thank Paul Hayford for his guidance and Ben Jeppesen for his supervision and inspiring the S-Coil.

Finally I would like to thank my wonderful friends for their limitless support, patience and encouragement and my family for raising me, educating me, supporting me and most importantly, loving me. To all of you, I dedicate this thesis.

9. References

Allen, R. L., & Mills, D. W. (2004). Signal analysis: time, frequency, scale, and structure. In D. W. R. L. Allen, *Signal analysis: time, frequency, scale, and structure* (pp. 538-540). Wiley-IEEE.

Ananthanarayanan, K. (1982, May). Third-order theory and bang-bang control of voice coil actuators. *IEEE Transactions on Magnetics, 18*(3), 888 - 892.

Bae, J., Kwak, M. K., & Inman, D. J. (2005, June). Vibration Suppression of a Cantilever Beam using Eddy Current Damper. *Journal of Sound and Vibration, 284*(3-5), 805-824.

Bandera, P. (1998, September 29). *Patent No. 5814907.*

Beards, C. F. (1996). Structural Analysis: Vibration and Damping. Butterworth-Heinemann.

Benenson, W., Harris, J. W., Stöcker, H., & Lutz, H. (2002). Handbook of physics. Springer.

Boldea, I., & Nasar, S. A. (1999, September). Linear Electric Actuators and Generators. *IEEE Transactions on Energy Conversion, 14*(3), 712-717.

Boldea, I., & Nasar, S. A. (2001). Linear Motion Electromagnetic Devices. Taylor and Francis.

Bollen, M. H., & Gu, I. Y. (2006). Signal processing of power quality disturbances. John Wiley and Sons.

Brice, R. (2001). Music engineering. In R. Brice, *Music engineering* (pp. 416-425). Newness.

Chai, H. D., & Lissner, R. (1988, April). *Voice Coil Motors for Disk Storage Applications.* IBM Technical TR02.1460, IBM, San Jose, CA.

Christopoulos, C. (1990). An introduction to applied electromagnetism. Oxford University Press.

Clower, P. H. (1994, March 22). *Patent No. 5,296,796.* United States of America.

Collinson, R. P. (2011). Introduction to Avionic Systems. Springer.

Duttweiler, D. L. (1999, September 14). *Patent No. 5951626.*

Ec-Council. (2009). Investigating Hard Disks, File and Operating Systems. In Ec-Council, *Investigating Hard Disks, File and Operating Systems* (p. 9). Cengage Learning.

Fujimoto, Y., Kominami, T., & Hamada, H. (2009, May). Development and Analysis of a High Thrust Force. *IEEE Transactions on Industrial Electronics, 56*(5), 1383-1391.

Gonzalez, R. C., & Woods, R. E. (2007). Digital Image Processing. Pearson Prentice Hal.

Hajian, A., Sanchez, D., & Howe, R. (1997). Drum roll: increasing bandwidth through passive impedance modulation. *IEEE International Conference on Robotics and Automation*, (pp. 2294 - 2299). Albuquerque, NM , USA.

Hammond, P. (1997). Electromagnetism for engineers : an introductory course. Oxford University Press.

Hanselman, D. C. (1994, June). Minimum Torque Ripple, Maximum Efficiency Excitation of Brushless Permanent Magnet Motors. *IEEE Transactions on Industrial Electronics , 41*(3), 292-300.

Hanson, B. M., Brown, M., & Fisher, J. (2001). Self Sensing: Closed-Loop Estimation for a Linear Electromagnetic Actuator. *Proceedings of the American Control Conference*, (pp. 1650-1655). Arlington, VA.

Hirano, Naruse, & Tsuchiyama. (1989, July). Dynamic Characteristics of a Voice Coil Motor. *IEEE Transactions on Magnetics, 25*(4), 3073-3075.

Hofmann, G., Howe, S. D., Iorillo, A. J., Reiter, G. S., & Rubin, C. P. (1974, April 23). *Patent No. 3806062.*

Hughes, A. (2006). Electric Motors and Drives: fundamentals, types and applications . In A. Hughes, *Electric Motors and Drives: fundamentals, types and applications* (pp. 357-360). Newnes.

Ida, N. (2004). Engineering Electromagnetics. In N. Ida, *Engineering Electromagnetics* (pp. 484-491). Springer.

Incropera, F. P. (2007). *Fundamentals of Heat and Mass Transfer* (6th ed.). Hoboken, NJ: John Wiley & Sons.

Jacek, F. G. (1994). Linear Induction Drives. Oxford University Press.

Jaensch, M., & Lampérth, M. U. (2007, June). Investigations into the stability of a PID-controlled micropositioning and vibration attenuation system. *Smart Materials and Structures, 16*(4), 1066-1075.

Jagacinski, R. J., & Flach, J. (2003). Control theory for humans: quantitative approaches to modeling performance. Routledge.

Kang, C., & Kim, C. (2005, August). An Adaptive Notch Filter for Suppressing Mechanical Resonance in High Track Density Disk Drives. *Microsystem Technologies, 11*(8), 638-652.

Kang, J., & Sul, S. (1076-1082, September/October). New Direct Torque Control of Induction Motor for Minimum Torque Ripple and Constant Switching Frequency. *IEEE Transactions on Industry Applications, 35*(5), 1999.

Kazimierczuk, M. K. (2009). High-Frequency Magnetic Components. John Wiley and Sons.

Kester, W. A. (2005). Data conversion handbook. Newnes.

Kirtley, J. L. (2010). Electric Power Principles: Sources, Conversion, Distribution and Use. John Wiley and Sons.

Kothari, D., & Nagrath, I. J. (2006). Electric Machines. Tata McGraw-Hill Education.

Kwak, M. K., Lee, M. I., & Heo, S. (2003). Vibration suppression using eddy current damper. *Korean Society for Noise and Vibration Engineering, 13*(10), 760-766.

Le-Huy, H., Perret, R., & Feuillet, R. (1986, July/August). Minimization of Torque Ripple in Brushless DC Motor Drives. *IEEE Transactions on Indusry Applications, IA-22*(4), 748-755.

Lerner, L. S. (1997). Physics for Scientists and Engineers. Jones & Bartlett Publishers.

Magee, P., & Tooley, M. (2005). The physics, clinical measurement, and equipment of anaesthetic practice. Oxford University Press.

Majumdar, S. R. (2000). Oil hydraulic systems: principles and maintenance. Tata McGraw-Hill Education.

Miller, R., & Miller, M. R. (2007). Electricity and Electronics for HVAC. McGraw-Hill Professional.

Mir, S., Elbuluk, M. E., & Husain, I. (1997). Torque ripple minimization in switched reluctance motors using adaptive fuzzy control. *IEEE Industry Applications Conference*, (pp. 571 - 578). New Orleans, LA , USA.

Moser, M. A. (1996, May). Shorted Turn Effects in Rotary Voice Coil Actuators. *IEEE Transactions on Magnetics, 32*(3), 1736-1742.

Oatley, C. (1976). Electric and Magnetic Fields: an introduction. Cambridge University Press.

Parker Hannifin. (2010). *Fundamentals of Servo Motor Control.* Retrieved October 26, 2011, from Parker Hannifin Corporation: http://www.parkermotion.com/whitepages/ServoFundamentals.pdf

Qingwei, J., Mingzhong, D., Kiankeong, O., & Jianyi, W. (2008, January 15). *Patent No. 7319570.*

Semba, T., Kagami, N., & Tokizono, A. (2001, April 17). *Patent No. 6219196.*

Sibley, M. (1996). Introduction to electromagnetism. Arnold.

Skidmore, I. D., & Proulder, I. K. (2004, April 15). *Patent No. 20040071207.*

Slemon, G., Turton, R., & Burke, P. (1974, September). A linear synchronous motor for high-speed ground transport. *IEEE Transactions on Magnetics, 10*(3), 435 - 438.

Sodano, H. A., & Inman, D. J. (2007, September). Non-Contact vibration control system employing an active eddy current damper. *Journal of Sound and Vibration, 305*(4-5), 596-613.

Stamp, A., & Hanson, B. (2011). Modelling and Control Techniques for a Shorted Turn to Improve High Frequency Coil Response. *Advanced Materials Research Journal*, In Press.

Thompson, E. M. (2003, March 18). *Patent No. 6533083.*

Thornton, R. D. (2005). Linear Synchronous Motor Design. *IEEE Electric Machines and Drives*, (pp. 1555-1560). San Antonio, TX.

Umashankar, K. (1989). *Introduction to engineering electromagnetic fields.* World Scientific.

Wagner, J. A. (1982, November). The Shorted Turn in the Linear Actuator of a High Performance Disk Drive. *IEEE Transactions on Magnetics, 18*(6), 1170-1172.

Walsh, G. E. (1992). Muscles, masses and motion: the physiology of normality, hypotonicity, spasticity and rigidity. Cambridge University Press.

Winder, S. (2002). Analog and Digital Filter Design. Newnes Press.

Yamada, H., Sasaki, M., & Nam, Y. (2004, March). Control of a Micro-Actuator for Hard Disk Drives Using Self-sensing. *2004 8th IEEE International Workshop on Advanced Motion Control*, 147 - 152.

Zhao, H., & J. Jin, J. C. (2009). Virtual Instrument Based Fuzzy Control System for PMLSM Drive. *International Conference on Applied Superconductivity and Electromagnetic Devices*, (pp. 299-303). Chengdu, China.

Zhu, Y., & Cho, Y. (2010). Detent Force Reduction of Permanent Magnet Linear Synchronous Motor by Imposing Auxiliary Poles Technique. *IEEE Conference on Electromagnetic Field Computation (CEFC)*, (p. 1). Chicago, IL.

10. Appendices

10.1. APPENDIX 1

%MATLAB program to calculate the cost function of shorted turn %experimental data

function CostFun = X0(R2, L12, L2)

%Experimental Values

freq=logspace(0,3,100);

exper_coil=[Experimental data – Magnitude of admittance];

exper_coil_p= [Experimental data – Phase of admittance];

L1 = 7.3e-3; % Leakage inductance, primary coil

R1 = 22.9; % Primary coil resistance

%Initial Values

X0 = [R1, 12, L1, 1e-8, 9.8e-3]; %R2=12, L2=9.8e-3, L12=1e-8

%Shorted Turn Model

num_st=[(X0(4)+X0(5))X0(2)]

```
den_st=[(X0(3)*(X0(4)+X0(5))+X0(5)*X0(4))
(X0(3)*X0(2)+X0(1)*(X0(4)+X0(5))+X0(2)*X0(5)) (X0(1)*X0(2))]

[mag_st,pha_st,f]=bode(num_st,den_st, freq);
```

%Calculate Cost Frequency – Sum Squared Error

```
magerror = sum(exper_coil - mag_st)^2;

phaseerror = sum(exper_coil_p - pha_st)^2;

totalerror = magerror + phaseerror;

CostFun = totalerror;


options = optimset('PlotFcns',@optimplotfval);

[x,fval] = fminsearch(@CostFun,[-1.2, 1], options);
```